

Universidade Estadual Paulista “Júlio de Mesquita Filho”  
Faculdade de Engenharia de Ilha Solteira  
Campus de Ilha Solteira

Julio Cesar Eduardo de Souza

Optimization in ultrasonic imaging systems: Use of  
metaheuristics to design sparse arrays and a heuristic to create an  
acquistion system

Ilha Solteira

2022

Julio Cesar Eduardo de Souza

Optimization in ultrasonic imaging systems: Use of  
metaheuristics to design sparse arrays and a heuristic to create an  
acquisition system

Tese apresentada à Faculdade de Engenharia de  
Ilha Solteira – UNESP como parte dos requisitos  
para obtenção do título de Doutor na área de  
Engenharia Elétrica  
Área: Automação.

Dr. Ricardo Tokio Higuti  
UNESP-FEIS  
Supervisor:

Dr. Óscar Fernando Martínez-Graullera  
CSIC-ITEFI  
Co-supervisor:

Ilha Solteira

2022

FICHA CATALOGRÁFICA

Desenvolvido pelo Serviço Técnico de Biblioteca e Documentação

S729o Souza, Julio Cesar Eduardo de.  
Optimization in ultrasonic imaging systems: use of metaheuristics to design sparse arrays and a heuristic to create an acquisition system / Julio Cesar Eduardo de Souza. -- Ilha Solteira: [s.n.], 2022  
133 f. : il.

Tese (doutorado) - Universidade Estadual Paulista. Faculdade de Engenharia de Ilha Solteira. Área de conhecimento: Automação, 2022

Orientador: Ricardo Tokio Higuti

Coorientador: Óscar Fernando Martínez Graullera

Inclui bibliografia

1. Algoritmos de otimização estocástico. 2. Arrays 2D esparsos. 3. Array lineares esparsos. 4. Metaheurísticas.

*Raiane da Silva Santos*  
Raiane da Silva Santos

**CERTIFICADO DE APROVAÇÃO**

TÍTULO DA TESE: Optimization in ultrasonic imaging systems: use of metaheuristics to design sparse arrays and a heuristic to create an acquisition system

**AUTOR: JÚLIO CESAR EDUARDO DE SOUZA**

**ORIENTADOR: RICARDO TOKIO HIGUTI**

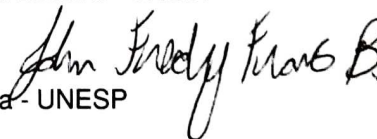
**COORIENTADOR: OSCAR MARTINEZ-GRAULLERA**

Aprovado como parte das exigências para obtenção do Título de Doutor em ENGENHARIA ELÉTRICA, área: Automação pela Comissão Examinadora:



Prof. Dr. RICARDO TOKIO HIGUTI (Participação Presencial)  
Departamento de Engenharia Eletrica / Faculdade de Engenharia de Ilha Solteira - UNESP

Prof. Dr. JOHN FREDY FRANCO BAQUERO (Participação Presencial)  
Departamento de Engenharia Elétrica / Campus Experimental de Rosana - UNESP



Prof. Dr. WALLACE CORREA DE OLIVEIRA CASACA (Participação Virtual)  
Departamento de matemática aplicada / IBILCE - UNESP

Prof. Dr. VANDER TEIXEIRA PRADO (Participação Virtual)  
Departamento de engenharia elétrica / Universidade Tecnológica Federal do Paraná - UTFPR

Prof. Dr. THEO ZEFERINO PAVAN (Participação Virtual)  
Departamento de Física / USP / Ribeirão Preto/SP

Ilha Solteira, 02 de setembro de 2022

Dedico este trabalho a Sônia Souza que com muito carinho e apoio não mediu esforços para  
que eu chegasse até esta etapa na minha vida.

Ao meu pai, Paulo Souza (*in memoriam*), que me inspira a buscar por meus objetivos de vida.  
Quando criança, o senhor desejava que eu me tornasse doutor, faltou esclarecer qual.

## ACKNOWLEDGMENT

À minha amada Jéssica, por muitas vezes foi coagida a debater sobre a minha tese, me segurou quando desejei cair e juntos estamos enfrentando os desafios.

À minha cachorrinha Luna, companheira durante o desenvolvimento e escrita da tese. Os passeios diários me ajudaram a ter ideias e pensar nas soluções dos problemas encontrados.

Ao meu orientador Prof. Dr. Ricardo Higuti, pela confiança no meu trabalho, conselhos e mentoria na minha carreira.

Ao meu coorientador Dr. Óscar Martínez Graullera, pelos ensinamentos repassados e ajuda no desenvolvimento da tese.

À minha avó Maria Takahashi (*in memoriam*), que esteve presente na minha criação e ajudou a formar a pessoa que sou hoje.

Aos meus companheiros do LUS, em específico Marcelo Tiago e Vander Prado, pela colaboração direta e indireta para que este trabalho fosse construído.

Aos professores que me ajudaram e motivaram a chegar até este estágio da minha vida. Espero conseguir motivar as pessoas assim como os senhores me motivaram.

A Coordenação de Aperfeiçoamento de Pessoal de Nível Superior (CAPES) e o Conselho Nacional de Desenvolvimento Científico e Tecnológico (CNPq), pelo auxílio financeiro.

À minha família, pois acredito que sem o apoio deles seria muito difícil vencer esse desafio.

E a todos os que direta ou indiretamente fizeram parte da minha formação, o meu obrigado.

"I have not failed. I have found 10,000 ways that it will not work"

**Thomas Edison**

## RESUMO

Imagens ultrassônicas possuem importante papel no diagnóstico médico e ensaio não destrutivo. Uma das alternativas para geração de imagens consiste em utilizar um *array*, um transdutor composto por um conjunto de elementos piezelétricos, para gerar diversas frentes de ondas e amostrar suas reflexões. Uma característica física importante para construção dos *arrays* é a sua dimensão. Quanto maior a extensão do *array*, melhor será a resolução lateral da imagem gerada. Além disso, uma recomendação de fabricação dos *arrays* é que o centro dos seus elementos precisam estar espaçados por uma distância (*pitch*) menor ou igual a  $0,5\lambda$ , em que  $\lambda$  é o comprimento da onda gerada pelo transdutor. Desta forma, as imagens geradas por esses *arrays* não apresentam artefatos causados pelos lóbulos de espaçamento. A recomendação para o uso de *arrays* é que seja o maior *array* possível, respeitando a restrição de *pitch*. No entanto, o volume de dados, recursos e custo de fabricação aumentam proporcionalmente à medida que o número de elementos no *array* aumenta, o que pode torná-lo impraticável dependendo da aplicação. Esta tese propõe técnicas para reduzir o uso de recursos em sistemas ultrassônicos visando obter imagens com alta resolução lateral e mitigar eventuais desvantagens. No primeiro estágio, *arrays* esparsos lineares cujos *itches* são superiores que  $0,5\lambda$  são estudados. Propõe-se uma nova estratégia para projetar esses *arrays*, na qual é apresentada uma nova codificação matemática para os *arrays* esparsos e uma função de aptidão baseada na equação de energia e entropia das PSFs (*Point Spread Function*). Posteriormente, algoritmos de otimização estocástico são utilizados para desenhar as configurações esparsas lineares. A função aptidão proposta foi comparada com a função aptidão mais utilizada na literatura, baseada no diagrama de radiação. Identificou-se que a função proposta valoriza configurações de *arrays* esparsos que geram imagens com melhor equilíbrio entre contraste e resolução lateral. Além disso, foi identificado que a função aptidão proposta na literatura apresenta inconsistências ao avaliar os *arrays* esparsos, o que não ocorre na função proposta. Em seguida, uma nova estratégia de aquisição de dados para *arrays* bidimensionais que não estão em uma malha é proposta. A estratégia se baseia em analisar as projeções dos elementos do *coarray* e manter somente as combinações de elementos emissores e receptores mais importantes para a geração de imagens. Assim, o número de aquisições e volume de dados de aberturas esparsas bidimensionais, cujos elementos não estão posicionados em uma malha, é reduzido, bem como o tempo de geração de imagens. As análises dos resultados indicaram a viabilidade em reduzir os sinais adquiridos sem comprometer a qualidade das imagens geradas. Adicionalmente, foram desenvolvidas duas figuras de mérito baseadas na análise da disposição espacial dos elementos, que por sua vez foram utilizadas para avaliar *arrays* 2D esparsos. A relação entre as figuras de mérito desenvolvidas e a energia irradiada pelos *arrays* foi estudada e, a partir desta análise, uma função custo desenvolvida. Em seguida, é apresentada uma estratégia para projetar *arrays* 2D esparsos utilizando o algoritmo *simulated annealing*. As análises do diagrama de radiação das aberturas bidimensionais esparsas obtidas pelo algoritmo de busca possuem característi-

cas desejáveis com alta resolução lateral e baixa intensidade nos artefatos. A tese possui três contribuições para os sistemas de geração de imagens por ultrassom que reduzem os custos de manufatura e computacional.

**Palavras-chave:** Algoritmos de Otimização Estocástico. *Arrays* 2D Esparsos. *Array* Lineares Esparsos. Metaheurísticas.

## ABSTRACT

Ultrasonic images have an important contribution to medical diagnosis and non-destructive testing. One strategy to generate an image is to use an array, which is a transducer composed of a set of piezoelectric elements, that emits several wavefronts and samples the reflected waves. An important physical characteristic of arrays is their dimension. The wider the array extension, the better the lateral resolution of the generated image will be. Additionally, a construction recommendation for arrays is that the centre of their elements must be spaced by a distance (pitch) less or equal to  $0.5\lambda$ , where  $\lambda$  is the generated wavelength by the transducer. Thus, the images generated by these arrays do not present artefacts caused by the grating lobes. The recommendation for using arrays is that it has to be the wider array possible, respecting the pitch recommendation. However, the data volume, resource, and manufacturing cost proportionally increase as the number of elements in the array rises, which might be impractical to use this array depending on the application. This thesis investigates techniques to reduce the use of resources in ultrasonic systems aiming to achieve images with high lateral resolution and mitigate any disadvantages. In the first part of this thesis, the linear sparse arrays, which are arrays that pitch higher than  $0.5\lambda$  are studied. A new strategy to design these arrays is proposed, where a new mathematical codification for sparse arrays and fitness function based on the equation of energy and entropy of the PSFs (Point Spread Function) are presented. Subsequently, stochastic optimization algorithms are used to design sparse configurations. The proposed fitness function was compared with the most used fitness function in the literature based on the radiation pattern. The sparse arrays found using the proposed fitness function generated images with a balance between contrast and lateral resolution. Moreover, it was noticed that the fitness function proposed in the literature has inconsistencies when evaluating sparse array configurations which do not happen with the proposed fitness function. Next, a new data acquisition strategy for synthetic aperture for two-dimensional arrays that are not in a grid is proposed. This strategy is based on analysing the projections of the elements of the coarray and keeping only the combinations of emitter and receiver elements that are most important for image generation. Consequently, the number of acquisitions and data volume of sparse two-dimensional apertures, whose elements are not positioned in a grid, is reduced, as well as the image generation time. The results indicate that it is possible to reduce the number of acquiring signals without compromising the quality of the ultrasonic image generated. In addition, two figures of merit based on the spatial distribution of the elements were used to evaluate sparse 2D arrays. A study of these parameters and how they influence the energy irradiated by arrays is done, and a fitness function is created. Then, a strategy to design a sparse 2D array is proposed using the simulated annealing algorithm. The radiation pattern analysis of the sparse arrays obtained from the search algorithm shown that the aperture generated images with high lateral resolution and low artefact intensities. The radiation pattern analysis of the sparse arrays obtained from the search algorithm showed that the aperture generated images with high lateral resolution and low

artefact intensities. This thesis has three main contributions to ultrasonic systems that reduce manufacturing and computational costs.

**Keywords:** 2D Sparse Arrays. Linear Sparse Arrays. Metaheuristics. Stochastic Optimization Algorithms.

## LIST OF FIGURES

Figure 1 – (a) Linear and (b) annular segmented array. . . . .	30
Figure 2 – (a) Matrix, (b) Fermat spiral, (c) segmented annular and (d) mills cross arrays. . . . .	31
Figure 3 – Pressure sum of a linear array at a point $P(R, \theta)$ considering the elements are point sources. . . . .	32
Figure 4 – (a) Radiation Pattern of 4 (solid blue line), 8 (dash-dot red line) and 16 (dashed green line) elements array. (b) Apodization of a 16 linear array with Rectangular (solid blue line), Hanning (dash-dot red line) and Hamming (dashed green line) apodization. . . . .	35
Figure 5 – Radiation Pattern of 256 elements matrix array with $0.5\lambda$ pitch. . . . .	35
Figure 6 – Wideband response of (a) linear array with different numbers of elements and (b) 256 elements matrix array with $0.5\lambda$ pitch. . . . .	37
Figure 7 – Pressure of an array element with width $a$ . . . . .	37
Figure 8 – (a) Energy irradiated by an element with different $a/\lambda$ values: (b) Radiation Pattern narrowband response modulated by the directivity of the element with a $a = 0.5\lambda$ width. . . . .	39
Figure 9 – 32 elements radiation pattern considering a pitch equal to: (a) $0.50\lambda$ , (b) $0.75\lambda$ , (c) $1\lambda$ and (d) $2\lambda$ . . . . .	40
Figure 10 – (a) Fully populated array (blue dot), sparse aperiodic array (red dot), sparse periodic array (green dot) and the missing elements to complete a fully populated array. (b) the radiation pattern narrow band response of the presented arrays with the <i>MLW</i> and <i>PSL</i> highlighted. . . . .	41
Figure 11 – Illustration of <i>Crt</i> . (a) the array elements are periodically spaced (in a grid). (b) One reception element is shifted by 0.3. . . . .	45
Figure 12 – (a) Transmit and Receiver Linear FPA with 32 elements. (b) the coarray formed from the two arrays with triangular shape with all elements respecting a pitch $0.5\lambda$ . (c) the radiation pattern of the transmit array and the coarray (two-way radiation pattern). . . . .	46
Figure 13 – (a) Sparse Transmit and Receiver Linear arrays created based on Vernier distribution, (b) the coarray created where it has the triangular shape, respects a pitch $0.5\lambda$ but it has adjacents elements that alternate the amplitudes and (c) the two-way radiation pattern of the coarray created. . . . .	47
Figure 14 – (a) Matrix array with 256 elements ( $16 \times 16$ ) where the adjacent elements in the $x$ -axis and $y$ -axis have a pitch equals to $0.5\lambda$ ( $\lambda = 1[mm]$ ) and the elements diagonally adjacents have a pitch equals to $0.70\lambda$ . (b) The coarray is created from the matrix array which has a pyramidal shape. . . . .	48

Figure 15 – An example of the minimum redundancy array (KARAMAN et al., 2009) where (a) 30 elements are disposed of two vertical lines and (b) 30 elements are disposed of two horizontal lines where the elements in the lines have a pitch equal to $0.5\lambda$ ( $\lambda = 1[mm]$ ). (c) the coarray is generated from these two apertures where the majority of the elements have amplitude one. . . . .	48
Figure 16 – Simple imaging system using a single element transducer. (a) representation of the imaging system where the transducer is shifted only in the $x$ axis and the resulting image (b) created in the $x$ and $z$ -axis. (c) An imaging strategy where the transducer moves in $x$ and $y$ -axis. (d) the segmented image generated in a different depth. . . . .	50
Figure 17 – Phased Array inspection modalities. (a) B-scan. (b) Focused B-scan. (c) Sector Scan. . . . .	51
Figure 18 – Synthetic Aperture Radar. . . . .	51
Figure 19 – Synthetic Aperture. . . . .	51
Figure 20 – Total Focusing Method (TFM). Representation in $(x, z)$ grid (a), and in $(r, \theta)$ grid (b). . . . .	52
Figure 21 – Data set simulation. (a) electrical input response. (b) shifted signal to the time of flight ( $9\mu$ ). . . . .	54
Figure 22 – PSF of an FPA with 32 elements. (a) Image generated from $-90^\circ$ to $90^\circ$ . (b) as the array is symmetric it is only necessary to generate half of the image (from $0^\circ$ to $90^\circ$ ). . . . .	54
Figure 23 – PSFs of (a) FPA with 32 elements, (b) SPA with 32 elements a pitch $\lambda$ and (c) SPA with 32 elements and pitch $2\lambda$ . (d) normalized sum of the amplitudes. . . . .	55
Figure 24 – (a) a sparse array created by selecting 16 elements in a grid corresponding to a 32 FPA. (b) the PSF of the sparse array where the energy besides the point reflector is not concentrated in a specific area. . . . .	56
Figure 25 – Eight elements FPA (red dot), where four elements were selected (blue dot) to create a sparse array. . . . .	59
Figure 26 – PSF of (a) 96 elements FPA, (b) 128 elements FPA and (c) amplitude are summed and then normalized at each angle of the PSF, where the blue continuous line corresponds to the 96 elements FPA and the red dashed line corresponds to 128 elements FPA. . . . .	63
Figure 27 – PSFs created using the 66 elements sparse array configurations related to Table 2, where (a) is the WOA Run 1 configuration and (b) the AOA Run 1 configuration. In (c), the normalized means of the two PSF are illustrated where the PSF in (a) is illustrated in a blue continuous line and (b) is illustrated in a red dashed line. . . . .	64

Figure 28 – PSFs created using the 88 elements sparse array configurations related to Table 2, where (a) is the SA Run 1 configuration and (b) the SA Run 3 configuration. In (c), the normalized means of the two PSF are illustrated where the PSF in (a) is illustrated in a blue continuous line and in (b) is illustrated in a red dashed line. . . . .	65
Figure 29 – PSFs created using the 102 elements sparse array configurations related to Table 3, where (a) is the WOA Run 1 configuration and (b) the SA Run 3 configuration. In (c), the normalized mean of the two PSF are illustrated where the PSF in (a) is illustrated in a blue continuous line and (b) is illustrated in a red dashed line. . . . .	66
Figure 30 – (a) Distance where the defect is placed based on the array size ( $D$ ). (b) PSF of a FPA with 64 elements is used as an example. (c) normalized mean extracted from the PSF showing the first valley and (d), the segmented PSF used to calculate the Energy. . . . .	68
Figure 31 – PSFs created using the 48 elements sparse arrays in a search space of 96 FPA, where the FF of each configuration is illustrated in Table 4. (a) is the WOA Run 1 configuration and (b) the WOA Run 3 configuration. In (c), the normalized means of the two PSF are illustrated where the PSF in (a) is illustrated in a blue continuous line and (b) is illustrated in a red dashed line. . . . .	70
Figure 32 – PSFs created using the 88 elements sparse arrays in a search space of 128 FPA, where the FF of each configuration is illustrated in Table 4. (a) is the WOA Run 1 configuration and (b) the AOA Run 2 configuration. In (c), the normalized means of the two PSF are illustrated where the PSF in (a) is illustrated in a blue continuous line and (b) is illustrated in a red dashed line. . . . .	71
Figure 33 – PSFs created using the 110 elements sparse arrays in a search space of 128 FPA, where the FF of each configuration is illustrated in Table 4. (a) is the WOA Run 3 configuration and (b) the WOA Run 3 configuration. In (c), the normalized means of the two PSF are illustrated where the PSF in (a) is illustrated in a blue continuous line, in (b) is illustrated in a red dashed line and the. . . . .	72
Figure 34 – Dansk Phantom Model 525. . . . .	73
Figure 35 – Ultrasonic images of (a) Section 3, (b) Section 6 and (c) Section F of the Dansk Phantom Model 525. . . . .	74
Figure 36 – Phantom Section 3 Image using: (a) 128 Elements FPA, (b) best 96-configuration found using the Radiation Pattern FF and (c) best 96-configuration found using the FF proposed in this work. . . . .	75

Figure 37 – Section F of the phantom generated using the (a) 96 FPA, (b) the best 48 elements sparse array found using the FF based on radiation pattern and (c) the best 48 elements sparse array found using the proposed FF. Section 6 of the phantom generated using the (d) 96 FPA, (e) the sparse array found using the FF based on radiation pattern and (f) the 48 elements sparse array found using the proposed FF. . . . .	79
Figure 38 – Section 3 of the phantom generated using the (a) 96 FPA, (b) the 80 elements best sparse array found using the FF based on radiation pattern and (c) the 80 elements best sparse array found using the proposed FF. . . . .	79
Figure 39 – (a) Section F and (d) Section 6 of the phantom generated using the 128 FPA, (b) and (e) the phantom images generated by the 96 elements best sparse array found using the FF based on radiation pattern and (c) and (f) the phantom images generated by the 96 elements best sparse array found using the proposed FF. . . . .	81
Figure 40 – For matrix arrays: (a) array structure, (b) coarray footprint, (c) equivalente array projection at $\phi = 0^\circ$ , and (d) radiation pattern at $\phi = 0^\circ$ (wideband response, BW=60%). For spiral array aparture: (e) array structure,(f) coarray footprint, (g) equivalente array projection at $\phi = 0^\circ$ , and (h) radiation pattern at $\phi = 0^\circ$ (wideband response, BW=60%) . . . . .	84
Figure 41 – Matrix presentation of acquisition strategy ( <i>ACQ</i> ) for a generic array composed of 64 elements. White cells are the active channels. (a) <i>ACQ1</i> - the reciprocity principle has been applied to reduce the number of signals. (b) <i>ACQ2</i> - the reciprocity principle also has been used to optimise the electronic resources. . . . .	85
Figure 42 – Compact Representation of <i>ACQ2</i> (a) and an ultrasonic acquisition system (b). . . . .	86
Figure 43 – Example of Coarray Projection Grid ( <i>CPG</i> ) where each $[p, g]$ position contains a set of coarray elements $\vec{C}_{er}$ that meet the condition (42) . . . . .	88
Figure 44 – The 64 element spiral. (a) array footprint, (b) coarray footprint, (c) acoustic pressure in the semi-sphere [ $\theta = 0^\circ : 90^\circ, \phi = 0^\circ : 360^\circ$ ] and (d) lateral profile showing the distribution of the sidelobes in elevation. The dashed line represents the spiral beampattern, and the light grey area within that line shows side lobe distribution at each elevation angle. The solid line is the corresponding beampattern of a 64 element matrix array. . . . .	92
Figure 45 – (a) strategy (64 : 64) for redundancy reduction. (b) sidelobe distribution at each elevation angle for strategy (64 : 64) (light grey area within the dashed line) and the <i>FMC</i> (dark grey area within the solid line). . . . .	93
Figure 46 – Acquisition matrix obtained from (a) <i>ACQ</i> (64 : 32), (b) <i>ACQ</i> (64 : 16) and (c) <i>ACQ</i> (64 : 8). . . . .	94

Figure 47 – Sidelobes distribution at each each elevation angle for strategies (a) $ACQ(64 : 32)$ , (b) $ACQ(64 : 16)$ and (c) $ACQ(64 : 16)$ (light grey area within the dashed line) and the $FMC$ (dark grey area within the solid line). . . . .	94
Figure 48 – $ACQ$ obtained from (a) the setting $(32 : 64)$ and (b) the setting $(16 : 64)$ . . . . .	95
Figure 49 – Sidelobes distribution at each each elevation angle for strategies (a) $(32 : 64)$ and (b) $(16 : 64)$ (light grey area within the dashed line) and the $FMC$ (dark grey area within the solid line). . . . .	95
Figure 50 – Segmented annular array. (a) Array prototype; (b) experimental setup in water, array faced downwards and a 3 mm-diameter spherical reflector placed 40 mm from the array; (c) element distribution, (d) coarray footprint. Image of a (e) point reflector (simulated) and (f) 3 mm-diameter metallic sphere (experimental) both placed at $[X=-25 : 25 \text{ mm}, Y=-25 : 25 \text{ mm}, Z=40 \text{ mm}]$ . . . . .	97
Figure 51 – Results for the segmented annular array obtained from $ACQ$ (a) $(64 : 64)$ , (b) $(64 : 24)$ , (c) $(64 : 16)$ and (d) $(64 : 8)$ , where the acquisition strategy, the simulated point reflector, the experimental metallic sphere image (cylindrical coordinates: $Z = 40 \text{ mm}$ $R = [0 : 25] \text{ mm}$ , $\theta = [0^\circ : 360^\circ]$ ), and the image reflectivity (maximum at each elevation angle) are illustrated, respectively. For the image reflectivity, the simulated response is illustrated in the dashed line and the experimental result in the solid line. . . . .	99
Figure 52 – Results obtained from $ACQ$ (a) $(42 : 42)$ , and (b) $(32 : 32)$ , where the acquisition strategy is presented on the left, the sidelobe distribution at each elevation angle for strategies is illustrated at the centre, and the configuration of the multiplexer net showing, at each shot, the distribution of reception transducer in the reception channels is illustrated in the right. For the sidelobe distribution, the current $ACQ$ is represented in a light grey area within the dashed line, and the $FMC$ is represented as a dark grey area within the solid line. . . . .	100
Figure 53 – (a) Asymmetrical matrix sparse array, (b) Radiation Pattern narrowband response, (c) Line extracted at $0^\circ$ of the narrowband response and (d) Radiation Pattern wideband Response with the amplitudes extracted at $0^\circ$ . . . . .	104
Figure 54 – (a) 360 Elements Fermat Spiral Array with $40 \lambda$ diameter ( $\lambda = 1 \text{ mm}$ ) and $\alpha = 160.875^\circ$ . (b) the radiation pattern of the spiral array. (c) the radiation pattern of the spiral array with the same setting, but elements placed in a $60 \lambda$ diameter. (d) the lateral profile of the two radiation patterns. . . . .	106
Figure 55 – Radiation pattern wideband response of the three sparse arrays with 64 elements emitting and 64 elements receiving with $40\lambda$ diameter, where the $M_o$ and $M_r$ information are given in Table (10). (a), (b) and (c) are generated using configurations 1, 2 and 3, respectively. . . . .	107

Figure 56 – (a) lateral profile of configuration 1 and 2 of $128/40\lambda$ and (b) the radiation pattern comparison. . . . .	108
Figure 57 – Radiation Pattern comparison, only the main lobe analysis. (a) Combination 1-3 (b) Combination 2-3. . . . .	110
Figure 58 – Radiation pattern wideband response of the three sparse arrays with 96 elements emitting and 96 elements receiving with $40\lambda$ diameter, where the $M_o$ and $M_r$ information are given in Table (10). (a), (b) and (c) are generated using configurations 1, 2 and 3, respectively. . . . .	111
Figure 59 – Radiation pattern wideband response of the three sparse arrays with 128 elements emitting and 128 elements receiving with $60\lambda$ diameter, where the $M_o$ and $M_r$ information are given in Table (10). (a), (b) and (c) are generated using configurations 1, 2 and 3, respectively. . . . .	112
Figure 60 – Optimization convergence. (a) $128/40\lambda$ , (b) $192/40\lambda$ and (c) $256/60\lambda$ . . . . .	115
Figure 61 – Radiation pattern wideband response of the spiral optimized arrays. (a) 128, (b) 192 and (c) 256 elements array. . . . .	116
Figure 62 – Radiation pattern comparison between the optimized $128/40\lambda$ aperture and configuration-1 of $128/40\lambda$ . . . . .	117
Figure 63 – Segmented annular array example with 128 elements distributed in 8 radii. (a) radii in phase. (b) radii randomly rotated. . . . .	118
Figure 64 – Radiation pattern wideband response of the segmented annular optimized arrays. (a) 128, (b) 192 and (c) 256 elements array. . . . .	119
Figure 65 – Search Space. (a) Image of a second-order equation. (b) Image of a different FF where there are minimums that the search algorithm can be stuck. . . . .	125
Figure 66 – Search Space. (a) illustration of intensification and diversification process in metaheuristics. (b) real representation of a searching problem. . . . .	126

## LIST OF TABLES

Table 1 – Comparison between search algorithm using the fitness function proposed by Trucco (1999). . . . .	42
Table 2 – Comparison between search algorithms using the radiation pattern based fitness function given in (30). Search space corresponding to a 96 elements FPA . . . . .	61
Table 3 – Comparison between search algorithms using the radiation pattern based fitness function given in (30). Search space corresponding to a 128 elements FPA . . . . .	62
Table 4 – Comparison between search algorithms using the radiation pattern based fitness function given in (33). Search space corresponding to a 96 and 128 elements FPA . . . . .	69
Table 5 – MSSIM calculated between an image generated with a sparse array and a reference image . . . . .	77
Table 6 – CNR of section 3, 6 and F of the phantom image generated by the sparse arrays and the 96 and 128 FPA . . . . .	78
Table 7 – Fermat spiral array: performance for the <i>FMC</i> , <i>RCP</i> and all six strategies considered ( <i>Tx : Rx</i> ). . . . .	93
Table 8 – Segmented Annular Array. Performance for the (64 : 64), (64 : 24), (64 : 16) and (64 : 8) settings. Simulated and experimental data included for $\Delta\theta_{-6dB}$ , DR (dB) and $\Delta\theta_{DR}$ . . . . .	98
Table 9 – Spiral array: <i>FMC</i> , <i>RCP</i> , <i>ACQ</i> (42 : 24) and <i>ACQ</i> (32 : 32) acquisition strategies results. . . . .	101
Table 10 – $M_o$ and $M_r$ results of different configurations . . . . .	106
Table 11 – Main Lobe and Side Lobe distribution analysis for the spiral array with 40 and 60 $\lambda$ . . . . .	109
Table 12 – $M_o$ , $M_r$ and $M_oM_r$ of different configurations with different settings and their optimized aperture. . . . .	115
Table 13 – Main lobe and side lobe distribution analysis. Optimized aperture vs configurations 1,2 and 3. . . . .	116
Table 14 – $M_o$ , $M_r$ and $M_oM_r$ of spiral and segmented optimized array. . . . .	118
Table 15 – Main lobe and side lobe distribution analysis. Spiral array vs segmented annular array . . . . .	119

## LIST OF ABBREVIATIONS AND ACRONYMS

<i>ACQ</i>	Acquisition strategy
<i>AOA</i>	Arithmetic optimization algorithm
<i>bPSO</i>	binary particle swarm algorithm
<i>CP</i>	Crossing Point between lateral profiles
<i>CNR</i>	Contrast to noise ratio
<i>CPG</i>	Coarray Projection Grid
<i>DTFT</i>	Discrete-Time Fourier transform
<i>DR</i>	Dynamic range
<i>FF</i>	Fitness function
<i>FMC</i>	Full matrix capture
<i>FPA</i>	Fully populated array
<i>GFP</i>	Global Free Positions
<i>GNFP</i>	Global Non-Free Positions
<i>GA</i>	Genetic algorithm
<i>GPGPU</i>	General-Purpose Graphics Processing Units
<i>ICPG</i>	Inverse Coarray Projection Grid
<i>MLW</i>	Main-lobe width
<i>MRC</i>	Minimum redundancy coarray
<i>MSSIM</i>	Mean structural similarity image measurement
<i>PSF</i>	Point spread function
<i>PSL</i>	Peak side-lobe
<i>PSO</i>	Particle swarm optimisation
<i>ROI</i>	Region of interest
<i>SA</i>	Simulated annealing
<i>SAA</i>	Sparse aperiodic array

SNR	Signal to noise ratio
SPA	Sparse periodic array
SSIM	Structural Similarity Image Measurement
TFM	Total focusing method

## LIST OF SYMBOLS

$AR_e$	Set of emitters array elements
$AR_r$	Set of receiver array elements
$a$	Array element width
$\alpha$	Divergence Angle
$BW$	Relative bandwidth
$\beta$	decreasing temperature rate in the Simulated Annealing
$c$	Speed of sound
$CAN$	Signal sets
$Crt$	Coarray set position
$\vec{C}_{er}$	Coarray element of emitter $e$ and receiver $r$
$C_{e_1r_1}$	Coarray element of emitter $e_1$ and receiver $r_1$
$C_{e_2r_2}$	Coarray element of emitter $e_2$ and receiver $r_2$
$C_{buf}$	Buffer containing the position of the coarray element projected.
$D$	Diameter of the aperture or Array Size
$d$	Pitch
$dp$	Infinitesimal pressure contribution
$dx$	Infinitesimal distance of the array element
$\delta$	Kronecker delta function
$\delta(t - \tau_{er})$	Time shifted impulse
$\Delta\tau$	Time delay between two elements
$\Delta\theta_{-6dB}$	Main lobe width when the lateral profile decrease to -6dB
$\Delta\theta_{DR}$	Main lobe width is defined at the level of the dynamic range
$e$	Euler's constant
$E$	Energy used to create the new FF
$e$	Index used to indicate emitter elements

$\vec{e}_e$	Vector with the position of the emitter element
$\vec{e}_i$	Vector with the position $(x_i, y_i)$ of the element
$\vec{e}_r$	Vector with the position of the receiver element
$\eta$	$\eta = 1.5/(BWf_c)$ .
$f_c$	Center frequency of the array
$f_s$	Sample Frequency
$FP$	counter of the filled positions in the <i>MAP</i> matrix
$G_c$	Candidate to the acquisition set
$GFP$	Global free positions counter
$GNFP$	Global non-free positions counter
$g(t)$	Ultrasonic pressure pulse
$g$	Column position of the <i>CPG</i> matrix
$g(t - \tau_{er})$	Ultrasonic pressure pulse delayed
$h(\theta, \theta_s, t)$	Array impulse response in relation to $\theta$ and $\theta_s$
$h(u, t)$	Array impulse response in relation to $u$
$h(\vec{r}, \vec{r}_f, t)$	Impulse response of 2D array
$H$	Entropy used to create the new FF
$H_1(\theta)$	Radiation Pattern of an array in a given angle $\theta$
$H_2(\theta)$	Radiation Pattern of an element in a given angle $\theta$
$H_2(\theta, \phi)$	Radiation Pattern of an element in a given angle $\theta$ and $\phi$
$i$	Variable used as an index
$i0$	Pair of emitter and receiver elements current selected
$I(x, z)$	Image amplitude at pixel $x$ and $z$
$I(R, \theta)$	Image amplitude at pixel radius $R$ and angle $\theta$
$I_1$	First ultrasonic image used to calculate the <i>MSSIM</i>
$I_{1_i}$	Area of the image $I_{1_i}$

$I_2$	Second ultrasonic image used to calculate the <i>MSSIM</i>
$I_{2_i}$	Area of the image $I_{2_i}$
$j$	Imaginary unit ( $j^2 = -1$ )
$L$	Array element length
$\lambda$	wavelength
$k$	Wavenumber
$k_1$	Weights used in the fitness function
$k_2$	Weights used in the fitness function
$N$	Number of elements in the array
$N_c$	Maximum number of parallel channels
$N_g$	Number of angles where the coarray elements are projected
$N_k$	Exchange control in the Simulated Annealing algorithm
$N_p$	Number of coarray grid positions
$N_{pix}$	Number of pixels in the PSF image
$N_s$	Number of signals used to create an ultrasonic image
$NFP$	Counter for the redundancy introduced in the <i>MAP</i> matrix
<i>MAP</i>	Matrix that counts the number of coarray elements that fill a position $(p, g)$
<i>MPD</i>	Maximum number of Parallel Degree
$M_r$	Redundancy level
$M_o$	Occupancy rate
$\mu$	Mean
$\theta$	Azimuth angle
$\theta_i$	Azimuth angle for the array element $i$
$\theta_s$	Azimuth angle where the beam is steering
$P$	Location where all acoustic pressures sum
<i>PD</i>	Parallelism Degree per element counter

$P(R, \theta, t)$	Sum of the acoustic pressures
$p$	Row position of the <i>CPG</i> matrix
$p(\theta, \theta_s, t)$	Acoustic pressure in wide band response
$p(R, t)$	Acoustic pressure in a radius $R$ for a given time $t$
$p_i(R, \theta, t)$	Acoustic pressure in a radius $R_i$ for a given azimuthal angle $\theta$ and time $t$
$p(\vec{r}, \vec{r}_f, t)$	Acoustic pressure wide band response for 2D arrays
$p_0$	Function of the wave number $k$
$PSF_{ref}$	Reference point spread function
$\phi$	Projection angle
$\phi_p$	Angular discretization
$\varphi$	Phase in the Fermat spiral array
$\rho_i$	Values of the probability distribution
$\rho$	Probability distribution used to calculate the Entropy
$r$	Index used to indicate receiver elements
$R$	Radius distance
$R_i$	Distance from the array element $i$ to the point where the acoustic pressure is analysed
$R'$	Distance from a point in the array element to the point where the acoustic pressure is analysed
$RCP$	Acquisition Strategy based on reciprocity
$R_x$	Number of parallel channels
$s_{er}(t)$	Ultrasonic signal related to the emitter $e$ and receiver $r$
$\hat{s}_{er}$	Hilbert transform of the ultrasonic signal related to the emitter $e$ and receiver $r$
$\sigma$	Standard Deviation
$t$	Time
$T_k$	Current temperature used in the Simulated Annealing algorithm

$T_x$	Number of elements emitting
$\tau$	Time of flight
$\tau_{er}$	Delay time of the ultrasonic wave that propagates from the emitter $e$ , is reflected and reaches the receiver $r$
$\tau_{er}(x, z)$	Time of flight from the emitter element to the point $(x, z)$ and back to the receiver element
$u$	$u = \sin(\theta) - \sin(\theta_s)$
$u_0$	Constant related to the ultrasound pulse transmitted by a single element
$x$	variable $x$ used to represent any value
$x_0$	start the solution of a metaheuristic
$x_v$	best solution of a metaheuristic
$y$	variable $y$ used to represent any value
$w_i$	Amplitude Modulation
$w_{er}$	Amplitude Modulation related to the emitter $e$ and receiver $r$
$\omega$	Angular frequency
$\omega_\theta$	$\omega_\theta = -kd \sin(\theta) + \omega\Delta\tau$

## CONTENTS

<b>1</b>	<b>INTRODUCTION</b> . . . . .	26
1.1	OBJECTIVE . . . . .	28
<b>1.1.1</b>	<b>Specific objectives</b> . . . . .	28
1.2	OUTLINE OF THE WORK . . . . .	28
<b>2</b>	<b>FUNDAMENTALS AND LITERATURE REVIEW</b> . . . . .	30
2.1	ARRAYS . . . . .	30
<b>2.1.1</b>	<b>The radiation pattern</b> . . . . .	31
<b>2.1.2</b>	<b>Sparse array</b> . . . . .	39
<b>2.1.3</b>	<b>Coarray</b> . . . . .	44
2.2	ULTRASONIC IMAGING . . . . .	49
<b>2.2.1</b>	<b>Phased array</b> . . . . .	49
<b>2.2.2</b>	<b>Synthetic aperture</b> . . . . .	50
<b>2.2.3</b>	<b>Point Spread Function</b> . . . . .	53
2.3	COMMENTS . . . . .	55
<b>3</b>	<b>NEW STRATEGY FOR LINEAR SPARSE ARRAY DESIGN</b> . . . . .	57
3.1	FITNESS FUNCTION BASED ON THE RADIATION PATTERN AND SEARCH ALGORITHM ANALYSIS . . . . .	57
<b>3.1.1</b>	<b>Countinous codification</b> . . . . .	58
<b>3.1.2</b>	<b>Comparing algorithms with radiation pattern fitness function</b> . . . . .	59
3.2	NEW FITNESS FUNCTION . . . . .	66
3.3	RESULTS AND DISCUSSION . . . . .	73
3.4	COMMENTS . . . . .	80
<b>4</b>	<b>ACQUISITION STRATEGY FOR NON-GRID APERTURES</b> . . . . .	82
4.1	THE COARRAY ANALYSIS . . . . .	82
<b>4.1.1</b>	<b>Identification of redundancy in the coarray</b> . . . . .	86
4.2	ACQUISITION STRATEGIES ALGORITHM . . . . .	87
<b>4.2.1</b>	<b>Step one: Generation of the CPG database</b> . . . . .	88
<b>4.2.2</b>	<b>Step two: Acquisition Strategy Design</b> . . . . .	89
4.3	EVALUATION OF THE PROCEDURE . . . . .	90
<b>4.3.1</b>	<b>Fermat spiral array</b> . . . . .	91
<b>4.3.2</b>	<b>Segmented annular array - simulated and experimental results</b> . . . . .	96
<b>4.3.2.1</b>	<i>Experimental setup</i> . . . . .	96
<b>4.3.2.2</b>	<i>Synthetic aperture strategies</i> . . . . .	96
4.4	DISCUSSION . . . . .	98
4.5	COMMENTS . . . . .	101
<b>5</b>	<b>2D SPARSE ARRAY EVALUATION</b> . . . . .	103

5.1	FITNESS FUNCTION BASED ON CPG . . . . .	103
<b>5.1.1</b>	<b>Mo and Mr analysis</b> . . . . .	104
5.2	PROBLEM FORMULATION AND SEARCH ALGORITHM . . . . .	113
5.3	FERMAT SPIRAL OPTIMIZATION . . . . .	114
5.4	SEGMENTED ANNULAR ARRAY OPTIMIZATION . . . . .	117
5.5	COMMENTS . . . . .	120
<b>6</b>	<b>FINAL COMMENTS AND FUTURE WORK</b> . . . . .	121
6.1	RECAPITULATION AND APPLICATIONS . . . . .	121
6.2	CONTRIBUTIONS . . . . .	122
6.3	PUBLICATIONS . . . . .	123
6.4	FUTURE WORKS . . . . .	123
	<b>APPENDIX A – SEARCH PROBLEMS AND METAHEURISTICS</b> . .	125
	<b>BIBLIOGRAPHY</b> . . . . .	128

## 1 INTRODUCTION

Ultrasonography is a relevant medical procedure used in several areas such as cardiology, orthopedics, and gynaecology. Using ultrasonic images, pathologies are detected in a non-ionizing, non-invasive, and non-traumatic way. It also allows the visualization of abnormalities that are not detected using other techniques, such as the ventricular septal defect, which cannot be diagnosed using the electrocardiogram (DAKKAK; OLIVER, 2020).

Ultrasonic systems are cheaper than other equipments, such as tomography or magnetic resonators. It allows fast diagnosis and can be used to combat pandemics by earlier identifying a person suffering from an illness, such as the use of lung ultrasound to diagnose the coronavirus (COVID- 19) (DUGGAN et al., 2020; QIAN et al., 2020; YU et al., 2020; BEVAN et al., 2020). It is also used for non-destructive testing to monitor parts and prevent accidents. There are several applications for ultrasound imaging in non-destructive testing to detect defects in parts and structures, such as cracks, delaminations and corrosions, and prevent accidents (LAROCHE et al., 2020; JOLLY et al., 2015; KHALILI; CAWLEY, 2018).

The simplest way to generate an ultrasonic image is to use a single-element transducer, for example, a piezoelectric element that converts electrical energy into acoustic pressure, and vice-versa. The transducer is excited, generating an acoustic wave that interacts with the medium (reflections, refractions, attenuation, etc.), and the same transducer can receive the echoes. By moving the transducer along a line, for example, an image can be created by plotting the reflected amplitudes for each transducer position. An array is a group of piezoelectric elements which can be linearly placed to image a section of an object, or bidimensionally (2D), to create volumetric images. One significant advantage of using arrays is that the individual elements can be independently excited, creating the possibility of beam steering and focusing without the need to move the array (or demanding small movements, in some cases). Although electronic complexity increases, lateral resolution and contrast can be improved compared to single-element operation (DRINKWATER; WILCOX, 2006).

When using an array, a recommendation for the distance between the centre of adjacent elements is at most  $0.5\lambda$ , where  $\lambda$  is the wavelength (LOCKWOOD et al., 1996a). This distance, called pitch, is relevant because, when the elements have a pitch higher than  $0.5\lambda$ , the resulting irradiated energy sums in different areas resulting in image deterioration. Another feature that contributes to image quality is the size of an array: the broader an array, the better the lateral resolution of an image (TRUCCO, 1999).

In this sense, the construction recommendation is to use larger arrays with  $0.5\lambda$  pitch. Nevertheless, extending the size of an array increases the number of elements, and, in consequence, increases the electronic complexity, data volume, and time to generate an image, which might be undesirable for a specific application or even make the imaging system impractical.

The need to find a solution for this problem is clear for 2D arrays, which are used to

create volumetric images. Considering an array with  $32\lambda \times 32\lambda$  dimension, if the elements are placed in a matrix pattern, 16384 elements would be required. Despite this type of array being physically fabricated using CMOS technology (ORALKAN et al., 2003), the resource to control all these elements turns its use impractical. For example, using the synthetic aperture technique (JENSEN et al., 2006), which is an imaging strategy where the emitter elements of the array are sequentially excited and the sampled ecos stored and post-processed, 268,435,456 mathematical operations would be necessary to create an image pixel, which is time-consuming and impractical for real-time applications.

There are different strategies to enable the use of this array. For example, Karaman et al. (2009) created a method that defines the minimum number of elements in a matrix array, decreasing the time to generate an image. Combining the synthetic aperture technique and their strategy would be required 64,516 mathematical operations to create an image pixel, considerably reducing the number of operations. However, this strategy only works for matrix arrays. For arrays where the elements are not placed in a matrix grid (non-grid arrays), it is necessary to create a different method that selects the emitter and receiver elements of the aperture, which creates a routine that reduces the number of acquisitions required, enabling real-time applications and decreasing the computation cost to generate an image for non-grid arrays.

Another strategy consists in creating a sparse array, in which elements' pitches are higher than  $0.5\lambda$ . With fewer elements, the area covered is still high and the lateral resolution remains elevated. However, because of the energy summing in different areas, the sparse array has the problem of decreasing the image's contrast compared to an array that respects the  $0.5\lambda$  recommendation. Although linear arrays uses fewer elements (64 to 256) and is commercially spread, the use of sparse linear arrays might be still beneficial. For example, new imaging systems might use the power supply and computation power of cellphones to generate images. Sparse arrays could be handy for this application, as fewer elements demand fewer resources (battery, processing). Moreover, if a certain number of elements in a probe burns, a sparse linear array could be designed to work without this array. The burned and some specific elements from the array are excluded from the imaging process, and the resulting image still would have good lateral resolution and contrast. This strategy allows to recycle and extend the array's life.

The need for sparse 2D arrays is straightforward justified when compared to linear arrays because of the higher number of elements and signals involved. At this date, matrix arrays with a reasonable size, as mentioned previously, have an elevated number of elements, becoming impossible to control all of them simultaneously (MARMONIER et al., 2022). Consequently, 2D sparse arrays are practically mandatory to achieve high lateral resolution using a manageable number of elements.

One strategy is to distribute the elements using a nature-based equation, such as the Fermat spiral equation, where the displacement is in a non-grid area. With fewer elements, it is possible to cover a wider area and distribute the elements with reduced periodicity, which is

a problem that contributes to increased artefact intensities in ultrasonic images (MARTÍNEZ–GRAULLERA et al., 2010).

Another strategy is to use search engines to design a sparse configuration, where the algorithm determines the elements' position (ROUX et al., 2017). These search algorithms, called metaheuristics, are part of stochastic optimization methods that can intelligently test solutions and return the best-found, according to a predefined condition (NESMACHNOW, 2014). In general, for ultrasonic imaging systems, the search mechanism creates different sparse configurations and finds one that attends to defined circumstances, such as image quality and system resources. Moreover, these two strategies can be merged to create sparse 2D arrays where, at first, the elements are placed in a non-grid distribution. Then, metaheuristics eliminate elements and create a more sparse aperture.

## 1.1 OBJECTIVE

The main goal of this work is to find strategies to decrease the time, data volume and resources of an ultrasonic imaging system.

### 1.1.1 Specific objectives

- Understand how the ultrasonic images are generated and investigate the modelling methods used to evaluate linear and 2D arrays.
- Analyse the different metaheuristics to design sparse linear arrays.
- Propose a technique to design linear sparse arrays.
- Identify and remove redundant information for imaging systems based on synthetic aperture for 2D arrays.
- Define a strategy to design 2D sparse arrays for non-grid apertures.

## 1.2 OUTLINE OF THE WORK

Chapter 2 gives the theoretical background and the literature review regarding fundamental and state-of-the-art techniques used in this work, where the mathematical functions used to evaluate, types and the strategies used to create sparse arrays are presented. Then, different metaheuristics working to design linear sparse array configurations are analysed, where a new codification and a fitness function based on the simulation of a point reflector are presented in chapter 3. In chapter 4, an acquisition strategy for synthetic aperture is presented where the aim is to decrease the acquisition for non-grid 2D arrays and enable real-time applications. In chapter 5, spatial parameters created during the previous chapter are analysed and used to define

a fitness function that is used with the simulated annealing algorithm to design sparse non-grid 2D arrays. Final considerations are made where the contributions of this work are highlighted and future ideas given.

## 2 FUNDAMENTALS AND LITERATURE REVIEW

In this chapter, the theoretical background used in this work is given and the recent literature in sparse array design are reviewed.

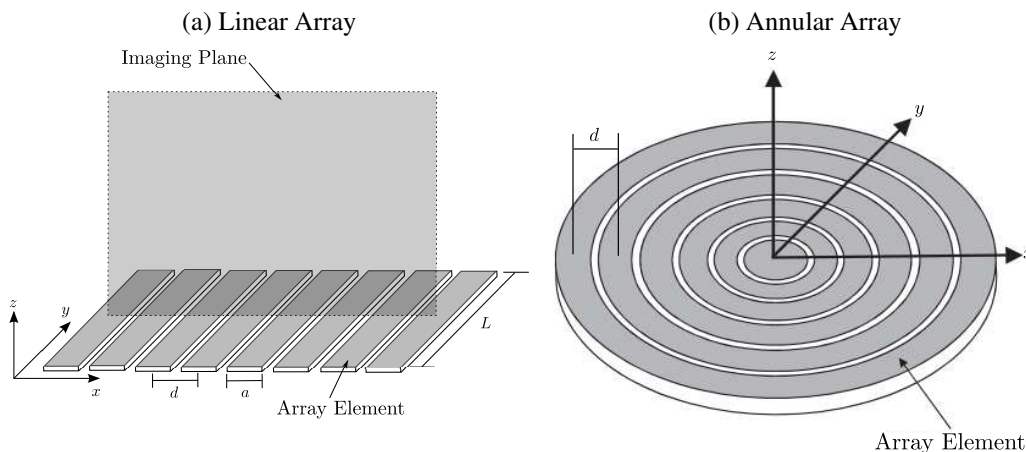
### 2.1 ARRAYS

One strategy to generate an ultrasonic image is to use an array, a group of piezoelectric elements, that converts electrical energy into vibration and vice-versa. The arrays are divided into two groups: the arrays used to generate 2D images, such as the linear and the annular array, and the arrays used to create 3D images, like the matrix array, the annular segmented array and the Fermat spiral array (DRINKWATER; WILCOX, 2006).

The linear and annular arrays are illustrated in Figure 1, where  $d$  is the array pitch, which is the distance between the centre of adjacent elements,  $a$  and  $L$  are the element width and length of the linear array element, respectively. Both arrays generate 2D images, but the difference between them is that the linear array allows beam steering in the imaging plane, and the annular array allows only the focal depth (DRINKWATER; WILCOX, 2006).

In this work, linear arrays are divided into three groups: the fully populated array (FPA), which is an array where the pitch  $d$  has the maximum value of  $0.5\lambda$ . The sparse periodic array (SPA), where the pitch is higher than  $0.5\lambda$  but equal to all elements, and the sparse aperiodic array (SAA), where the pitches are not the same, and some of them are higher than  $0.5\lambda$ .

Figure 1 – (a) Linear and (b) annular segmented array.

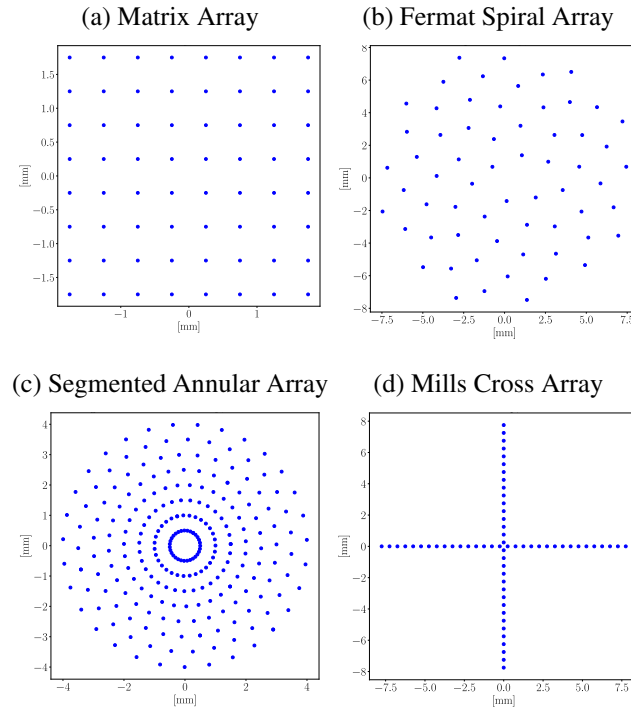


Source: Adpated from (DRINKWATER; WILCOX, 2006)

Arrays used for 3D imaging have more design space, and different configurations are proposed. The most intuitive way to place the elements in a 2D array is in a matrix (Figure 2 (a)), where the array elements are placed into a matrix shape that creates a grid. However, different types of configurations result in images with considerable good contrast using fewer

elements, such as the Fermat spiral (Figure 2 (b))(MARTÍNEZ-GRAULLERA et al., 2010), segmented annular (Figure 2 (c))(MARTÍNEZ et al., 2003), and cross mills arrays (Figure 2 (d)) (MONDAL et al., 2005).

Figure 2 – (a) Matrix, (b) Fermat spiral, (c) segmented annular and (d) mills cross arrays.



Source: Author

Both linear and 2D arrays, when increased in size and number of elements, require a considerable amount of electronic and computational resources to operate. Depending on the application and available resources, it is necessary to find alternatives to reduce the time to acquire and generate an image or the manufacturing cost to produce an ultrasonic system. To achieve this goal, it is necessary to understand different methods used to analyse ultrasonic imaging systems, where one of these is the radiation pattern.

### 2.1.1 The radiation pattern

The Radiation Pattern is the energy irradiated by an element source or array (JENSEN, 2002). It can be simulated considering the far field and elements continuously excited with a sinus signal, referred to as the narrowband response, or considering different electrical excitation, ideally the pulse excitation, which is the wideband response (CARDONE et al., 2001).

Although several ultrasonic applications in imaging occur in the near field and the array elements are pulsed, the radiation pattern narrowband response is a modelling tool used to analyse array response and its ability to generate images with high lateral resolution and contrast. Moreover, this modelling tool aids in understanding the concepts of ultrasonic imaging. Con-

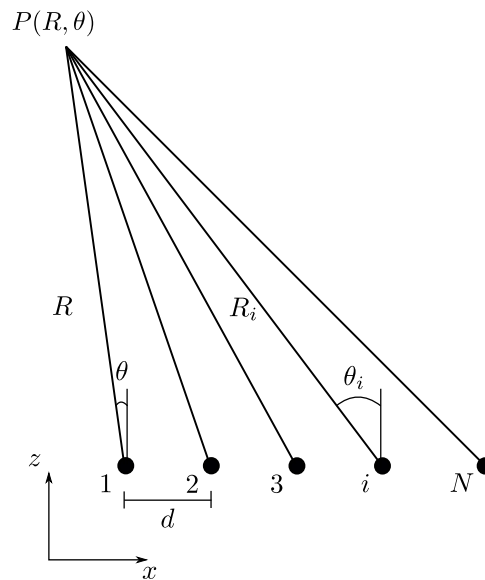
sidering that a point source generates an omnidirectional acoustic wave, the acoustic pressure  $p$  as a function of time  $t$  and radius  $R$  is described as (WOOH; SHI, 1999a):

$$p(R, t) = \left(\frac{p_0}{R}\right)^{\frac{1}{2}} e^{j(\omega t - kR)}, \quad (1)$$

where  $\omega$  is the angular frequency, and  $p_0$  is a function of the wavenumber  $k$ , derived from the solution of the acoustic wave. Therefore, the acoustic pressure of an array with  $N$  sources generators is given as the sum of pressures described in (1).

Figure 3 illustrates a linear periodic array with  $N$  elements and pitch ( $d$ )  $0.5\lambda$ . Element  $i$  has a distance  $R_i$  and angle  $\theta_i$  to the point  $P$ , where the acoustic pressure ( $p_i(R_i, \theta_i, t)$ ) is analysed and calculated as:

Figure 3 – Pressure sum of a linear array at a point  $P(R, \theta)$  considering the elements are point sources.



Source: Author

$$p_i(R_i, \theta_i, t) = \left(\frac{p_0}{R_i}\right)^{\frac{1}{2}} e^{j(\omega(t - (i-1)\Delta\tau) - kR_i)}, \quad (2)$$

where  $1 \leq i \leq N$ ,  $\Delta\tau$  is the difference in time-of-flight of the wave propagating from element  $i$  to the point  $P$  and its neighbour.

Considering that a triangle with vertices at element 1, element  $i$  and point  $P$ , the following relationship between  $R$  and  $R_i$  is built:

$$R_i = \sqrt{R^2 + [(i-1)d]^2 - 2R(i-1)d \cos(\pi/2 - \theta)}. \quad (3)$$

However, if the distance where the pressure is analysed is sufficiently farther than the pitch  $d$  (far-field) and the lines  $R_i$  are considered parallel, (3) can be approximated as (WOOH; SHI, 1999a):

$$R_i \approx R - (i - 1)d \sin(\theta), \quad (4)$$

and using (4) in (2), the following relationship is obtained:

$$p_i(R, \theta, t) = \left(\frac{P_0}{R}\right)^{\frac{1}{2}} e^{j(\omega t - kR)} e^{-j(\omega(i-1)\Delta\tau - k(i-1)d \sin(\theta))}, \quad (5)$$

where the pressure of any element  $i$  is in function of  $R$ ,  $\theta$  and  $t$ .

Therefore, the total acoustic pressure is the sum of all pressures of the  $N$  elements, given by:

$$P(R, \theta, t) = \sum_{i=1}^N w_i p_i(R, \theta, t), \quad (6)$$

where  $w_i$  is an amplitude modulation used to change the radiation pattern response to achieve the desired response, also known as apodization (SZABO, 2014).

Substituting (5) in (6), the following relationship is achieved:

$$P(R, \theta, t) = \left(\frac{P_0}{R}\right)^{\frac{1}{2}} e^{j(\omega t - kR)} \sum_{i=1}^N w_i e^{-ji(-kd \sin(\theta) + \omega\Delta\tau)}, \quad (7)$$

defining  $\omega_\theta = -kd \sin(\theta) + \omega\Delta\tau$ , (7) can be rewritten as:

$$P(R, \theta, t) = \left(\frac{P_0}{R}\right)^{\frac{1}{2}} e^{j(\omega t - kR)} \sum_{i=1}^N w_i e^{-ji\omega_\theta}, \quad (8)$$

and considering  $w[i] = 0$  for  $i \notin [1, N]$ , (8) can be written as :

$$P(R, \theta, t) = \left(\frac{P_0}{R}\right)^{\frac{1}{2}} e^{j(\omega t - kR)} \sum_{i=-\infty}^{\infty} w_i e^{-ji\omega_\theta}, \quad (9)$$

which the right part of the equation is a Discrete-Time Fourier transform (DTFT) of  $w_i$ . Thus, the DTFT of the apodization coefficients is equal to the radiation pattern of the linear array.

Solving (9), the energy irradiated by a linear array with uniform apodization ( $w_i = 1$ ,  $1 \leq i \leq N$ ) can be written in the harmonic form as:

$$P(R, \theta, t) = \left(\frac{P_0}{R}\right)^{\frac{1}{2}} \frac{\sin[((\omega\Delta\tau - kd \sin(\theta))/2)N]}{\sin((\omega\Delta\tau - kd \sin(\theta))/2)} e^{-j\left(\frac{\omega\Delta\tau - kd \sin(\theta)}{2}\right)(N-1)} e^{j(\omega t - kR)}, \quad (10)$$

and gives information about the energy irradiated from a set of emitters. Moreover, a normalization at any arbitrary steering angle  $\theta_s$  is given by:

$$H_1(\theta) = \left| \frac{P(R, \theta, t)}{P(R, \theta_s, t)} \right|. \quad (11)$$

Substituting (8) in (11), the following relationship is obtained:

$$H_1(\theta) = \left| \sum_{i=-\infty}^{\infty} w_i e^{-ji(\omega\theta - \omega\theta_s)} \right|, \quad (12)$$

and using the relationship  $\Delta\tau = d \sin(\theta_s)/c$ , (12) has the following solution:

$$H_1(\theta) = \left| \frac{\sin((\pi d(\sin(\theta_s) - \sin(\theta))/\lambda)N)}{N \sin(\pi d(\sin(\theta_s) - \sin(\theta))/\lambda)} \right|. \quad (13)$$

Using linear arrays with 4, 8 and 16 elements, where the elements are equally spaced with a  $0.5\lambda$  pitch (FPA), the radiation pattern using (13) is illustrated in Figure 4(a).

In sparse array design, two features are used to evaluate the array performance in generating ultrasonic images, the main-lobe width (*MLW*), which is the angular length where the main lobe is -6 dB and related to the lateral resolution of the images, and the peak side-lobe (*PSL*), which is the maximum side-lobe peak related to artefacts and contrast of the ultrasonic images (YANG et al., 2006; HU et al., 2018; HU et al., 2017; ZHANG et al., 2020).

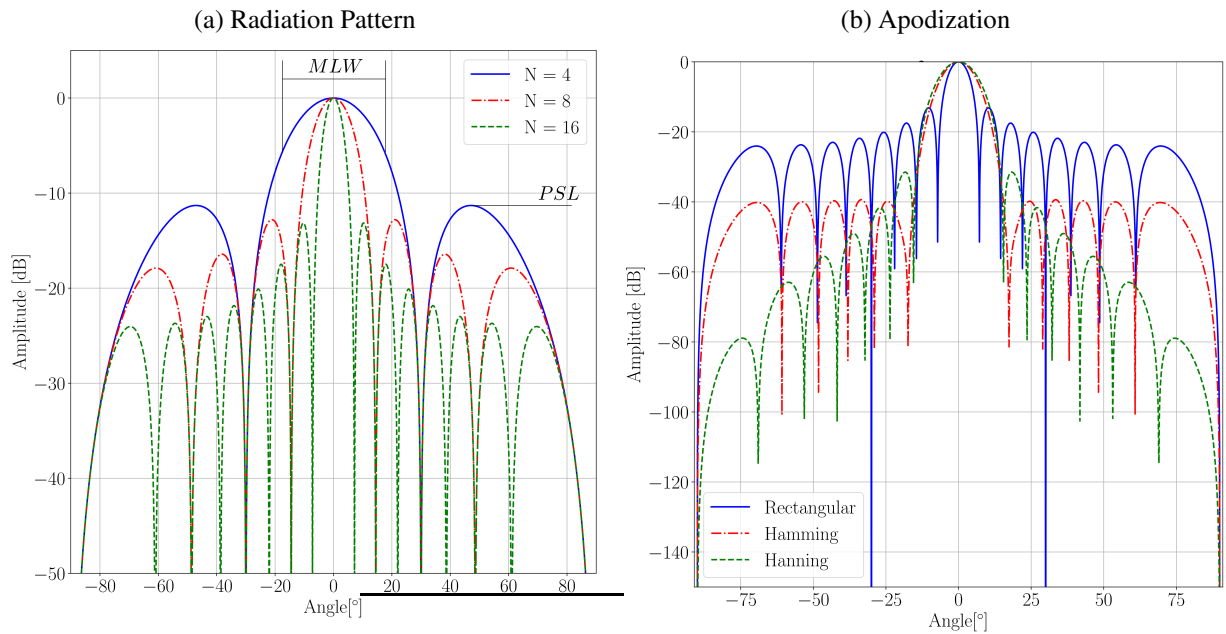
In both features, it is desirable to have a low value. For *MLW*, increasing the array's size will reduce its value. However, using an FPA, the number of elements will increase, requiring more resources. Sparse arrays are handy for this problem because a wider length size array can be achieved using fewer elements. For *PSL*, one strategy to reduce its value is using a sparse aperiodic array or apodization, as will be seen in this chapter.

In Figure 4(b), the radiation pattern of a linear array with 16 elements is illustrated where three apodizations were used: Rectangular, Hamming and Hanning. As it can be seen, the Hamming and Hanning apodizations decrease side lobes levels, with a trade-off with increasing main lobe width (SZABO, 2014).

The radiation pattern can be also expanded to 2D arrays, where the elements are positioned on the  $x$  and  $y$ -axis. In this sense, instead of only considering the azimuthal angle, the radiation pattern of a 2D array is obtained in both azimuthal ( $\theta$ ) and elevation angle ( $\phi$ ), described as:

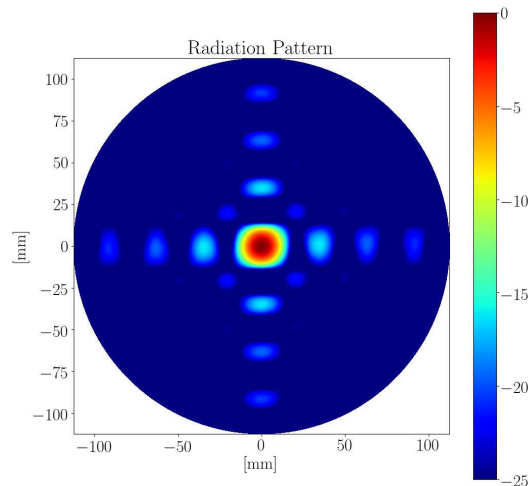
$$H_1(\theta, \phi) = \left| \sum_{i=1}^N w_i e^{-jk(x_i(\cos(\phi) - y_i \sin(\phi)) \sin(\theta) - (x_i \cos(\phi_s) + y_i \sin(\phi_s)) \sin(\theta_s))} \right|. \quad (14)$$

Figure 4 – (a) Radiation Pattern of 4 (solid blue line), 8 (dash-dot red line) and 16 (dashed green line) elements array. (b) Apodization of a 16 linear array with Rectangular (solid blue line), Hanning (dash-dot red line) and Hamming (dashed green line) apodization.



Source: Author

Figure 5 – Radiation Pattern of 256 elements matrix array with  $0.5\lambda$  pitch.



Source: Author

Figure 5 illustrates the radiation pattern of a matrix array with 256 elements ( $16 \times 16$ ) with a  $0.5\lambda$  pitch that separates each element. In this figure, it is possible to see the main lobe at the centre and the side lobes.

The radiation pattern presented, so far, is created considering the narrowband response.

In order to obtain the wideband radiation pattern, which is a response close to ultrasonic imaging systems, it is necessary to consider the ultrasonic pressure pulse transmitted by a single element. Using the array impulse response, the acoustic pressure in wideband response is given by (CARDONE et al., 2001):

$$p(\theta, \theta_s, t) = g(t) * h(\theta, \theta_s, t), \quad (15)$$

where the asterisk denotes convolution,  $g(t)$  the ultrasonic pressure pulse and  $h(\theta, \theta_s, t)$  is the array impulse response given by (CARDONE et al., 2001):

$$h(\theta, \theta_s, t) = \sum_{i=1}^N w_i \delta \left( t - \frac{id(\sin(\theta) - \sin(\theta_s))}{c} \right), \quad (16)$$

and  $\delta()$  is the Kronecker Delta function.

The number of parameters in the equation can be reduced by considering the sinusoidal relationship as a real value  $u = \sin(\theta) - \sin(\theta_s)$ , therefore (16) becomes:

$$h(u, t) = \sum_{i=1}^N w_i \delta \left( t - \frac{i u}{2 f_c} \right), \quad (17)$$

where  $f_c$  is the centre frequency of the transducer.

The ultrasound pulse transmitted by a single array element  $g(t)$  can be simulated as a Gaussian-envelope sinusoidal pulse, which can be given by (CARDONE et al., 2001):

$$g(t) = u_0 e^{\frac{\pi^2 BW^2 f_c^2 (t-\eta)^2}{1.2 \ln 10}} \sin(2\pi f_c t), \quad (18)$$

where  $u_0$  is a constant,  $BW$  the -6 dB relative fractional bandwidth, and  $\eta = 1.5/(BW f_c)$ .

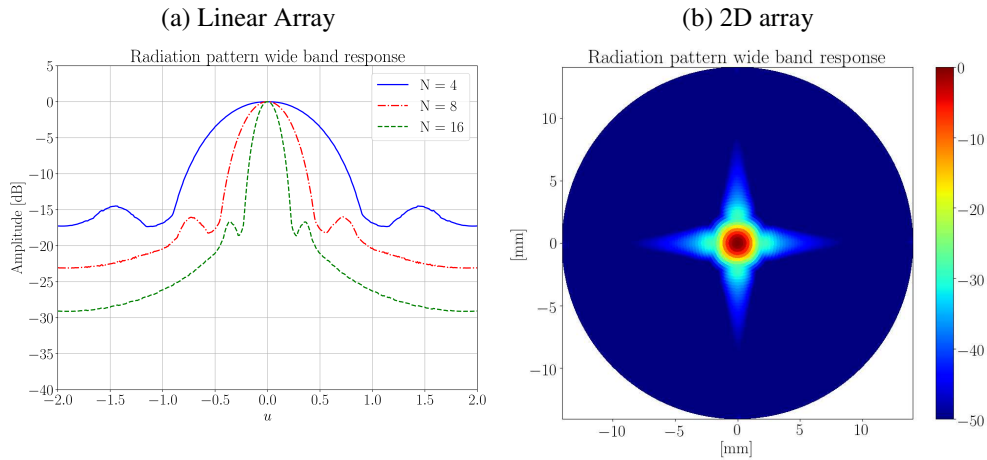
For 2D apertures, the radiation pattern wideband response is calculated using the following equation (TURNBULL; FOSTER, 1991):

$$p(\vec{r}, \vec{r}_f, t) = g(t) * h(\vec{r}, \vec{r}_f, t), \quad (19)$$

where  $h(\vec{r}, \vec{r}_f, t)$  is the impulse response of the 2D array,  $\vec{r}$  it a vector with the azimuthal angle and radius ( $\theta, \phi$  and  $R$ ) where the pressure is sampled and  $\vec{r}_f$  is the focus position of the radiation pattern.

Figure 6 (a) illustrates the FPA wideband radiation pattern with 4, 8 and 16 elements linear array, respectively. Figure 6 (b) illustrates the radiation pattern for the 256 matrix array. As it can be seen, the representation of the side lobes is attenuated in both images, compared to linear and 2D FPA.

Figure 6 – Wideband response of (a) linear array with different numbers of elements and (b) 256 elements matrix array with  $0.5\lambda$ pitch.

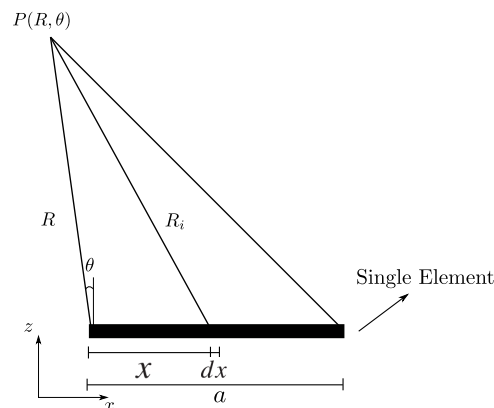


Source: Author

All simulations presented consider the array elements as point sources, where the irradiated energy is omnidirectional. Real elements do not behave like this as they have finite dimensions. The energy irradiated by an array element can be calculated and included in the radiation pattern to give a better approximation of the practical performance of the array (WOOH; SHI, 1999b).

In Figure 7, the dimensional array element is illustrated, where it is possible to see from a different perspective the dimension  $a$  illustrated in Figure 1 (a).  $x$  is the distance between the origin and a point of the element.

Figure 7 – Pressure of an array element with width  $a$ .



Source: Author

Using the Huygens' principle, which says that every point on the radiation surface is the origin of an outgoing spherical wave (JENSEN, 2002), the energy of a rectangular array element with width  $a$  and length  $L$  is calculated as:

$$p(R, \theta, t) = \int_0^a dp, \quad (20)$$

where  $dp$  is the infinitesimal pressure contribution of the element with width  $a$ , written as:

$$dp = \left(\frac{p_0}{R}\right)^{1/2} e^{j(\omega t - kR)} dx, \quad (21)$$

and the  $dx$  in the integral means an infinitesimal distance of the array width illustrated in Figure 7.

Considering that the element's width  $a$  is smaller than the distance  $R'$  ( $R_i \gg a$ ),  $R_i$  can be approximated using a similar relationship used in (3) as:

$$R_i = \sqrt{R^2 + x^2 - 2Rx \cos(\theta)} \approx R - x \sin(\theta), \quad (22)$$

and (20) can be written as:

$$\begin{aligned} p(R, \theta, t) &= \int_0^a dp = \left(\frac{p_0}{R}\right)^{1/2} \frac{\sin(ka \sin(\theta/2))}{k \sin(\theta/2)} e^{-\frac{jka \sin(\theta)}{2}} e^{j(\omega t - kR)} \\ &= \left(\frac{p_0}{R}\right)^{1/2} \text{sinc}(ka \sin(\theta/2)) e^{-\frac{jka \sin(\theta)}{2}} e^{j(\omega t - kR)}, \end{aligned} \quad (23)$$

where normalizing the pressure at a max angle ( $\theta \rightarrow 0$ ) gives the directivity for a single element as (WOOH; SHI, 1999a):

$$H_2(\theta) = \left| \frac{\sin(\pi a \sin(\theta)/\lambda)}{\pi a \sin(\theta)/\lambda} \right|, \quad (24)$$

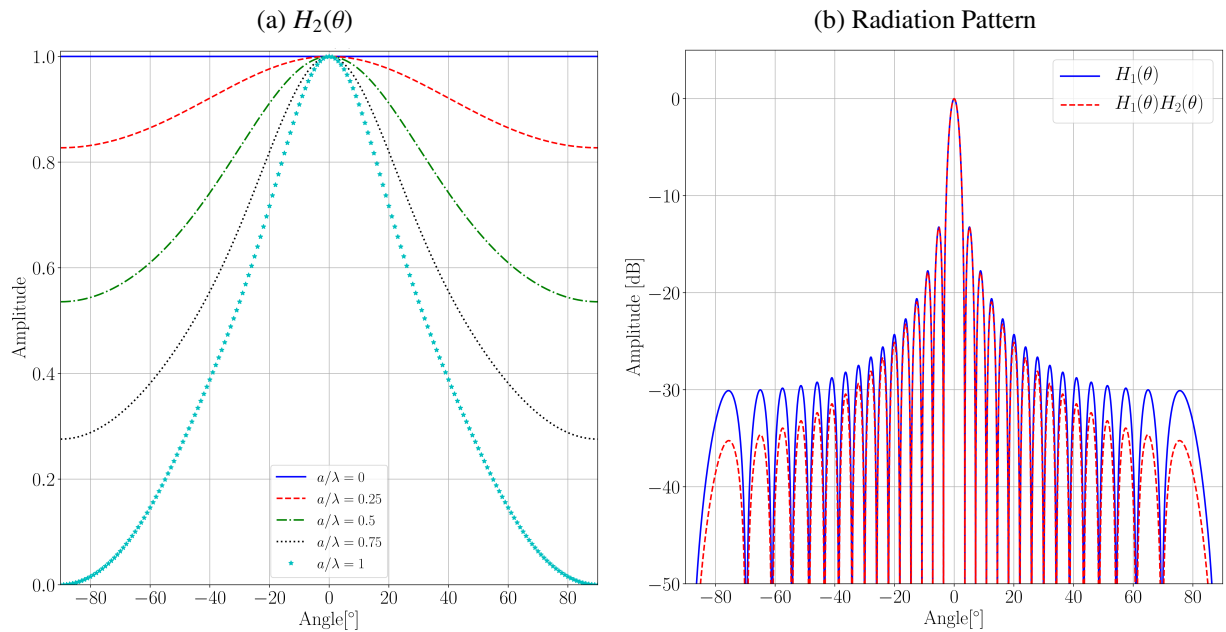
and considering the length  $L$  of the element, the directivity is given as (WOOH; SHI, 1999b):

$$H_2(\theta, \phi) = \left| \text{sinc}\left(\frac{\pi a \sin(\theta) \sin(\phi)}{\lambda}\right) \text{sinc}\left(\frac{\pi L \sin(\theta) \sin(\phi)}{\lambda}\right) \right|. \quad (25)$$

Figure 8(a) illustrates the irradiated energy by an element for different widths. As it can be seen, punctual elements ( $a/\lambda = 0$ ) irradiate the energy in all directions. In contrast, as the element size increase, the irradiated energy is more concentrated at smaller angles, in front of the element.

This directly affects the radiation pattern narrowband response of the array, where the energy irradiated by an element modulates the energy irradiated by the array. In Figure 8(b) this behaviour can be seen comparing the radiation pattern considering an array with 32 punctual elements (illustrated in blue) and the radiation pattern considering the same amount of elements but with elements with width  $a = 0.5\lambda$ . It is important to highlight that, in ultrasonic applications, elements are pulsed excited, and the wideband response would be a more reliable

Figure 8 – (a) Energy irradiated by an element with different  $a/\lambda$  values: (b) Radiation Pattern narrowband response modulated by the directivity of the element with a  $a = 0.5\lambda$  width.



Source: Author

simulation. However, the narrowband response illustrates the worst-case scenario, highlighting the arrays' characteristics and helping to explain the characteristics of the arrays' responses.

Although the energy irradiated by a finite dimension element is normally not taken into account when designing sparse arrays, it is good to know how the elements behave experimentally. In this way, all radiation pattern simulations presented in this work consider punctual elements.

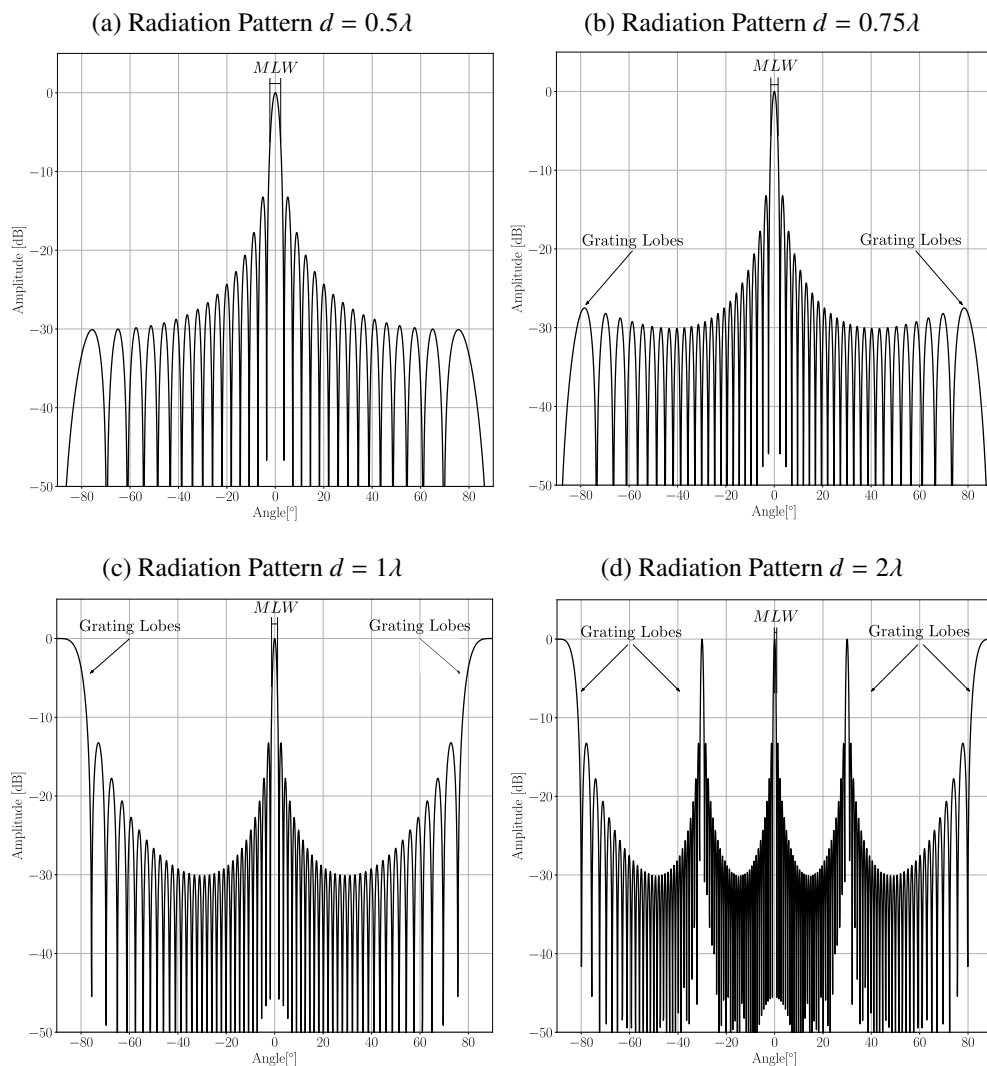
### 2.1.2 Sparse array

Sparse arrays are an alternative to increasing the lateral resolution without increasing the electronic complexity. To understand the consequences of using sparse arrays, the narrowband radiation pattern can be analysed considering punctual elements. Figure 9 illustrates four radiation patterns of a 32 elements arrays where the pitch are different for each case. In (a), the radiation pattern generated from an array with a pitch equal to  $0.5\lambda$  (32 elements FPA) has the biggest  $MLW$ , and the side lobes' intensities decrease as it gets away from the main lobe. When the pitch increases to  $0.75\lambda$  (b), the  $MLW$  decreases from  $2.2^\circ$  to  $1.5^\circ$ , but the side lobes intensities stop decreasing as it gets far from the main lobe and increase at the extreme angles. These lobes are called grating lobes, which are caused by the waves of the array summing in unwanted directions.

In Figure 9(c), the pitch is increased to  $1\lambda$ , and it is possible to see that the grating

lobes at  $\pm 90^\circ$  have the same intensity as the main lobe. In (d), the pitch is  $2\lambda$ , and the radiation pattern has additional grating lobes at  $\pm 30^\circ$ . In contrast, the *MLW* in these cases reduces to  $1.1^\circ$  and  $0.6^\circ$ , respectively. As it can be seen, increasing the size of the array by just increasing the pitch will reduce the size of the *MLW* leading to better lateral resolution. However, the energy irradiated by the element will sum in different regions, which might result in images with high-intensity artefacts that can lead to misinterpretations of the images.

Figure 9 – 32 elements radiation pattern considering a pitch equal to: (a)  $0.50\lambda$ , (b)  $0.75\lambda$ , (c)  $1\lambda$  and (d)  $2\lambda$ .

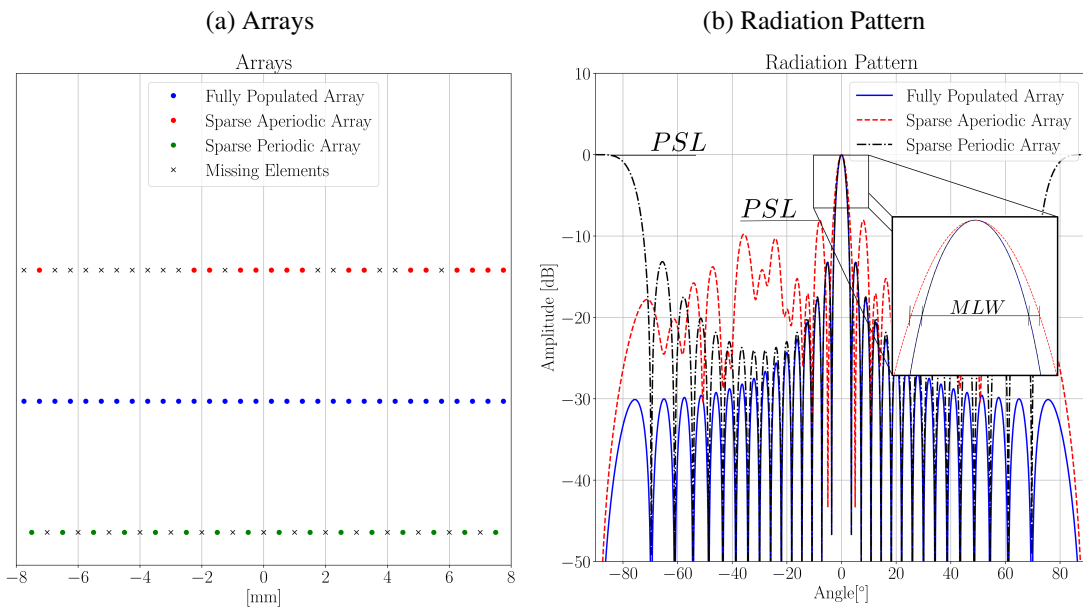


Source: Author

One way to decrease the intensity of the grating lobes is by breaking the periodicity of the elements by using sparse aperiodic arrays, where the pitch of the elements will be different from each other. Figure 10 (a) illustrates two sparse array configuration. In red dots, a sparse aperiodic array where 16 elements were randomly removed from a 32 FPA. In green dots, 16 elements sparse periodic array of  $1\lambda$  pitch, which has the same length as the 32 FPA. Figure 10 (b), illustrates the radiation pattern created from these sparse configurations where the *MLW*

and  $PSL$  are highlighted. It is possible to see a reduction in the grating lobes' intensity with an exchange of the rise of side lobes. Moreover, the  $MLW$  is slightly lower for the sparse periodic array as it has the same length as the 32 FPA.

Figure 10 – (a) Fully populated array (blue dot), sparse aperiodic array (red dot), sparse periodic array (green dot) and the missing elements to complete a fully populated array. (b) the radiation pattern narrow band response of the presented arrays with the  $MLW$  and  $PSL$  highlighted.



Source: Author

Works such as Goss et al. (1996) propose to randomly select 64 in 108 elements in a 2D sparse array to obtain a sparse array configuration. Although the focus of the work is to use arrays in focal heating, the study of the radiation patterns presented shows a reduction in the intensity of the grating lobes, but these random configurations produce sparse arrays with unpredictable performance as the side lobes summed in different regions.

Search mechanisms can be a better strategy to find sparse array configurations. They are composed of three parts: the codification process, where the problem is encoded into a mathematical representation. For example, the FPA illustrated in Figure 10 (a) can be encoded as a binary vector with 32 positions. In this case, it will be a vector with 32 ones as the ones indicate that the elements are used in the imaging process. In the sparse array illustrated in Figure 10 (a), the 32 binary vectors will have zeros indicating the elements not used and ones indicating that the elements are used.

The second part is the fitness function (FF), a mathematical function that translates the encoded configuration into a number. The FF translates the sparse configuration to how well it can be to image. In this way, two configurations that have different FF can be compared, and with this value, it is possible to say which one is better to image. Creating this FF is a

Table 1 – Comparison between search algorithm using the fitness function proposed by Trucco (1999).

Metaheuristic	Fitness of the best
Simulated Annealing	34,714
Genetic Algorithm	65,378
Particle Swarm Optimization	29,152
Harmony Search	34,823
Whale Optimization Algorithm	70,455
Bat Optimization Algorithm	31,505
Arithmetic Optimization Algorithm	28,976

difficult task, as most of the time it is necessary to quantify an image or a signal with different amplitudes into a number. The codification strategy and the FF are used in a search engine that will search different configurations aiming to minimize or maximize the FF. The search engine is called metaheuristics, and more information is provided in Appendix A.

One of the classic algorithms used for this problem is simulated annealing (KIRKPATRICK et al., 1983). Murino et al. (1996) proposed using the energy of the narrowband radiation pattern response as a fitness function and use simulated annealing to find configurations of sparse linear arrays and also the apodization of the elements. Trucco (1999) proposed a similar strategy to optimize both the elements in 2D sparse arrays and the weight coefficients (apodization). In that work, the FF proposed by the author uses the mean squared error of the radiation pattern, where one signal is the radiation pattern of the sparse array, and the other is the desired radiation pattern, which is a matrix array where the elements has  $0.5 \lambda$  pitch. In both strategies, the positions of the elements are predefined, which creates a grid, and the search engines select which elements are going to work.

The search algorithm does not guarantee that the best result is found, and may vary among different algorithms. For example, the Genetic Algorithm (HOLLAND, 1992), Particle Swarm (KENNEDY; EBERHART, 1995), Harmony Search (ZONG et al., 2001), Whale Optimization (MIRJALILI; LEWIS, 2016), Bat Optimization (YANG, 2010) and Arithmetic Optimization Algorithm (AOA) (ABUALIGAH et al., 2021) were implemented to work with the fitness function proposed by Trucco (1999). Table (1) gives the FF of the best sparse array found using the respective algorithm. As it can be seen, the results found by the algorithms vary considerably, with the AOA finding the best result.

Trucco (2002) used this same optimization logic involving simulated annealing to find sparse linear array configurations. However, the author created a fitness function based on the radiation pattern wideband response. The author claimed the wideband response is closer to real ultrasound applications and, therefore, better layouts could be achieved. Nevertheless, the author observed that processing the wideband response is time-consuming and getting valuable information from the wideband response is more challenging.

In these works, a common problem is to control the number of elements selected in the array. The way that the search problem is constructed, it is required to add a penalization function in the FF to limit the number of active elements selected in the array during the search problem construction. This penalization function is a conditional statement inserted in the algorithm that if the current configuration analysed has more active elements than the predefined at the beginning of the search, an arbitrary constant is added to the fitness value. Although the penalization strategy can limit the number of elements selected in the sparse array, it is difficult to tune the penalization factor.

A different optimization algorithm was used by Haupt (1994), where the author used the genetic algorithm to find sparse configurations for linear and matrix arrays. Although the work is for antennas, the fitness function is based on the radiation pattern narrowband response, which shares the same theory as ultrasonic arrays, and it can be used as an example. The author proposes to use the peak sidelobe (PSL) as a fitness function. The genetic algorithm has the advantage in comparison to simulated annealing because the algorithm works with binary representation, so 0 is used to illustrate that the element in a certain position is turned off and 1 when the element is on. For example, the binary representation of the sparse array illustrated in Figure 10 (a) would be [0, 1, 0, 0, 0, 0, 0, 0, 0, 0, 0, 0, 1, 1, 0, 1, 1, 1, 1, 1, 0, 0, 1, 1, 0, 0, 1, 1, 0, 1, 1, 0, 1, 1, 1, 1]. In the work presented by Haupt (1994), a penalization strategy was not used, and for a 200 element FPA and a 10x20 matrix array, the author achieves a 25% reduction in the number of elements for the linear array and 46% element reduction in the 2D array.

The genetic algorithm was also used by Yang et al. (2006) to optimize the linear array. The FF proposed by the authors is based on the radiation pattern narrowband response where the two pieces of information are extracted from it: the main lobe width (MLW) and the peak sidelobe (PSL). The two features are combined using a Scalarization Method, which is a multi-objective strategy (MURATA et al., 1996). Equation (26) illustrates the fitness function used by the authors.

$$FF = k_1 MLW + k_2 PSL, \quad (26)$$

where  $k_1$  and  $k_2$  are the weights used to focus the search. If the operator wants to focus on better lateral resolution, a higher value in  $k_1$ , with respect to  $k_2$ , would be defined.

The equation (26) has been used in different works to find sparse linear array configurations. Hu et al. (2017) proposed an imaging algorithm that corrects the divergence of the sound beam and uses the same methodology proposed by Yang et al. (2006). The difference from the previous study is that the authors only find sparse emitters configurations and used a 32 FPA as a receiver.

In the article published by Hu et al. (2018), the authors propose the use of a different variation of the genetic algorithm called Almost Different Sets Genetic Algorithm with (26) to

find emitters and receivers sparse linear arrays configurations and also proposed an algorithm to enhance the ultrasonic image by post-processing it interpolating its pixels

Different algorithms were also used, Zhang et al. (2020) proposed to adapt the particle swarm optimisation algorithm (PSO) into a binary search mechanism and used the same FF described in (26) to find linear sparse configurations.

For 2D arrays, metaheuristics have been used to design the sparse arrays. Trucco (1999) uses simulated annealing algorithm to select elements from 3 pre-defined matrix arrays with 112, 200 and 3228 elements. The simulation method used by the author is the radiation pattern narrowband response, where the FF created is the error between the radiation pattern generated by a sparse array and the pre-defined matrix array. Moreover, a penalization function is added to control the elements selected from the matrix array. Chen et al. (2011) refined this FF by changing the penalization function and expanding the analysis for multiple foci to find arrays with the same quality as Trucco (1999) but with fewer selected elements.

In the article published by Diarra et al. (2013), this fitness function is used with a simulated annealing-based algorithm to design 2D sparse array for non-grid arrays, where the elements are placed anywhere in the space. The authors achieved the same lateral resolution with reduced side lobes intensities compared to the proposed works. One drawback of this strategy is the manufacturing process. Although CMUT technology enables the array manufacturing (ORALKAN et al., 2003), the cost of doing it is high which is necessary to increase production to compensate for the cost. Later in the same research group, Roux et al. (2017) propose a new fitness function based on the multi-depth focal points of the radiation pattern wideband response, which needs to define the element impulse response and might limit the sparse array to work under a specific setting.

The optimization algorithms are used to find sparse array configurations using an FF that evaluates the configurations. Another strategy used in array design consists in evaluating the coarray shape to create different emitter and receiver sparse arrays.

### 2.1.3 Coarray

The Coarray or effective aperture is a representation of a receiver aperture that would produce an identical image if the transmit aperture was considered a point source (omnidirectional radiation) (GEHLBACH; ALVAREZ, 1981). It is a mathematical tool that merges the array used for emission and reception and can be used to get information about the ability of the array imaging. By calculating the DTFT of the coarray, the two-way or pulse-echo radiation pattern narrowband response is calculated, which is the product of the radiation pattern of the emitting array with the receiving array (LOCKWOOD et al., 1996a).

The coarray is defined as the convolution of the emitter and receiver apertures (GEHLBACH; ALVAREZ, 1981; LOCKWOOD et al., 1996a; LOCKWOOD et al., 1996b; KARA-

MAN et al., 2009). Considering that the array elements are impulses in the space, each coarray element is the product of an emitting and receiving element of the array, which is also an impulse, and the coarray position is the sum of the emitting position with the receiving position. In this way, the coarray can be calculated as a set of its positions, where each position is calculated as:

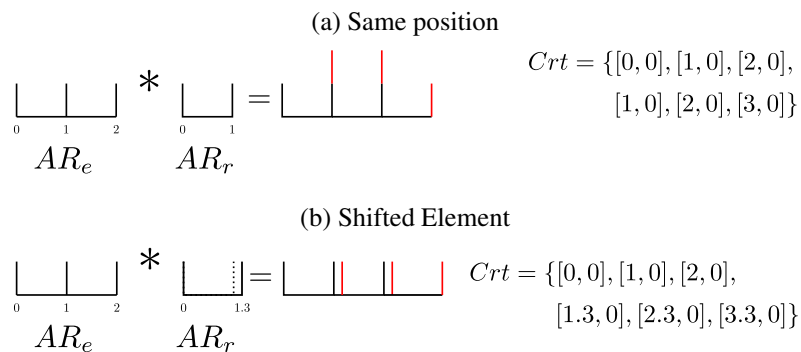
$$Crt = \{\vec{C}_{er} = \vec{e}_e + \vec{e}_r\} \quad \forall \quad \vec{e}_e \in AR_e, \quad \vec{e}_r \in AR_r, \quad (27)$$

where  $\vec{C}_{er}$  is a coarray element generated by the respective emitter  $e$  and the receiver  $r$ ,  $AR_e$  the position set of the emitter elements,  $AR_r$  the position set of the receiver elements, and  $e_i = (x_i, y_i)$ , which is the  $XY$  position in the plane.

Figure 11 illustrates two cases of  $Crt$ . In both cases, as the linear array is analysed,  $y$  is zero. In (a), the convolution of the apertures  $AR_e$  and  $AR_r$  generates a coarray with a triangular shape. The elements in the linear arrays are in one grid and the positions on the coarray overlap. In (b), one element of  $AR_r$  is displaced by  $0.3\lambda$ . In this example, the coarray elements do not overlap, where the first row of  $Crt$  gives the positions of the coarray elements considering the  $\vec{e}_1$  of  $AR_r$  and the second row gives the positions of the  $\vec{e}_2$  of  $AR_r$ .

The weight of each coarray element is the number of emitter/receiver pairs that are coincident at the same position, and the analysis of its shape can be used to estimate the dynamic range and lateral resolution of the imaging system (DRINKWATER; WILCOX, 2006; HOCTOR; KASSAM, 1990). For 2D non-grid arrays, such as the Fermat spiral and annular segmented arrays, this superposition is very rare to occur, turning the analysis of its shape difficult. In this way, this definition of coarray is important as it will be further used to analyse the coarray elements' distance and identify elements that are closer enough to be considered in the same position.

Figure 11 – Illustration of  $Crt$ . (a) the array elements are periodically spaced (in a grid). (b) One reception element is shifted by 0.3.

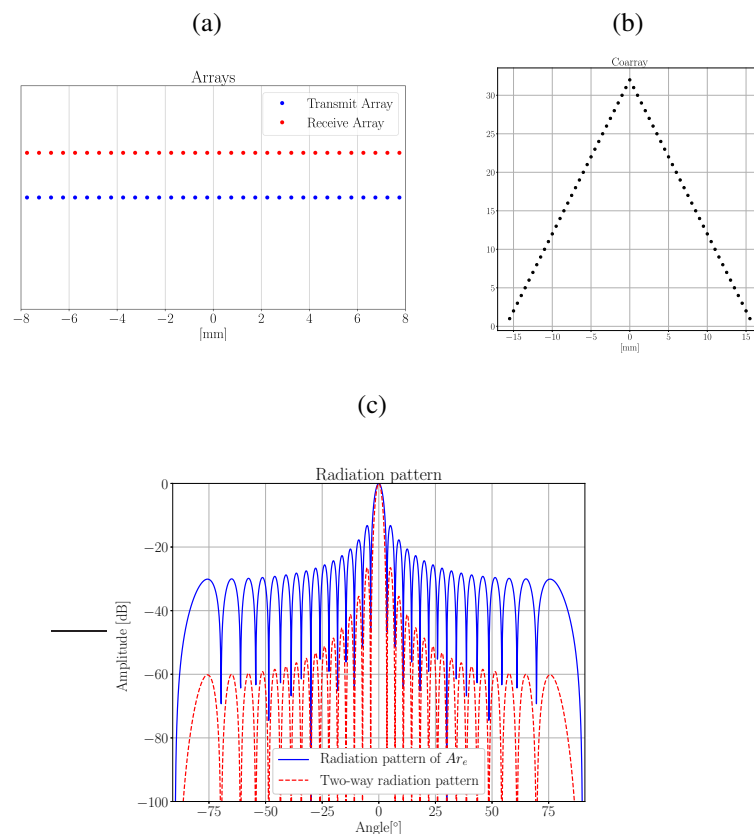


Source: Author

Considering a linear FPA with 32 elements, where a rectangular apodization is used, and all elements are used for transmission and reception (Figure 12(a)), the coarray  $Crt$  ge-

nerated has 1024 elements where summing the elements that overlaps has a triangular shape (Figure 12(b)). The radiation pattern narrowband of the transmit array ( $AR_e$ ) and the Coarray ( $Crt$ ) are illustrated in Figure 12(c), where the two-way radiation pattern has a lower  $MLW$ ,  $3.20^\circ$  in comparison to the radiation pattern of the emitter FPA ( $4.39^\circ$ ), and lower side lobes levels.

Figure 12 – (a) Transmit and Receiver Linear FPA with 32 elements. (b) the coarray formed from the two arrays with triangular shape with all elements respecting a pitch  $0.5\lambda$ . (c) the radiation pattern of the transmit array and the coarray (two-way radiation pattern).



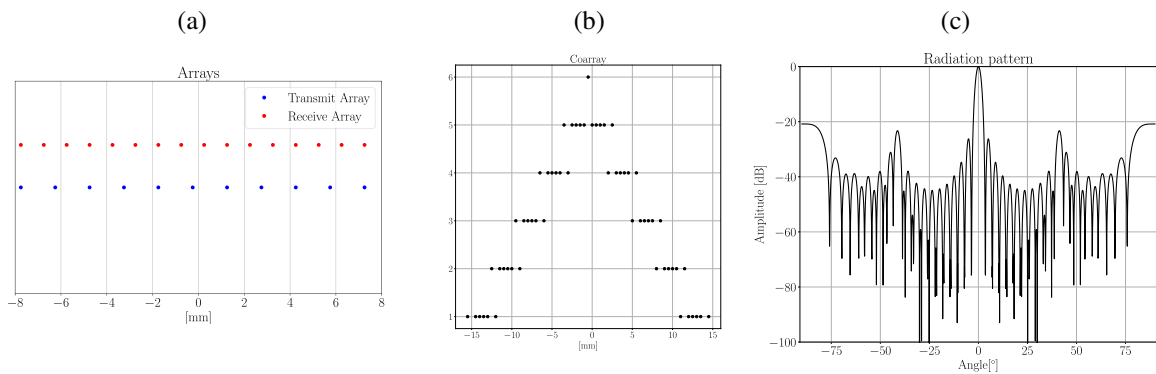
Source: Author

The analysis of the coarray is important and was used to design sparse array configurations. Lockwood et al. (1996a) used two linear sparse arrays, one working in emission and the other working in reception to create a coarray where the elements have a  $0.5\lambda$  pitch, although the shape of the coarray created is uneven. The spacing between the elements is based on the Vernier scale, the same scale existing in rulers and pachymeters.

Figure 13 (a) illustrates two sparse periodic arrays created based on the Vernier scale, one used for emission and the other for reception. The transmitting array has a  $1.5\lambda$  and the receiver has a  $1\lambda$  pitch. These two configurations are periodic and have grating lobes with the same intensity as the main lobe in the radiation pattern narrowband response. However, the resultant coarray illustrated in Figure 13 (b) resembles a triangular shape and the elements

respect the pitch of  $0.5\lambda$ . The two-way radiation pattern is illustrated in Figure 13 (c), where it is possible to see the reduction in the grating lobes intensities.

Figure 13 – (a) Sparse Transmit and Receiver Linear arrays created based on Vernier distribution, (b) the coarray created where it has the triangular shape, respects a pitch  $0.5\lambda$  but it has adjacent elements that alternate the amplitudes and (c) the two-way radiation pattern of the coarray created.



Source: Author

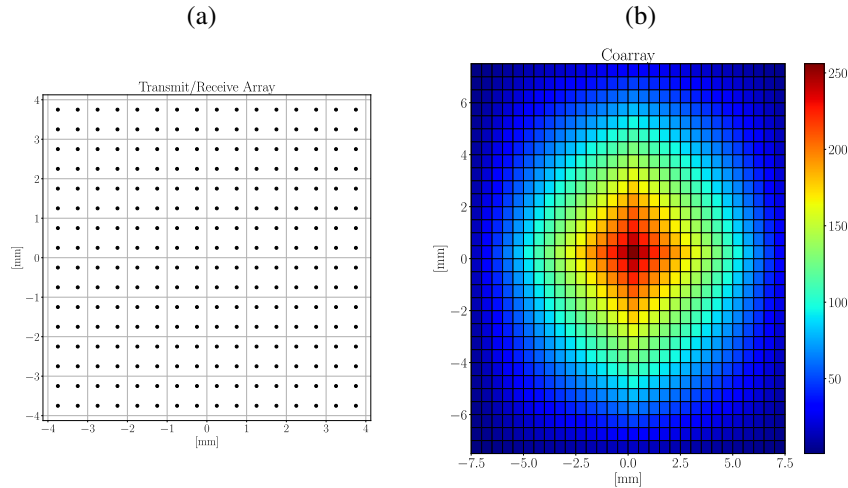
Another example of using sparse periodic arrays to create a desired coarray is given by Mitra et al. (2010), where the authors used the concept of factorization of polynomials to place the emitter and receiver elements of arrays. The problem in the arrays created using this methodology is the concentration of emitters on one side of the array, which unbalances the energy irradiated and might generate non-linear artefacts in the images.

For bidimensional arrays, a 2D matrix array with  $16 \times 16$  elements is illustrated in Figure 14(a) as an array example. Figure 14(b) illustrates the coarray formed from the matrix array. As it can be seen by analysing the colorbar, the coarray has a square-based pyramidal shape, similar to the example presented using linear arrays (Figure 12(b)).

Following the strategy to use periodic sparse arrays and create desired coarrays, Lockwood et al. (1996b) also proposed the use of the Vernier scale to design sparse planar arrays aiming at a desired coarray shape. Karaman et al. (2009) proposed four strategies using different emitter and receiver arrays to create a minimum redundancy coarray, where the elements of the coarray avoid overlapping. Figure 15 illustrates one example presented in that work. In (a), the elements of the emitter array are placed at the vertical at the extreme boundaries, with  $0.5\lambda$  pitch. In (b), the elements of the receiver array are placed horizontally at the extreme boundaries, with  $0.5\lambda$  pitch. The coarray generated from these two arrays is illustrated in Figure 15 (c), where it is possible to see the majority of the elements have amplitude one (in white colour), which indicates the minimum redundancy.

Although this strategy almost creates a coarray in which elements are unitary, this analysis is restricted to matrix arrays, where the elements overlap and can be summed. In arrays where the elements are in a non-grid, for example, Fermat spiral arrays (Figure 2(b)), the coar-

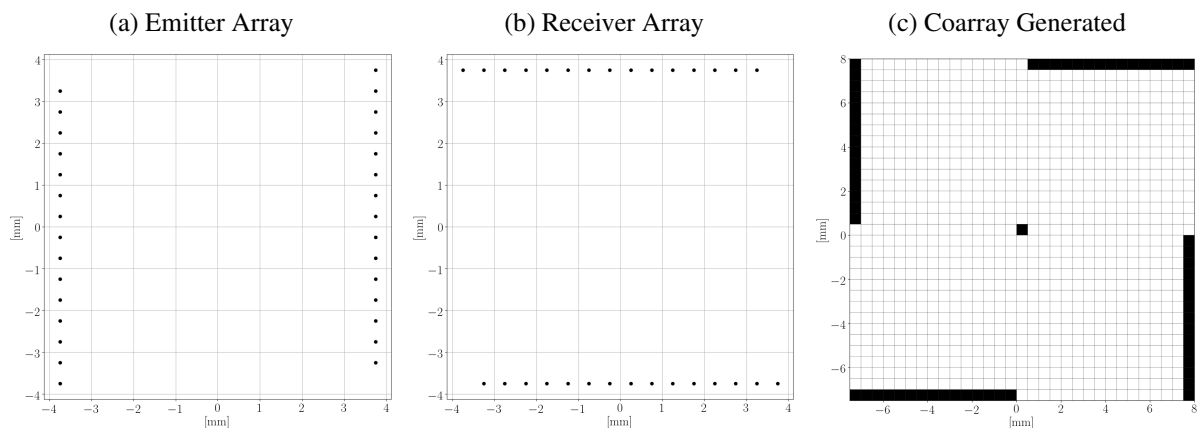
Figure 14 – (a) Matrix array with 256 elements ( $16 \times 16$ ) where the adjacent elements in the  $x$ -axis and  $y$ -axis have a pitch equals to  $0.5\lambda$  ( $\lambda = 1[mm]$ ) and the elements diagonally adjacents have a pitch equals to  $0.70\lambda$ . (b) The coarray is created from the matrix array which has a pyramidal shape.



Source: Author

ray elements do not overlap and the redundancy cannot be analysed in the same way.

Figure 15 – An example of the minimum redundancy array (KARAMAN et al., 2009) where (a) 30 elements are disposed of two vertical lines and (b) 30 elements are disposed of two horizontal lines where the elements in the lines have a pitch equal to  $0.5\lambda$  ( $\lambda = 1[mm]$ ). (c) the coarray is generated from these two apertures where the majority of the elements have amplitude one.



Source: Author

The coarray is a mathematical tool that can be used to evaluate sparse configurations. It is considered a spatial apodization as the two-way radiation pattern is the Fourier transform of the amplitudes of the coarray (LOCKWOOD et al., 1996b). Another alternative to evaluate sparse configurations is the point spread function (PSF), which is the simulation of a reflector point in the medium and gives information about how a sparse array can image. Before ex-

plaining how the PSF is generated, which will be done in section (2.2.3), first, it is necessary to know how an ultrasonic image is generated.

## 2.2 ULTRASONIC IMAGING

The basic principle of ultrasonic images is to use a transducer with a single element to emit an ultrasonic wave in the medium, and, in the case of reflection (change of density), the reflected mechanical wave is converted to an electrical signal by the same transducer, amplified, and then sampled. By doing this operation in different areas, creating a sweep, the acquired signals can be used to create an image.

Figure 16 illustrates two simple imaging strategies. In (a), where the B-scan is represented, the transducer is shifted and activated in the  $x$ -axis. The irradiated wave reflects at the end of the object or the hole. With the acquired data, a brightness image can be created in the  $x$  and  $z$  axis, as illustrated in Figure 16 (b). The C-scan is illustrated in (Figure 16(c)) where the transducer shifts in the  $x$  and  $y$  region. In this case, a section of the image in a certain depth is generated (Figure 16(d)) .

The use of a single transducer to generate images is a simple example to understand the principle of ultrasonic images. In practice, images generated by a single element would have low lateral resolution and contrast. Moreover, the element needs to be mechanically moved, which decreases the frame rate and creates a margin for positioning errors. Arrays are used to overcome these problems, and two main strategies are used for data acquisition and imaging: the Phased Array and the Synthetic Aperture.

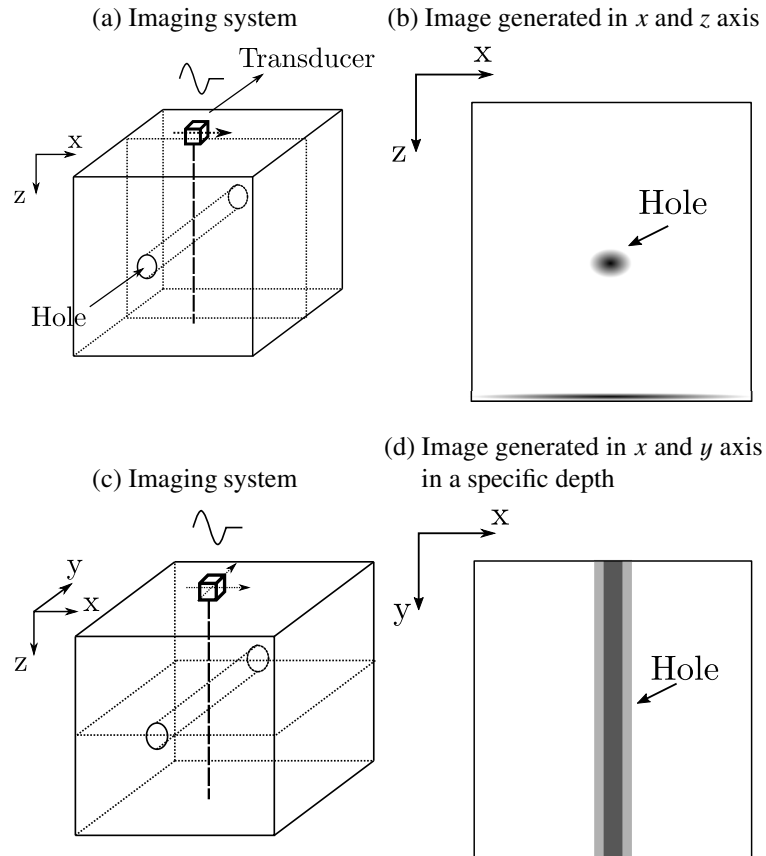
### 2.2.1 Phased array

In Phased Array systems, the elements in the array can be pulsed independently, and depending on the relative phases of element excitations, the ultrasonic beam can be steered or focused. The most common inspection modality is the B-scan (Figure 17(a)), where a subset of elements is used to inspect the object, and the reflected signals are plotted as intensity (DRINKWATER; WILCOX, 2006). This inspection modality is similar to the monolithic illustrated in Figure 16(a). However, the difference that the scan is done electronically and the mechanical movement is reduced.

A different inspection modality is created when delays in the activation of the elements are applied. Figure 17(b) illustrates the focused B-scan, where the elements are fired with delays between each other and the beam focused in a region. The delays can also be used to create a sector scan (Figure 17(c)), where the beam is steered at an angle and objects can be scanned at positions not directly in front of the array.

One drawback of Phased Arrays is that the elements need to work in parallel, increasing

Figure 16 – Simple imaging system using a single element transducer. (a) representation of the imaging system where the transducer is shifted only in the  $x$  axis and the resulting image (b) created in the  $x$  and  $z$ -axis. (c) An imaging strategy where the transducer moves in  $x$  and  $y$ -axis. (d) the segmented image generated in a different depth.



Source: Author

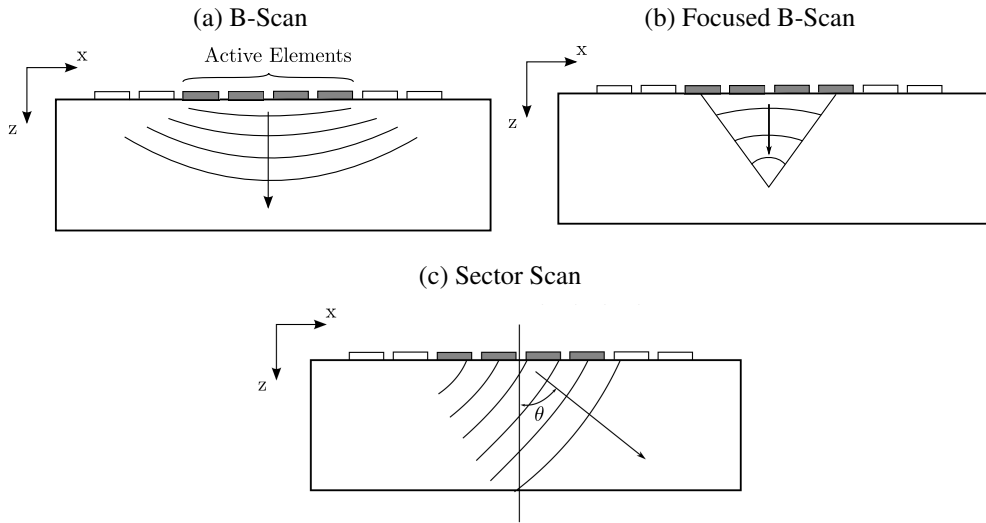
electronic complexity. An alternative to overcome this problem is the use of the Synthetic Aperture technique.

### 2.2.2 Synthetic aperture

Synthetic aperture is an imaging technique based on the synthetic aperture radar, where the reflected electromagnetic wave of a region is sampled in different positions, and an image of a region is created (JENSEN et al., 2006). Figure 18 illustrates the working principle of this technique, an antenna is attached to the aircraft that moves above an area. The antenna emits and receives the waves in different positions and the data acquired is processed to create an image.

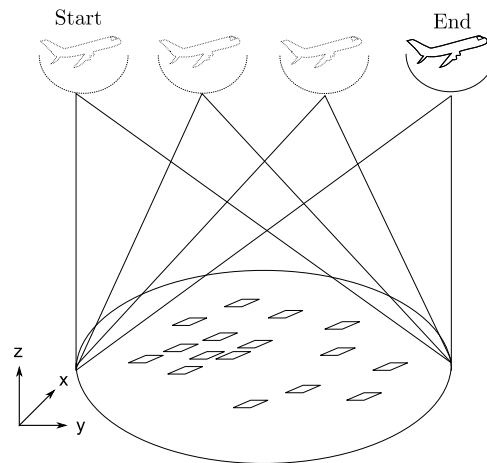
In synthetic aperture, the elements of the array are sequentially emitted, which copies how the antenna is used in Figure 18. An illustration of the SA technique is given in Figure 19. At the first stage, element 1 emits, and all array elements receive. Afterwards, element 2 emits, and all array elements receive. This process is repeated for all  $N$  elements, which creates a

Figure 17 – Phased Array inspection modalities. (a) B-scan. (b) Focused B-scan. (c) Sector Scan.



Source: Author

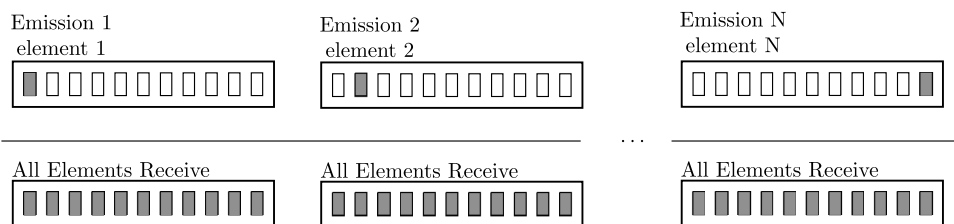
Figure 18 – Synthetic Aperture Radar.



Source: Author

dataset with the echoes of all combinations of emitters and receivers, namely full matrix capture (*FMC*) (HOLMES et al., 2005).

Figure 19 – Synthetic Aperture.



Source: Adapted from Jensen et al. (2006)

After the process of signal acquisition, an algorithm needs to be used to create an ul-

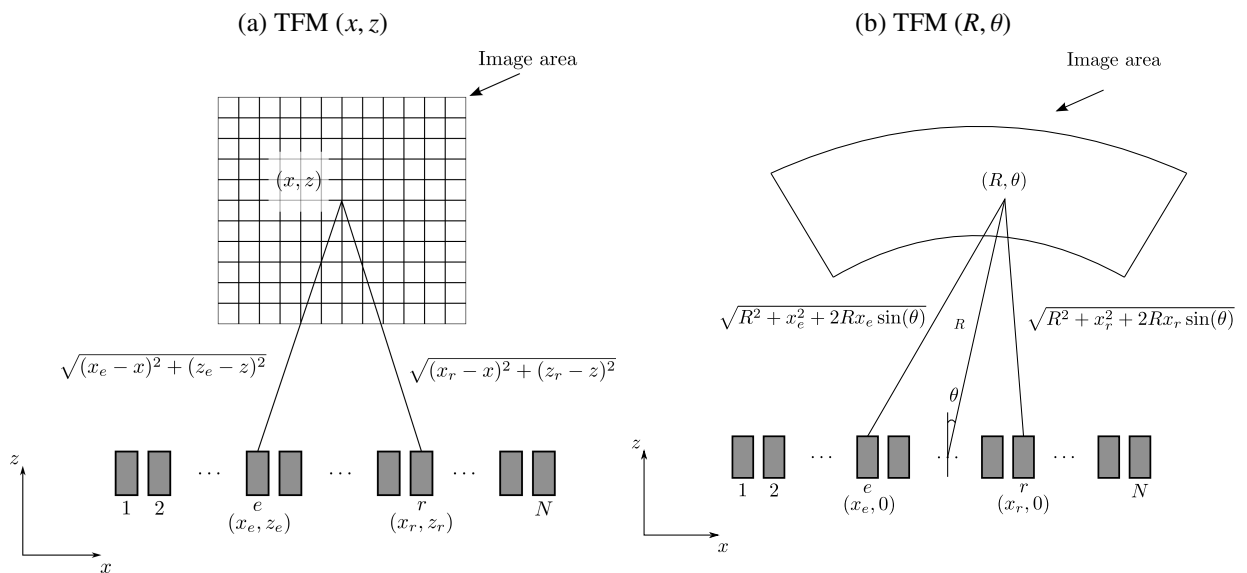
trasonic image, where the gold standard algorithm is called Total Focusing Method (TFM) (BANNOUF et al., 2013). This algorithm consists of applying delays and summing signals samples. Equation (28) gives the mathematical operation to calculate the TFM:

$$I(x, z) = \frac{1}{N^2} \left\{ \left[ \sum_{e=1}^N \sum_{r=1}^N w_{er} s_{er}(\tau_{er}(x, z)) \right]^2 + \left[ \sum_{e=1}^N \sum_{r=1}^N w_{er} \hat{s}_{er}(\tau_{er}(x, z)) \right]^2 \right\}^{1/2}, \quad (28)$$

where  $I(x, z)$  is the envelope of the amplitude image at a given  $(x, z)$  position,  $w_{er}$  the apodization,  $s_{er}(t)$  the ultrasonic signal related to the emitter  $e$  and receiver  $r$ ,  $\hat{s}_{er}$  the Hilbert transform of  $s_{er}(t)$ , and  $\tau_{er}(x, z)$  the time of flight from the emitter  $e$  to the pixel  $(x, z)$  back to the receiver  $r$ .

Figure 20(a) illustrates how the TFM algorithm is calculated. The image area is discretised in a grid in the  $x, z$  plane, and the amplitude of the image is calculated at all points. At each point, the Euclidian distance from the emitter element  $e$  to a point in the grid  $(x, z)$  is calculated and summed to the distance from the point  $(x, z)$  to the receiver element  $r$ . This value is then divided by the velocity of the sound in the medium ( $c$ ) to find the time of flight  $\tau_{er}$ . Afterwards, the respective amplitudes at the time  $\tau_{er}$  are summed.

Figure 20 – Total Focusing Method (TFM). Representation in  $(x, z)$  grid (a), and in  $(r, \theta)$  grid (b).



Source: Author

Equation (28) gives the TFM calculate in respect to cartesian coordinates, which can be changed to polar using the cosine rule (Figure 20(b)). In this case, instead of using the notation  $I(x, z)$ ,  $I(R, \theta)$  is used, where  $R$  is the radius and  $\theta$  the angle that the image is calculated.

The synthetic aperture technique reduces the electronic complexity and system cost as the emission and reception can be multiplexed. At the minimum, it is only necessary one Ana-

log to Digital (A/D) converter, but, in exchange, the acquisition time increases as  $N^2$  emissions are required. This long-duration acquisition time might turn impractical for the use of this technique; therefore, the solution is to use more A/D converters and add multiplexers to enable several receivers to work in parallel. However, if the number of array elements increases, followed by the number of A/D converters and multiplexers, the system cost and data volume escalate at an unfeasible level.

The sparse array is one solution for this problem, where some elements are placed in a large area. However, there is another alternative. Some emitters/receivers combinations can be removed from the acquisition process, which creates an acquisition strategy different from FMC. With fewer combinations of emitters and receivers, the number of elements in the array can increase, covering a larger area, and the number of receiver channels working in parallel can be managed, which helps to remain the system cost and data volume at an acceptable level.

### 2.2.3 Point Spread Function

A different strategy to analyse the arrays' ability to generate an image is the Point Spread Function (PSF). In this method, a point reflector is placed in space and, using simulated data, the ultrasonic image is generated (DRINKWATER; WILCOX, 2006). The data set of the combinations of emitters and receivers can be simulated by time-shifting the electrical input response of the transmitting element to the time of flight of the combination of emitter and receiver element. In Figure 21(a), an electrical input response defined using equation (18) is illustrated. In this example  $BW = 0.5$ ,  $u_0 = 1$ ,  $f_c = 3.5$  MHz, and  $f_s = 35$  MHz. where  $f_s$  is the sample frequency.

The shift operation can be done in different ways, for example, the electrical signal  $g(t)$  can be convolved with a time-shifted impulse  $\delta(t - \tau_{er})$ , or multiplied by an exponential in the frequency domain. Another alternative, used in this work, is to time-shift (18), which will be written as:

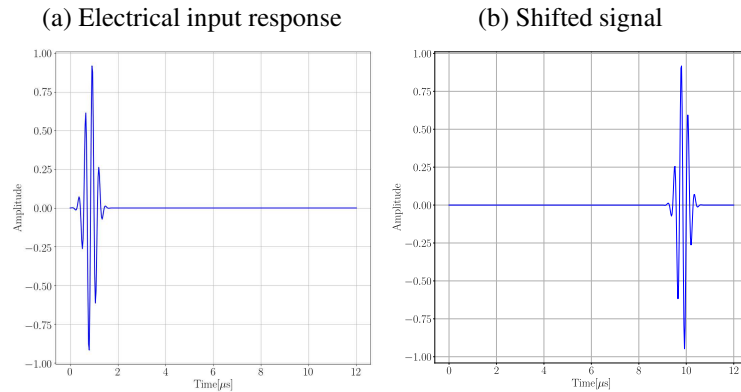
$$g(t - \tau_{er}) = u_0 e^{\frac{\pi^2 BW^2 f_c^2 (t - \tau_{er})^2}{1.2 \ln 10}} \sin(2\pi f_c (t - \tau_{er})), \quad (29)$$

where the electrical input signal shifted at the time  $\tau_{er} = 9\mu\text{s}$  is illustrated in Figure 21(b).

The shifted signals are calculated for all combinations of emitters and receivers that are going to be used for imaging, and the data set is created. Afterwards, an algorithm is used to generate the PSF. Figure 22 illustrates the PSF of a FPA with 32 elements, where the point reflector is placed at  $x = 0$  and  $z = 32\lambda$ . In (a) the image angle vary from  $-90^\circ$  to  $90^\circ$ . As the array is symmetric, it is only necessary to generate half of the angles (from  $0^\circ$  to  $90^\circ$ ). Figure 22 (b) illustrates only the half of the image that carries the same information as the full image. This strategy can be done only in symmetric arrays and is useful to reduce the simulation time.

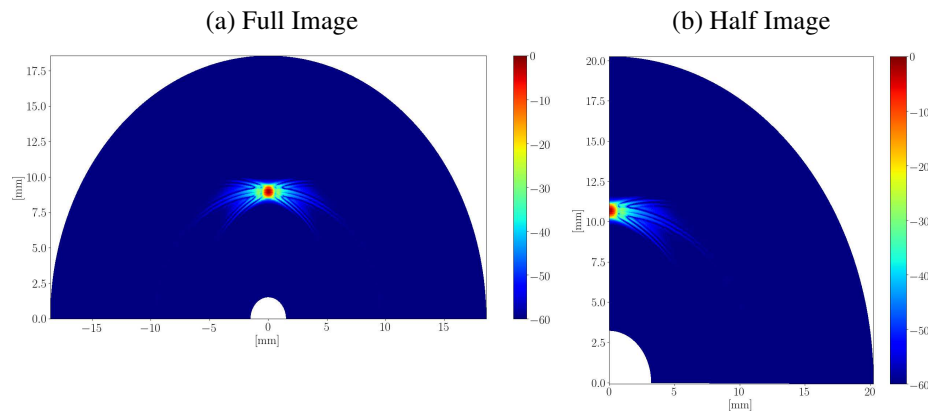
Figure 23 illustrates three cases of PSF created using only half of the image. (a) is the

Figure 21 – Data set simulation. (a) electrical input response. (b) shifted signal to the time of flight ( $9\mu$ ).



Source: Author

Figure 22 – PSF of an FPA with 32 elements. (a) Image generated from  $-90^\circ$  to  $90^\circ$ . (b) as the array is symmetric it is only necessary to generate half of the image (from  $0^\circ$  to  $90^\circ$ ).



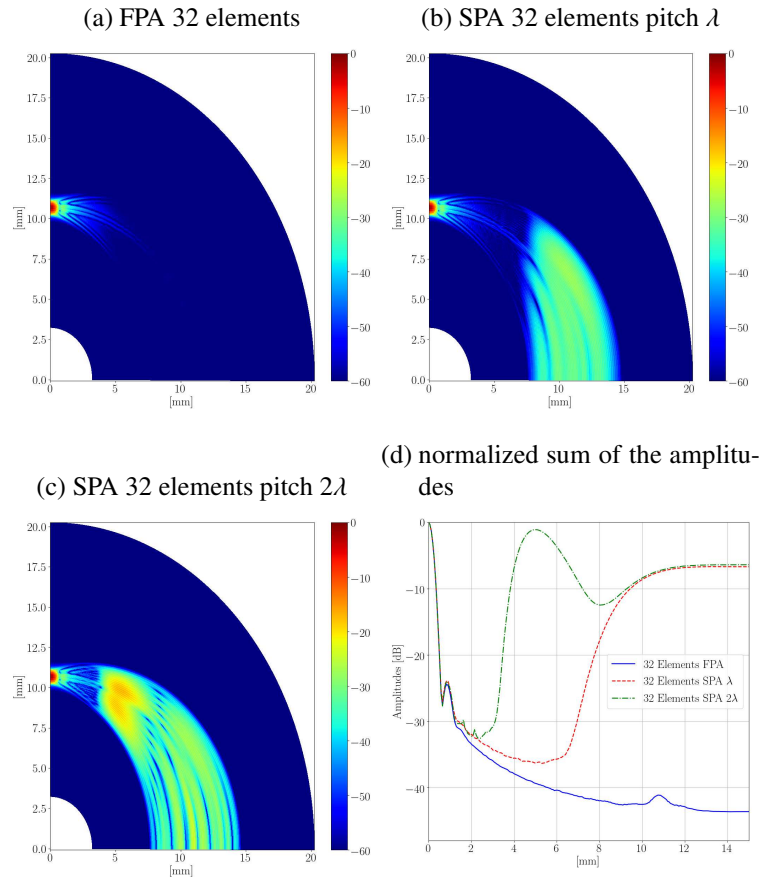
Source: Author

PSF of a FPA with 32 elements; (b) is the PSF of a 16-element sparse periodic array (SPA) with  $\lambda$  pitch, and (c) is the PSF of an 8-element SPA with  $2\lambda$  pitch. The point reflector remained the same size for all PSF, as the arrays have the same length. The number of signals processed and mathematical operations reduced from 1024 to 256 and 64, respectively, which decreases the time to generate images and resources. However, there is an increase in the intensity of the artefacts caused by the grating lobes.

Figure 23(d) illustrates the normalized mean in the axial direction of the PSFs. To create this graph, the PSF is stored in a matrix where the lines correspond to the radii  $R$  of the image and the columns of the angles  $\theta$ . At each  $\theta$ , the amplitudes of the radii are summed, resulting in a vector that is then normalized. It is possible to see an increase in the artefacts' intensity as the lateral resolution remained the same.

The energy concentrated in a region outside the point reflector is distributed by breaking

Figure 23 – PSFs of (a) FPA with 32 elements, (b) SPA with 32 elements a pitch  $\lambda$  and (c) SPA with 32 elements and pitch  $2\lambda$ . (d) normalized sum of the amplitudes.



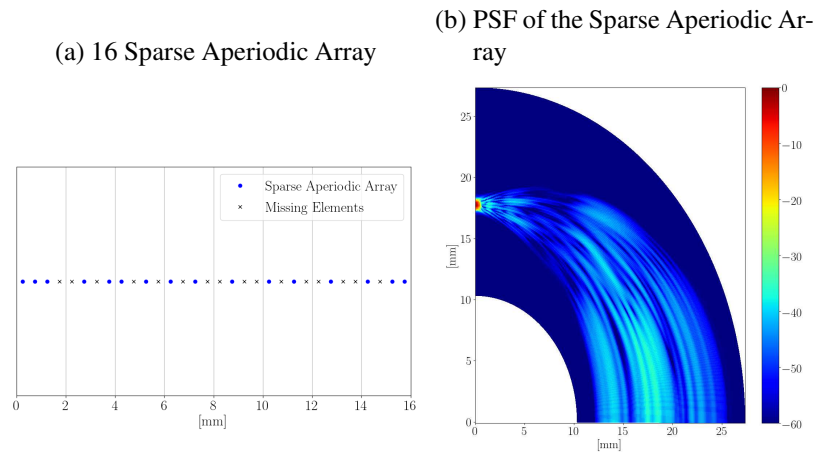
Source: Author

the periodicity of the elements. Figure 24 (a) illustrates a sparse array where 16 elements are selected from a grid with 32 positions that correspond to a FPA. The 32 elements sparse aperiodic array is created by mirroring the selected elements and, in Figure 24(b), the PSF of the sparse array is illustrated. The energy is not concentrated in an area as in Figure 23(b) and (d), but it spreads in the area beside the point reflector. This energy interferes with image quality by increasing the artefact's intensity. In this way, it is interesting to find a sparse array configuration that has improved lateral resolution with low energy besides the point reflector.

### 2.3 COMMENTS

In this chapter, the background to understand how arrays are used to create an ultrasonic image is given. The differences between FPA, sparse periodic and aperiodic arrays are presented, and the benefits of using sparse arrays to increase the speed to generate an image in exchange for image quality are discussed. As it could be verified, different combinations of sparse arrays can be obtained, making it impossible to test all the combinations. In this sense, there is a need to define strategies that find sparse array configurations while reducing

Figure 24 – (a) a sparse array created by selecting 16 elements in a grid corresponding to a 32 FPA. (b) the PSF of the sparse array where the energy besides the point reflector is not concentrated in a specific area.



Source: Author

the corresponding drawbacks. Moreover, the synthetic aperture technique requires a series of acquisitions combining all the emitter and receivers elements of an array. To reduce the acquisition time and decrease the time to generate an image, some emitters/receivers combinations can be removed from the acquisition process.

### 3 NEW STRATEGY FOR LINEAR SPARSE ARRAY DESIGN

In this chapter, the radiation pattern narrowband response fitness function (RP FF), which is the sum of the peak side-lobe (PSL) and main-lobe width (MLW), is used in different search algorithms. A new codification method for sparse linear arrays enables using search algorithms designed for continuous search values that found configurations with lower FF than using binary codification. The sparse arrays found are analysed, and inconsistencies in the results will lead to the development of a new fitness function (FF) based on the Point Spread Function (PSF) and based on the energy and entropy analysis. Then, this new FF is used in different search algorithms to analyse their performance in the sparse linear array design. Afterwards, the sparse configurations found using the radiation pattern fitness function and the proposed FF will be used to create a phantom image, which is a 128-element Fully Populated Array (FPA) imaged the phantom using the synthetic aperture technique acquiring a 128x128 FMC. Then, the sparse array images of the phantom were created using only the respective data of the FMC.

#### 3.1 FITNESS FUNCTION BASED ON THE RADIATION PATTERN AND SEARCH ALGORITHM ANALYSIS

The RP FF was defined in Chapter 2, where it is the sum of the main lobe width (MLW) with the peak side lobe (PSL). It is rewritten in (30) as:

$$FF = k_1 MLW + k_2 PSL, \quad (30)$$

where the weights  $k_1$  and  $k_2$  are set to 1 to create a balance between  $MLW$  and  $PSL$ .

This RP FF has been used in different works to evaluate sparse configurations (YANG et al., 2006; HU et al., 2017; HU et al., 2018; ZHANG et al., 2020), whereas Genetic Algorithm and Binary Particle Swarm were used as a search engine. Moreover, different algorithms have also been used to find sparse arrays, such as Simulated Annealing (TRUCCO, 1999) and Harmony Search (YANG; KIANG, 2015). In all cases, the weights  $k_1$  and  $k_2$  have been set to 1.

The search algorithms can be divided into 3 parts: the optimization codification, where a real problem is codified into a mathematical representation; the fitness function (FF), which will take a codified solution of the problem and evaluate it; and a search engine that will change this solution to optimize it and find better solutions with lower FF. In the sparse linear array optimization problem, the common method to represent the arrays is using the binary representation, where each position of this binary vector corresponds to an array element. For example, a vector with 128 positions filled with ones codes a 128 FPA, and a sparse array can be created by changing some of these ones to zeros. This creates a grid of  $0.5\lambda$  where the elements will be selected.

This codification strategy limits the type of search algorithms that can be used. For example, Genetic Algorithm (HOLLAND, 1992) was built to work with this type of codification, while other algorithms, such as Particle Swarm Algorithm (PSO) (KENNEDY; EBERHART, 1995), were designed to work with continuous values. Although there are strategies to convert a binary algorithm to a continuous algorithm and vice versa, this conversion is hard to tune and it is believed that the search algorithm cannot be fully explored to find the optimal goal.

Different algorithms, such as Simulated Annealing (KIRKPATRICK et al., 1983), accept both cases. However, they do not have a defined search engine, becoming necessary to create a function to create new solutions. This function adds another difficult step as it needs to generate new configurations considering the diversification and intensification in the search space.

The problem when using binary codification for sparse linear array design is the absence of control in the number of selected elements. In this way, the sparse array might have a different number of elements for each run of the algorithm, which depending on the application might be undesirable. This can be overcome by using a penalization function, which punishes the FF values of sparse array configurations that exceeded the number of desired elements. These functions need to be tuned to work properly. If the penalization is sharp, the search mechanism will not converge to a result with a sparse array with the desired number of elements. The same behaviour occurs if the penalization is smooth. This creates a challenge to tune the penalisation properly to select the number of elements in the sparse array.

As far as it could be seen in sparse linear array design, only binary codification has been used. The closest to use continuous search algorithm was done by Zhang et al. (2020). The authors used an S-Shape transfer function that converts continuous values into binary to adapt the PSO algorithm and create a binary Particle Swarm Algorithm (bPSO). Even though the authors claim that better configurations were found, the number of elements in the sparse array is not limited without a penalization function. In such a manner, a codification for sparse linear arrays can be created where it has control over the number of array elements without using any penalization function and can be used in continuous optimization algorithms.

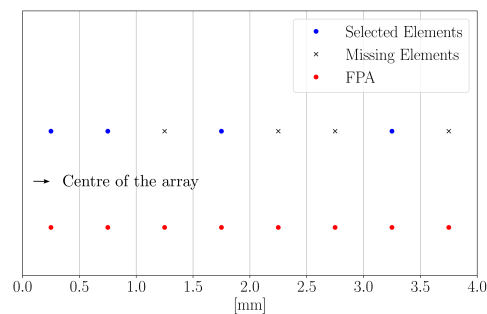
### 3.1.1 Countinous codification

The continuous codification developed in this work has in a vector (solution) the information of the element's position, instead of each element on the grid being on or off. Figure 25 illustrates half of an FPA and a sparse array. The array centred is at zero and, to form a complete symmetric array, the results need to be mirrored. If the sparse array was encoded using binary codification, the vector would have eight positions with the sequence [1, 1, 0, 1, 0, 0, 1, 0], where the ones represent the four elements selected. In the proposed codification, the vector has only four positions with the elements' positions ([0.25, 0.75, 1.75, 3.25]).

This new codification limits the number of elements in the sparse array. In the example given, the binary representation has a size vector of eight, and the number of elements in the array can vary from zero to eight. In the continuous codification, this size is four, and the sparse array will always have this number of elements. This number is defined at the beginning of the search and is immutable during the optimization process.

An aspect of the optimization defined in this work is that only half of the array will be optimized, and the array will be symmetric, as illustrated Figure 25. In this way, it is possible to assure that the energy coming from one part of the array will be equal to the energy coming from the other part and it will avoid irregular shapes in the reflectors. Moreover, this strategy reduces the number of possibilities of sparse arrays which enhances the convergence as it has fewer possible arrays to be tested.

Figure 25 – Eight elements FPA (red dot), where four elements were selected (blue dot) to create a sparse array.



Source: Author

One more parameter that needs to be defined at the beginning of each search is called search space. The elements need a maximum and minimum distance where the elements will be placed. For example, with a 96 FPA and 128 FPA, the size of the array is  $47.5\lambda$  and  $63.5\lambda$ , respectively. Considering that only half of the array is optimized, the search space for these two cases would be from  $0.25\lambda$  to  $23.75\lambda$  or  $31.75\lambda$ . This means that the elements cannot be placed outside this interval, and a solution outside this search distance is considered unfeasible. At last, to match the elements' position in a  $0.5\lambda$  grid, the values on the solution are rounded to the nearest grid point.

### 3.1.2 Comparing algorithms with radiation pattern fitness function

To test if this new coding strategy will help to find better sparse array configurations, different algorithms using both binary and continuous codifications are used and the results are compared. For the binary representation, the algorithms selected to find sparse arrays were Genetic Algorithm (HOLLAND, 1992) and Simulated Annealing (KIRKPATRICK et al., 1983). For the continuous representation, the algorithms selected were Harmony Search (ZONG et al., 2001), Bat Optimization Algorithm (YANG, 2010), Whale Optimization Algorithm (MIR-

JALILI; LEWIS, 2016), Arithmetic Optimization Algorithm (ABUALIGAH et al., 2021) and Particle Swarm algorithm (KENNEDY; EBERHART, 1995). The fitness function used in this problem is the RP FF given in (30).

Two search spaces were set for this problem to test the fitness functions in different settings as they might happen to work in one configuration and fail in another. The first search space corresponds to a 96 FPA, and the second is a 128 FPA search space. For the algorithms where the binary configuration was used, the vector will have 48 and 64 positions with zeros and ones, respectively. For the continuous codification, the array elements can be placed from  $0.25\lambda$  to  $23.75\lambda$  (96 FPA) or  $31.75\lambda$  (128FPA), respectively. Then, the positions of the elements are round to a  $0.5\lambda$  grid that corresponds to the 96 or 128 FPA.

The genetic algorithm, which was initially designed to work with binary vectors, is one of the algorithms that need a penalization function to control the number of elements in the sparse array. As this is not the aim of this work, the algorithm was used to set the number of elements in the sparse array by running it three times for each search space and taking the number of elements in the sparse array as a parameter for the other algorithms.

For the 96 FPA search space, the first sparse array found using the genetic algorithm had 66 elements with a FF of -15.75. The second result had 72 elements with a FF of -15.59, and the third result the sparse array had 80 elements with a FF of -16.25. For the 128 FPA search space, the first result found was a sparse array with 88 elements with a FF of -16.16. The second result was a sparse array with 96 elements with a FF of -17.88 and, the last was a sparse array with 102 elements with a FF of -17.52.

These number of elements of the sparse arrays found by the genetic algorithm were used as a reference for the other algorithms as in the others it is possible to set the number of elements desired for the sparse array. Moreover, two more numbers were arbitrarily selected for the 96 FPA search space (48 and 88), and three for the 128 FPA search space (48, 64 and 110).

Tables 2 and 3 give the FF of the best sparse configurations found using the Arithmetic Optimization Algorithm (AOA), Harmony Search (HS), Particle Swarm Optimization (PSO), Simulated Annealing (SA) and Whale Optimization Algorithm (WOA) where each algorithm ran three times finding three different sparse linear arrays. For each column, it is possible to see the number of elements that the sparse arrays have and the results in bold indicate the best result among them. The bat optimization algorithm was also tested, but it had a convergence issue. This might happened because of the parameters used in the algorithm or its inefficient to solve this problem. Either way, the results found using this algorithm were discarded.

The Simulated Annealing Algorithm differs from the others algorithm in the Tables as it uses binary codification. The algorithm differs from the others as it requires that the user creates a neighbourhood structure, which is a function that finds new solutions for the optimization

problem. The strategy created randomly swaps an active element in the binary vector to an inactive one. In this way, the number of elements in the sparse array keeps the same, and it is possible to control the number of elements in the sparse array, which is not possible using the genetic algorithm strategy.

Table 2 – Comparison between search algorithms using the radiation pattern based fitness function given in (30). Search space corresponding to a 96 elements FPA

Elements	48	66	72	80	88
GA (binary)	–	-15.75	-15.59	-16.25	–
AOA Run 1	-12.09	-17.06	-16.56	-17.53	-15.09
AOA Run 2	-11.67	-16.41	-16.96	-17.55	-15.09
AOA Run 3	-13.16	-16.48	<b>-18.21</b>	-18.07	-15.10
HS Run 1	-14.34	-15.95	-15.95	-17.22	-15.11
HS Run 2	-13.62	-16.26	-16.26	-17.03	-14.96
HS Run 3	-12.96	-16.18	-16.18	-16.75	-15.11
PSO Run 1	-13.57	-16.00	-16.00	<b>-18.29</b>	-15.11
PSO Run 2	-12.31	-15.12	-15.12	-17.80	-15.11
PSO Run 3	-11.62	-15.22	-15.22	-17.52	-15.11
SA Run 1 (binary)	-12.11	-15.21	-15.21	-15.04	<b>-17.98</b>
SA Run 2 (binary)	-12.39	-13.32	-13.32	-15.11	-16.10
SA Run 3 (binary)	-11.30	-14.91	-14.91	-14.01	-14.94
WOA Run1	-14.76	<b>-17.51</b>	-17.51	-17.65	-15.11
WOA Run2	-14.08	-16.75	-16.75	-18.01	-15.11
WOA Run3	<b>-16.58</b>	-17.23	-17.23	-17.66	-15.11

As it is possible to see in Table 2, most of the best results were found by the algorithms that work with the continuous domain, except the SA Run1, where -17.98 is the best result and used the binary domain. The FF of the configurations found by these algorithms were also better than the FF of the best sparse arrays found in the Genetic Algorithm.

From Table 3, it is possible to see that the WOA found the best results for all settings of sparse arrays and also these results were better than the ones found by the Genetic Algorithm. This leads to an indication that the continuous codification together with algorithms designed for its use can find sparse configurations with better FF than using binary codification.

One motivation of this part of the study is that most of the works that use the RP FF do not show the sparse configuration, only the RP FF of the array found. When the array configuration is given, the settings defined by the authors consider an FPA smaller than the desired in this work. This makes it hard the comparison of different sparse arrays as the configurations are unknown. After implementing the continuous search, it was noted that the results found had lower FF values than in the works that use discrete search (YANG et al., 2006; HU et al., 2017; HU et al., 2018; ZHANG et al., 2020). For example, Zhang et al. (2020) find a 88/128 sparse array where configuration FF is -18.33. In this work, the best 88/128 has a FF of -18.71. In the same work, the 71/96 configuration has a FF of -17.81 and, in this work, the best 72/96

Table 3 – Comparison between search algorithms using the radiation pattern based fitness function given in (30). Search space corresponding to a 128 elements FPA

Elements	48	64	88	96	102	110
GA (binary)	–	–	-16.16	-17.88	-17.52	–
AOA Run 1	-11.56	-14.53	-15.27	-18.42	-18.77	-17.61
AOA Run 2	-11.13	-13.44	-16.17	-18.64	-17.45	-17.79
AOA Run 3	-10.87	-14.29	-18.30	-17.48	-19.03	-17.51
HS Run 1	-12.30	-13.41	-17.21	-18.89	-18.53	-17.35
HS Run 2	-11.13	-13.02	-17.69	-17.84	-18.12	-17.26
HS Run 3	-11.04	-13.45	-18.47	-18.10	-18.17	-17.50
PSO Run 1	-11.52	-12.98	-16.09	-18.74	-19.18	-17.82
PSO Run 2	-10.69	-13.15	-16.57	-15.50	-17.95	-17.91
PSO Run 3	-11.08	-13.56	-17.88	-18.75	-19.14	-17.45
SA Run 1 (binary)	-13.18	-12.83	-15.67	-15.20	-15.73	-16.49
SA Run 2 (binary)	-12.15	-13.54	-13.53	-15.19	-15.30	-17.56
SA Run 3 (binary)	-12.70	-13.90	-13.04	-16.02	-14.41	-15.95
WOA Run1	-14.82	<b>-16.62</b>	-18.02	-19.12	<b>-19.50</b>	<b>-18.08</b>
WOA Run2	-14.33	-15.99	<b>-18.71</b>	<b>-19.37</b>	-19.02	-18.01
WOA Run3	<b>-14.99</b>	-15.85	-18.53	-18.80	-19.20	-17.86

configuration has a -18.21 FF. This codification with the continuous optimization algorithms was able to find configurations with better FF.

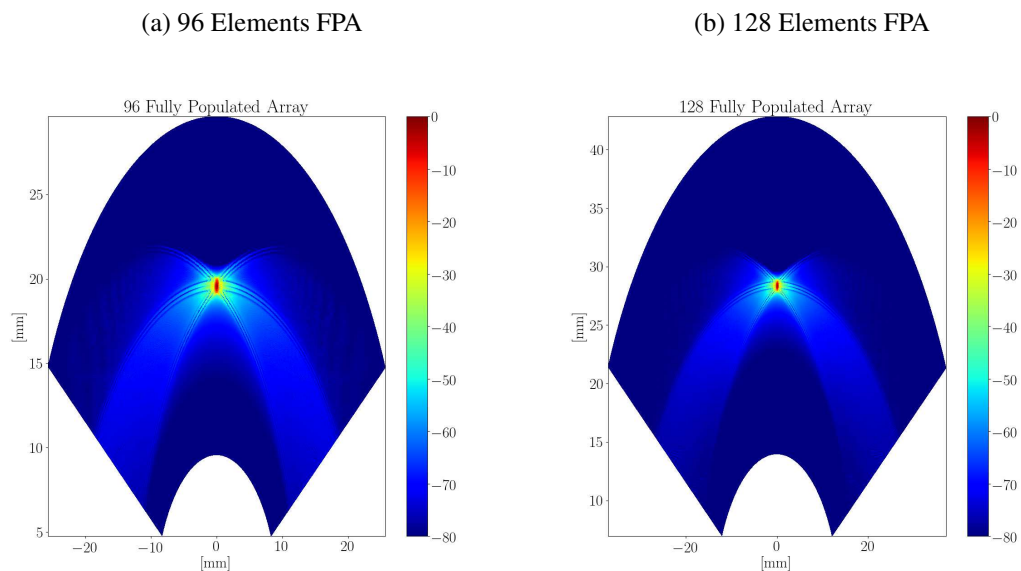
In Figure 26 (a) and (b) the PSFs of a FPA with 96 and 128 elements are illustrated. For all PSFs created in this chapter, the  $f_c = 3.5$  MHz,  $BW = 0.6$  and  $f_s = 35$  MHz. The images were created from  $-60^\circ$  to  $60^\circ$  where the important information about the lateral and grating lobes is concentrated in this area. For real applications, each element of the array has its own radiation pattern that attenuates the energy outside  $[60^\circ]$ . Moreover, the point reflector was positioned at 0 on the x-axis and a distance of z corresponding to the array size. For 96 FPA, it is  $47.5\lambda$  and, for 128 FPA, it is  $63.5\lambda$ . The PSF, in axial size, needs to be wide enough to assure that the lateral and grating lobes will be imaged.

As it can be seen in these PSFs, if the number of elements in the array increases, the lateral resolution improves. Furthermore, if the array is symmetric, the PSF is symmetric and it is only necessary to create half of the image. A difficult task when analysing ultrasonic images is to quantify the images to decide which one is better. One strategy is to plot lines of the PSF so it's possible to see the lateral resolution and sidelobes levels improvement.

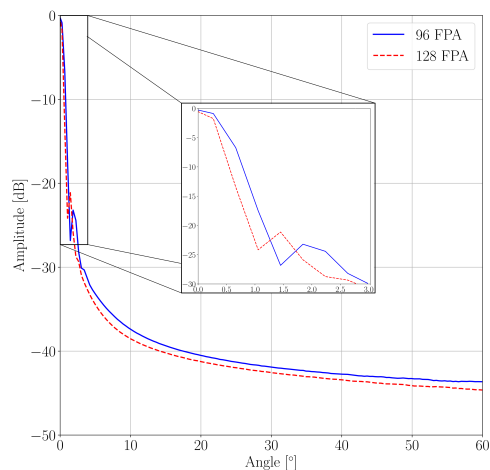
In this way, Figure 26 (c) illustrates the amplitudes created by calculating the mean of the PSFs at each angle and then normalizing it, which will be referred to as normalized means. These lines illustrate only half of the PSF, as the other half is the same. The blue continuous line corresponds to the 96 elements of FPA, and the red dashed line corresponds to the 128 elements of FPA. As can be seen in the zoomed part of the image, the lateral resolution is better for the 128 elements FPA, which is expected. One interesting feature of these signals is seen in  $1.4^\circ$

and  $1.5^\circ$ , where a valley is seen. This valley becomes closer to  $0^\circ$  as the array size increase. Further, it will be used to define the new fitness function created in this work.

Figure 26 – PSF of (a) 96 elements FPA, (b) 128 elements FPA and (c) amplitude are summed and then normalized at each angle of the PSF, where the blue continuous line corresponds to the 96 elements FPA and the red dashed line corresponds to 128 elements FPA.



(c) Amplitudes's Normalized Means



Source: Author

During the study of the optimization algorithms and the codification problem, different sparse array configurations were found. It is expected that the lower the FF value of a sparse array, the better this array is in imaging. To check if this trend happens, the PSFs of different sparse configurations corresponding to the results in Table 2 and 3 were analysed.

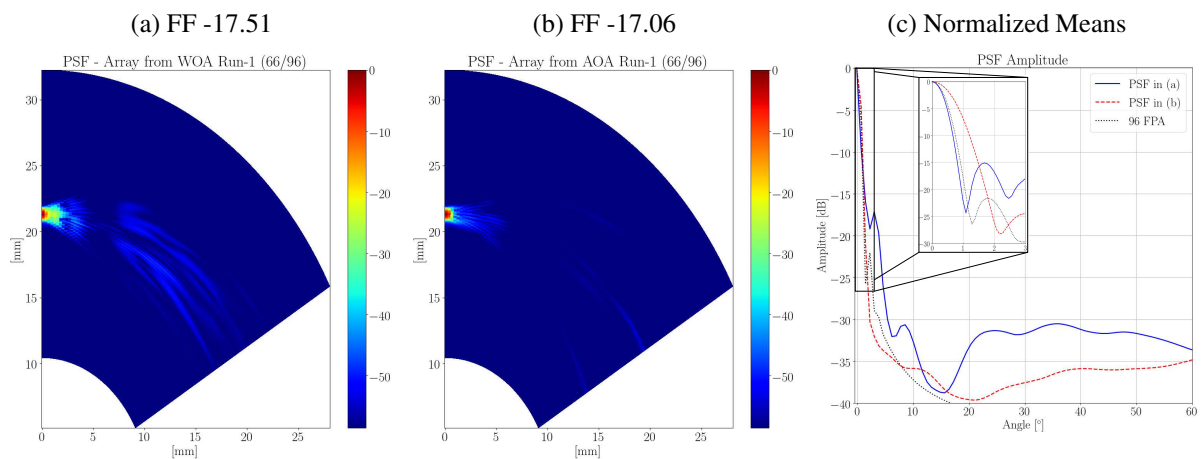
Figure 27 illustrates two PSFs created using 66 elements in a search space correspond-

ing to a 96-element FPA. In (a), the PSF created corresponds to the sparse array related to the best 66 results presented in Table 2 as WOA Run1. In (b), the PSF was created using the sparse configuration referred to AOA Run1.

Comparing the two PSFs, it is possible to see that Figure 27(a) has higher amplitudes close to the point reflector and higher energy in different areas of the image compared to (b). This is clear when the normalized mean of the PSFs are plotted together in Figure 27(c), where the continuous blue line corresponds to the first PSF (WOA Run1 66/96) and the red dashed line corresponds to the second PSF(AOA Run1 66/96). The amplitudes are lower at most of the points in the PSF illustrated in (b). Although there is a slightly better lateral resolution in the PSF illustrated in (a), it does not compensate for the high side lobes energy.

The FFs of these configurations are close to each other. The best configuration (WOA Run1) has a FF of -17.51 and the second configuration (AOA Run1) has a FF of -17.06. However, by comparing the PSFs, the second configuration shows a PSF with a better balance between lateral resolution and artefact intensities, which is desirable for sparse arrays. The FF is failing in distinguish sparse arrays as the ones with higher values have better characteristics.

Figure 27 – PSFs created using the 66 elements sparse array configurations related to Table 2, where (a) is the WOA Run 1 configuration and (b) the AOA Run 1 configuration. In (c), the normalized means of the two PSF are illustrated where the PSF in (a) is illustrated in a blue continuous line and (b) is illustrated in a red dashed line.



Source: Author

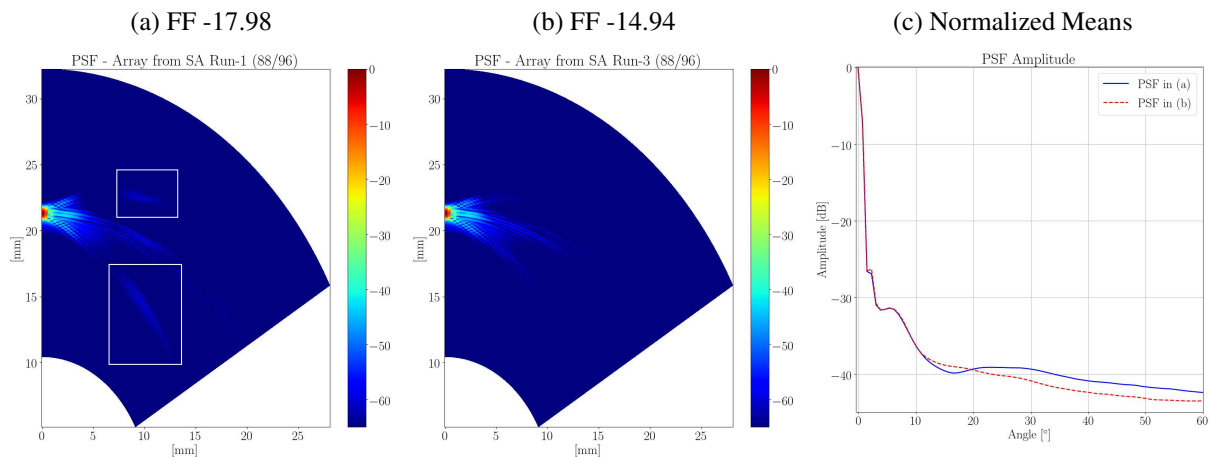
Figure 28 illustrates two PSF of sparse arrays with 88 elements in a search space of a 96 FPA. The first PSF (a) is generated using the best configuration according to Table 2, which is the WOA Run2 configuration with an FF of -17.98. The second PSF (b) is generated using the worst configuration according to Table 2, that is SA Run 3 with a FF of -14.94.

By looking at the PSFs, they almost can be considered the same as the only difference between them is the amplitudes highlighted in the squares in Figure 28 (a). The similarities are clear when the mean normalized is analysed (Figure 28 (c)), where it is possible to see that the

signals are similar to each other.

An interesting point of this comparison is when the FF of these two configurations are analysed. The best configuration has a FF of -17.98 and the worst has a FF of -14.94. However, they produce almost the same PSF, indicating that the sparse configurations have the same potential for imaging. This shows that the FF used in several works (YANG et al., 2006; HU et al., 2017; HU et al., 2018; ZHANG et al., 2020) is inefficient to evaluate the sparse linear array configurations as the configuration with the best FF value does not correspond to the best configuration to image.

Figure 28 – PSFs created using the 88 elements sparse array configurations related to Table 2, where (a) is the SA Run 1 configuration and (b) the SA Run 3 configuration. In (c), the normalized means of the two PSF are illustrated where the PSF in (a) is illustrated in a blue continuous line and in (b) is illustrated in a red dashed line.



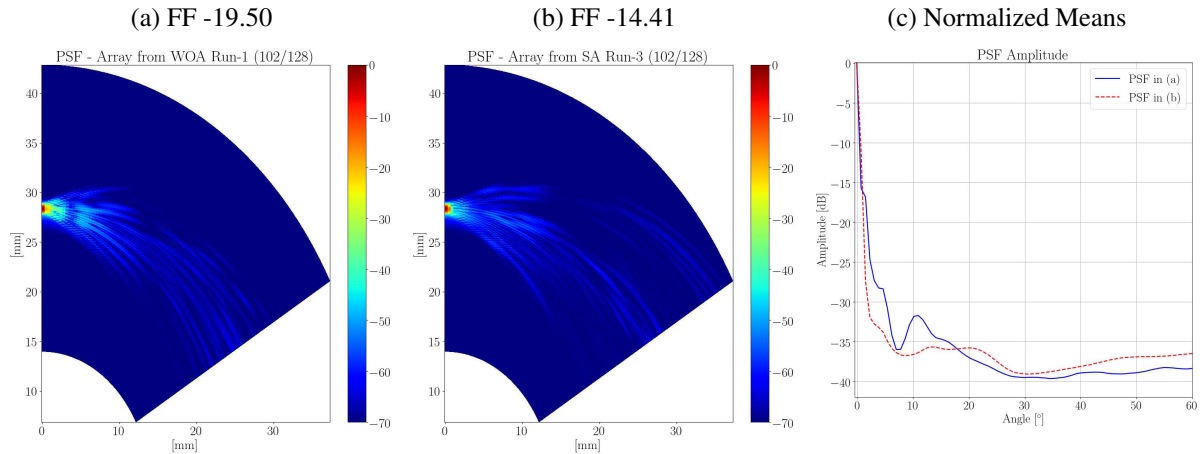
Source: Author

This same trend can be identified in the sparse array configurations found in the search space of 128 elements FPA given in Table 3. Figure 29 illustrates two PSFs where the sparse arrays have 102 elements. The PSF illustrated in (a) is generated with the sparse configuration with the best FF value in Table 3 under 102 elements with a -19.50 value. The second PSF, illustrated in (b), is generated with the sparse array with the worst FF among the 102 elements with -14.41. Analysing the two PSFs it is possible to see that in (a) the PSF has higher energy aside the point reflector than the PSF in (b).

The normalized mean of the PSF is illustrated in (c), where the blue continuous line corresponds to the PSF in (a) and the red dashed line the PSF in (b). It is possible to verify that the red dashed signal has a lower amplitude close to zero degrees, which translates to lower energy close to reflectors during the imaging process giving better resolution and contrast.

The PSF's analysis of the sparse arrays found indicates that this RP FF gave in (30) is an unsatisfactory fitness function to evaluate sparse arrays configurations. The two features extracted from the radiation pattern narrowband response are insufficient to summarize all the

Figure 29 – PSFs created using the 102 elements sparse array configurations related to Table 3, where (a) is the WOA Run 1 configuration and (b) the SA Run 3 configuration. In (c), the normalized mean of the two PSF are illustrated where the PSF in (a) is illustrated in a blue continuous line and (b) is illustrated in a red dashed line.



Source: Author

information about it.

Different features of the radiation pattern can be extracted to create a new FF that can evaluate the sparse array configuration and distinguish better the sparse configurations that can generate images with good lateral resolution and contrast. However, it could be interesting to use as a modelling tool a method close to how the ultrasonic images are generated. In this way, the PSF has this ability and the challenge is to extract features of the PSF that will quantify all the information about it to distinguish the configurations.

### 3.2 NEW FITNESS FUNCTION

The PSF simulates how a point reflector is imaged using an array. It is a better approximation to real applications than the radiation pattern narrowband response. Therefore, it is going to be used to create a FF that will quantify the sparse array ability in imaging. The aim of this chapter is to create a FF that is able to distinguish the sparse configurations in a way that a low value represents a good array and a high value a bad array. As it could be seen, the previous FF based on the radiation pattern fails in this distinction.

The PSF, as far as it could be seen in the literature, has not been used yet for this purpose because it is considered time-consuming compared to the time to generate the radiation pattern. However, as the processing power has increased over time, the PSF is now available for this task.

During the analysis of the sparse arrays found using the RP FF, different PSFs were analysed. Two characteristics were evaluated: The size of the point reflector and the amplitudes

around it. The point reflector needs to be the smaller possible as it translates to better lateral resolution in the images. On the other hand, the amplitudes outside the point need to be the smaller possible so the images generated by this array would have good contrast. In this way, it would be a reasonable strategy to create a FF that evaluates these two parameters.

The FF is created by extracting two features from the PSF, the energy ( $E$ ) of part of the PSF, which corresponds to the amplitudes outside the point reflector, and the Shannon entropy ( $H$ ) (SHANNON, 1948). Although the entropy is used in information theory as message uncertainty during transmission, in this work, the entropy is used in machine learning background (GERON, 2019) where it will evaluate the similarity between PSFs. Therefore, the PSF of a sparse array will be compared to the PSF of an FPA considered as a PSF reference. Thus, both the amplitudes and the point reflector size will be evaluated. The new FF will be created by combining these two features. The logic of creating this FF is that it will be able to evaluate both the point reflector size and the amplitudes around it.

Figure 30 (a) illustrates where the point reflector in the PSF will be positioned, which is in  $x = 0$  and  $z = D$ .  $D$  is the maximum size that the sparse array will have, which is defined at the beginning of the search. For example, with 48 elements it is possible to create a sparse array with an equivalent size of 64, 96 or 128 FPA. For this reason, it is necessary to define this maximum size before starting the optimization process. The PSF size created needs to have an axial size wider enough to contain all the side and grating lobes interferences. To compensate for the time cost caused by the axial size, the PSF will be created from 0 to  $60^\circ$  and, as the sparse array will be symmetric in its centre, only half of the PSF is required.

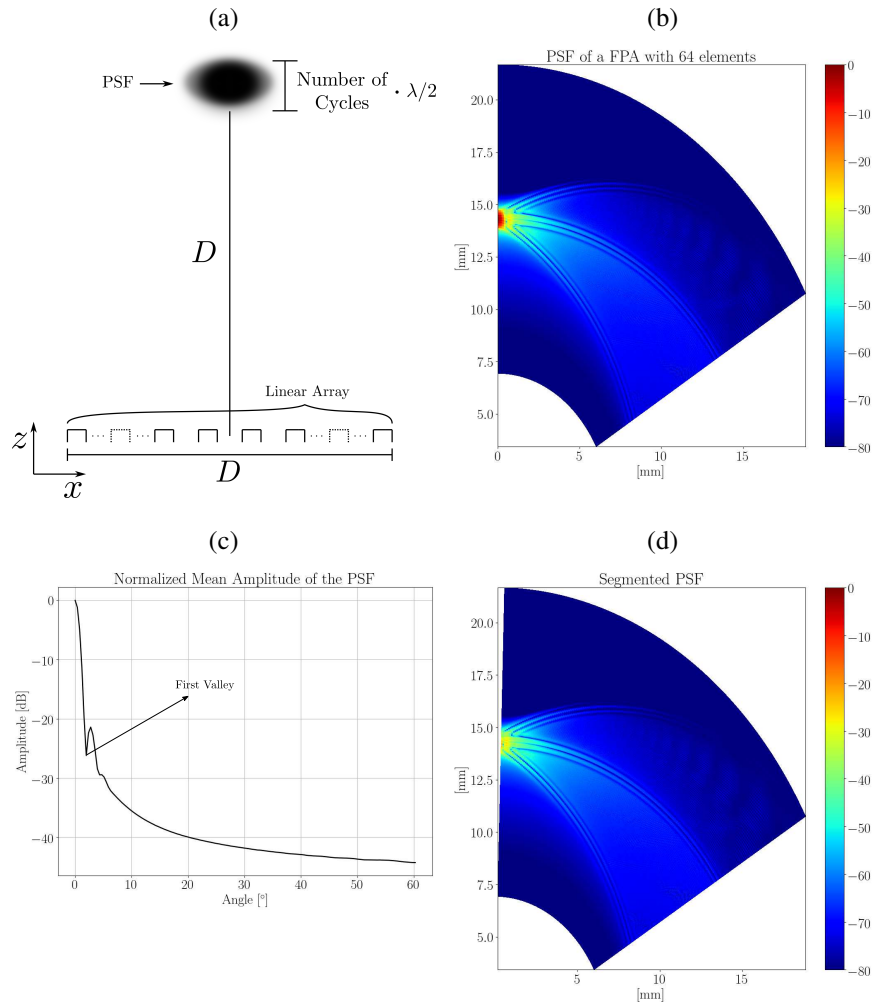
The energy is the sum of the amplitudes squared. However, the energy is not calculated for all PSF as the focus is the energy around the point reflector. Figure 30 (b) illustrates a PSF calculated using a 64 element FPA. To determine which amplitudes will be used to calculate the energy, the normalized mean of the PSF is calculated and presented in Figure 30 (c). As it can be seen, a recurrent valley appears and changes its position as the array size changes. This valley was mentioned when the PSFs of 96 and 128 FPA were presented. Using this information, the energy will be calculated using all amplitudes after this valley.

Figure 30 (d) illustrates the amplitudes used to calculate the energy, which is the amplitudes after the first valley in the PSF reference (c). It is possible to see that the point reflector is removed, remaining only the undesired amplitudes. The logic in this feature is that the optimization algorithm will find sparse array configurations with lower energy that will, in consequence, reduce the contrast loss when sparse arrays are used.

The second feature uses the Shannon entropy equation defined as:

$$H = - \sum_{i=1}^{N_{pix}} \rho_i \log_{N_{pix}}(\rho_i), \quad (31)$$

Figure 30 – (a) Distance where the defect is placed based on the array size ( $D$ ). (b) PSF of a FPA with 64 elements is used as an example. (c) normalized mean extracted from the PSF showing the first valley and (d), the segmented PSF used to calculate the Energy.



Source: Author

where  $\rho_i$  is a value of the distribution  $\rho$  calculated as:

$$\rho = PSF - PSF_{ref} + \frac{1}{N_{pix}}, \quad (32)$$

which is the PSF generated by the sparse array currently analysed minus a PSF reference, that is a PSF of an FPA with the dimension  $D$  set at the beginning of the search (Figure 30 (b) for example), and added to an amplitude  $1/N_{pix}$ , where  $N_{pix}$  is the number of pixels in the PSF image.

This equation works as a similarity evaluator between two PSFs, where one is generated by the sparse array and the other by a PSF considered the best, which is based on an FPA with size  $D$  defined at the beginning of each search. If in a perfect case where the two PSFs are the same, the difference in amplitudes is equal to zero. However, the constant  $1/N_{pix}$  is summed resulting in a uniform distribution and a max entropy of 1.

The new fitness function proposed in this work combines these two features. As the optimization algorithms work to find new arrays that minimize the FF value, the new FF is created by taking the energy of the segmented PSF and dividing it by the entropy (Equation (33)). In this way, the optimization algorithm will try to find a sparse array configuration that produces low energy in the undesired area and has high entropy, which corresponds to a more similar PSF compared to the PSF reference.

$$FF = E/H, \quad (33)$$

Table 4 – Comparison between search algorithms using the radiation pattern based fitness function given in (33). Search space corresponding to a 96 and 128 elements FPA

Setting Elements	96					128					
	48	66	72	80	88	48	64	88	96	102	110
AOA Run 1	1.98	1.34	1.18	1.03	0.93	12.75	6.12	1.70	1.34	1.54	1.01
AOA Run 2	2.05	1.30	1.19	1.02	0.92	12.17	4.02	1.92	1.22	1.54	0.90
AOA Run 3	1.98	1.28	1.21	1.02	0.91	12.61	6.30	1.72	1.57	1.24	1.11
HS Run 1	2.95	1.54	1.17	1.04	0.93	13.28	4.77	1.68	1.15	1.00	0.85
HS Run 2	2.76	1.52	1.26	1.02	1.01	12.58	5.09	1.75	1.18	1.02	0.86
HS Run 3	3.23	1.41	1.19	1.09	0.98	12.07	5.73	1.55	1.21	1.00	0.84
PSO Run 1	1.97	1.36	1.15	1.00	0.90	11.12	4.48	1.51	1.13	0.98	0.83
PSO Run 2	7.81	1.28	1.17	1.01	0.91	15.37	4.09	1.74	1.17	0.97	0.84
PSO Run 3	2.05	1.31	1.17	1.08	0.92	10.61	4.22	1.57	1.17	0.97	0.83
SA Run 1 (binary)	2.81	1.32	1.19	1.07	0.93	14.27	4.91	1.56	1.18	1.03	0.86
SA Run 2 (binary)	2.14	1.32	1.33	1.05	0.92	20.42	4.00	1.46	1.13	1.04	0.90
SA Run 3 (binary)	1.99	1.31	1.13	1.05	0.93	20.91	4.98	1.48	1.17	0.95	0.84
WOA Run 1	<b>1.37</b>	1.49	<b>0.96</b>	0.90	0.84	9.72	3.37	<b>1.27</b>	0.96	<b>0.81</b>	0.72
WOA Run 2	2.11	<b>1.00</b>	0.94	<b>0.87</b>	<b>0.83</b>	<b>7.84</b>	<b>3.31</b>	1.29	0.96	0.82	0.71
WOA Run 3	7.32	1.07	1.00	0.89	0.85	7.96	3.62	1.28	<b>0.95</b>	0.84	<b>0.70</b>

The search algorithms used with the fitness function based on the radiation pattern were also used with this new fitness function to evaluate how the algorithm behaves. Only the simulated annealing has the binary codification and the genetic algorithm was not used as it is necessary to have a penalty function to control the number of elements. The settings with search space and the number of array elements remained the same and the FF values of the sparse arrays found were illustrated in Table 4.

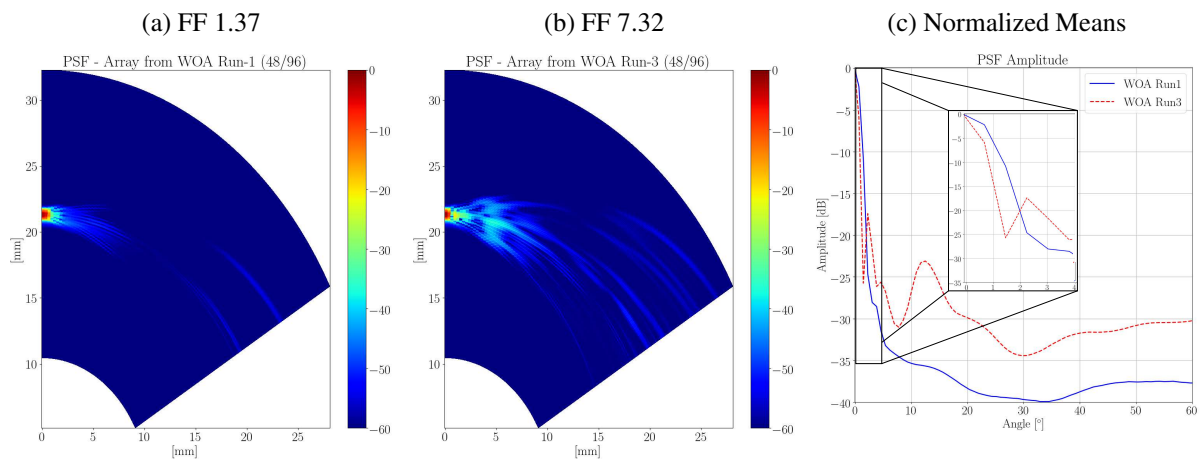
One interesting point about the results is that the WOA algorithm was able to find the configurations with the lowest FF value as highlighted in bold. This concentration of best results indicates that the WOA is the best search algorithm among the tested algorithms.

Different sparse arrays with their respective FF given in Table 4 were used to generate their respective PSF to analyse how well the FF was able to distinguish the sparse arrays configurations in imaging. In the first case, the best array configuration with 48 elements in a search

space of 96 elements (WOA Run 1) was used to create the PSF illustrated in Figure 31 (a). To compare with this PSF, the sparse array found using the WOA in run 3 with FF of 7.32 was illustrated in Figure 31 (b). As it is possible to see in the PSFs, the energy outside the point reflector is much higher in (b) and this configuration would probably generate worse images.

This difference is clear when the normalized means, illustrated in Figure 31 (c), are analysed. In the blue continuous line, the PSF of the WOA Run 1 (the best) has a worse lateral resolution, but an energy 15 dB lower compared with the PSF of the WOA Run 3, illustrated in the red dashed line. There is a substantial difference between the FFs as the WOA Run 1 configuration has a 1.37 value and the WOA Run3 configuration has a 7.32 value.

Figure 31 – PSFs created using the 48 elements sparse arrays in a search space of 96 FPA, where the FF of each configuration is illustrated in Table 4. (a) is the WOA Run 1 configuration and (b) the WOA Run 3 configuration. In (c), the normalized means of the two PSF are illustrated where the PSF in (a) is illustrated in a blue continuous line and (b) is illustrated in a red dashed line.



Source: Author

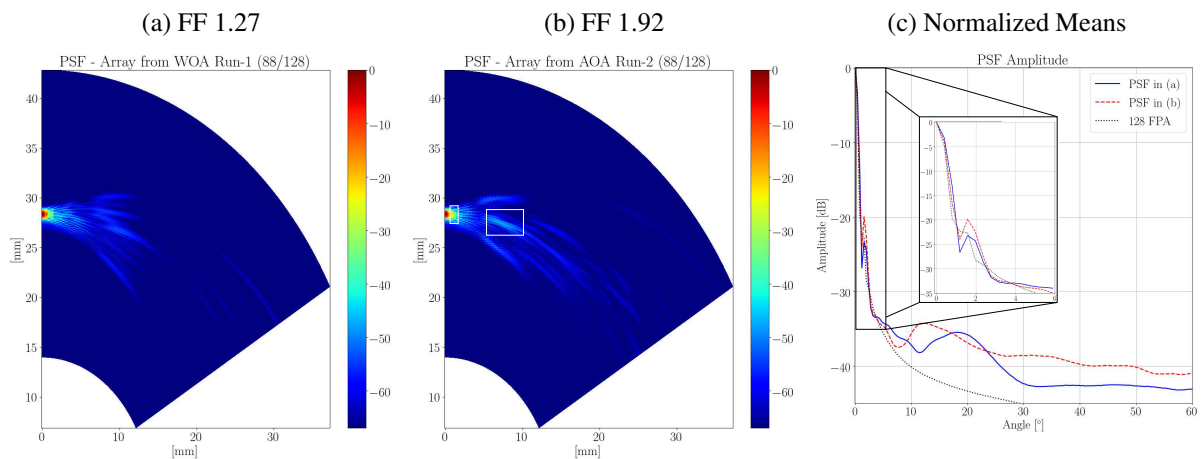
This example was used to illustrate that the configurations with higher FF generate PSF with undesired features, like wider lateral resolution and higher side lobes. The configuration related to the PSO Run 2 with a 7.81 FF value also has a PSF with high energy outside the point reflector. These results are outliers as they are much higher than the other FF. Sometimes these outliers can occur in optimization problems as the algorithm is not able to converge to a good result. In this way, one strategy is to run the algorithm a number of time and consider the configuration with the lowest FF.

In this second example, the configurations selected have a small FF difference. Both configurations are a sparse array with 88 elements in a search space of 128 elements where the first is the WOA Run 1 with a FF of 1.27, which is the smallest value found among the other results, and the second is the AOA Run 2 with a FF of 1.92. Their PSF are illustrated in Figure 32 (a) and (b), respectively. The differences between the PSFs are visually smaller in this case. However, it is possible to see a higher amplitude in (b) highlighted in the image.

The normalized mean is illustrated in Figure 32 (c) where the PSF of WOA Run 1 configuration is illustrated in a blue continuous line, the PSF of AOA Run 2 is illustrated in a red dashed line and the PSF of a 128 FPA is illustrated in black dotted line. Close to the point reflector, the amplitudes are similar to each other with a small difference in  $2^\circ$  where the red dashed is 3 dB higher. For most of the larger angles, the PSF of AOA Run 2 configuration has higher values, corroborating the higher FF value.

Although the PSF are alike, the PSF in (b) has higher amplitudes outside the point reflector which might translate to a worse contrast in ultrasonic images compared to the PSF in (a). In this way, the proposed FF was able to quantify this visual difference and indicate which is a better sparse linear array configuration.

Figure 32 – PSFs created using the 88 elements sparse arrays in a search space of 128 FPA, where the FF of each configuration is illustrated in Table 4. (a) is the WOA Run 1 configuration and (b) the AOA Run 2 configuration. In (c), the normalized means of the two PSF are illustrated where the PSF in (a) is illustrated in a blue continuous line and (b) is illustrated in a red dashed line.



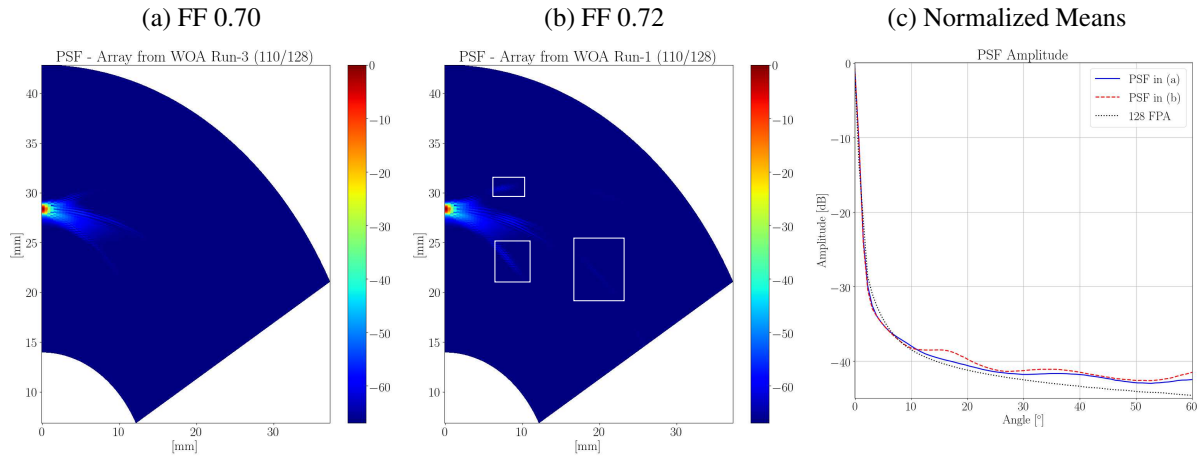
Source: Author

This ability for this fitness function to distinguish the sparse configurations is even better highlighted when the PSFs of two sparse array configurations with 110 elements are compared. The first configuration is the best one found WOA Run 3 with a FF value of 0.70 and the second configuration is the WOA Run 1, which has a slightly higher FF value of 0.72. The PSF of these configurations are illustrated in Figure 33 (a) and (b), respectively. As it can be seen, their PSFs are almost identical with a minor intensity increase highlighted with the white rectangles in (b).

The normalized means amplitude are given in Figure 33 (c). It is possible to see where these higher amplitudes summed as the PSF generated with the WOA Run 1 configuration, illustrated with a dashed red line, have higher intensity between  $15$  to  $38^\circ$ .

In this last example, two results with almost identical FF values were compared to check if this small value difference would be able to distinguish the sparse array configurations. The

Figure 33 – PSFs created using the 110 elements sparse arrays in a search space of 128 FPA, where the FF of each configuration is illustrated in Table 4. (a) is the WOA Run 3 configuration and (b) the WOA Run 3 configuration. In (c), the normalized means of the two PSF are illustrated where the PSF in (a) is illustrated in a blue continuous line, in (b) is illustrated in a red dashed line and the.



Source: Author

configuration with higher FF also had higher PSF amplitudes meaning that this configuration would generate a slightly worse ultrasonic image compared to the other sparse array configuration with lower FF.

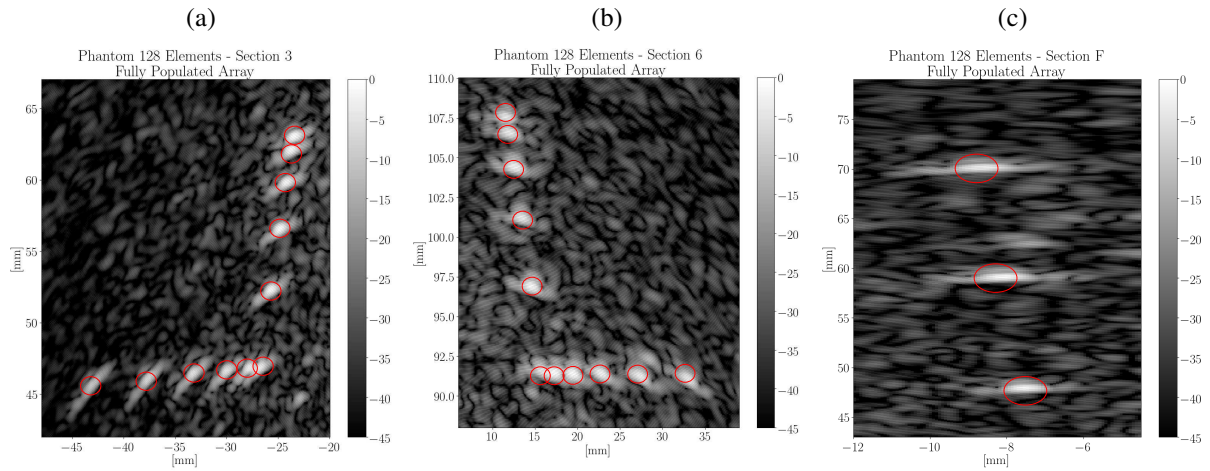
In the state of art FF based on the radiation pattern (30), there were cases where configurations that generated PSF with low artefact intensity and high resolution were considered a worse configuration compared to sparse arrays that generate worse PSF but have a lower FF. This means that the RP FF misses apertures that generate images with good qualities and cannot distinguish between good and bad sparse array configurations.

In this new FF, when the difference in the FF between two configurations is high, it is evident that the PSF generated with the configuration with lower FF will be better with lower energy outside the point reflector. If this difference is reduced, the distinctions start to be hard to see, as illustrated in example 2. However, the FF can distinguish which configuration generates better PSF. At last, two configurations with almost the same FF were analysed. The PSFs were very similar, but the one generated by the configuration with lower FF has better features, as highlighted.

The new FF follows the logic, as the lower its value in a configuration, the better this sparse array is to image, which is a behaviour not seen in the RP FF. To validate this new FF and compare the configurations found using it with configurations found using the RP FF, phantom images were generated and analysed.



Figure 35 – Ultrasonic images of (a) Section 3, (b) Section 6 and (c) Section F of the Dansk Phantom Model 525.



Source: Author

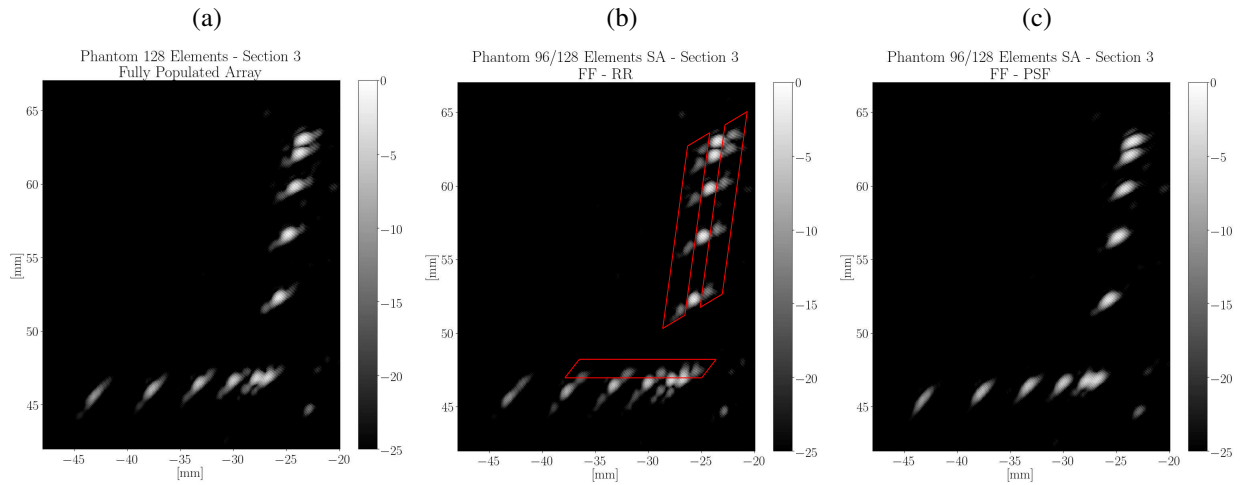
One laborious task is to evaluate the ultrasonic images, as it is a subjective task. It is hard to quantify information about lateral resolution and artefact intensity in the way that all aspects of the image are considered. For example, the mean squared error between one ultrasonic image generated using a sparse array and the image generated using an FPA can have a high error, but it does not mean that the image is bad.

The problem of using the Mean Squared Error can be illustrated in Figure 36, where section 3 of the phantom is generated using 3 configurations: (a) the 128 FPA, (b) a 96 Sparse Array found using the RP FF and (c) a 96 sparse array found using the proposed fitness function. These two sparse configurations are the best found in Table 3 and Table 4, respectively. The dynamic range was purposely set to -25 dB to highlight the wires and the energy aside them. In (a), there is high energy aside the wires related to the side lobes of the FPA. This is more evident in (b), where there is an improvement in the lateral solution, but the high side lobes create an artefact with high intensity aside the reflectors, as highlighted in the image. In (c), there is a loss in lateral resolution compared with (a) and (b), but this energy besides the reflector does not appear.

As it can be seen, there are different aspects of the image that need to be analysed to determine the image quality. If only the error between the image generated by the FPA and the sparse array would be used to characterize the images, the image in (b) that has a lower error, would be considered better than the image in (c).

Wang et al. (2004) presented one figure of merit called Mean Structural Similarity Image Measurement (*MSSIM*), which evaluates one image with a reference based on three components: luminance, contrast and structure. Rangaraju et al. (2012) used this figure of merit in ultrasonic images to conclude that this measurement is more consistent than the mean squared error.

Figure 36 – Phantom Section 3 Image using: (a) 128 Elements FPA, (b) best 96-configuration found using the Radiation Pattern FF and (c) best 96-configuration found using the FF proposed in this work.



Source: Author

The MSSIM of two images,  $I_1$  and  $I_2$ , is calculated as:

$$MSSIM(I_1, I_2) = \frac{1}{M} \sum_{i=1}^M SSMI(I_1, I_2), \quad (34)$$

where the images are segmented into squared blocks of 25 pixels, which corresponds to the wire size. Then, the SSMI for each block is calculated as:

$$SSMI(x, y) = \frac{(2\mu_x\mu_y)(2\sigma_{xy})}{(\mu_x^2 + \mu_y^2)(\sigma_x^2 + \sigma_y^2)}, \quad (35)$$

which  $x$  and  $y$  correspond to the amplitudes of the segmented image  $I_1$  and  $I_2$ , respectively.  $\mu$  the mean and  $\sigma$  the standard deviation.

$\sigma_{xy}$  is a value calculated as:

$$\sigma_{xy} = \frac{1}{M-1} \sum_{i=1}^M (x_i - \mu_x)(y_i - \mu_y). \quad (36)$$

$MSSIM$  has a range of 0 to 1, where the higher the value, the greater the similarity.

This figure of merit will be used to compare and measure the similarity between the ultrasonic image generated by a sparse array and an ultrasonic image generated by an FPA, which is considered the best array. In this way, it is possible to check which sparse array configuration will generate images more similar to a reference.

In addition, the contrast to noise ratio (CNR) is also used as a figure of merit, which is defined as (PATTERSON; FOSTER, 1983):

$$CNR(I_{in}, I_{out}) = \frac{|\mu_{I_{in}} - \mu_{I_{out}}|}{(\sigma_{I_{in}} + \sigma_{I_{out}})^{1/2}}, \quad (37)$$

in this way, the best sparse array configuration indicated in Tables 2, 3 and 4 found using the FF based on radiation pattern and the proposed FF based on the PSF's analysis was used to generate the phantom image of section 3, 6 and F. Then, the CNR and the MSSIM, defined in (36), were used to evaluate the generated phantom images.

The MSSIM needs a reference image and two strategies were adopted to define this reference image. First, the reference image is generated based on the search space defined at the beginning of each search. For example, the first five array configurations correspond to a search space of 96 FPA. Therefore, the reference image for these configurations is a phantom image of sections 3,6, and F that was created using a 96 FPA. For the last six configurations, the search space corresponds to a 128 FPA, so the reference image is generated using a 128 FPA.

The second strategy considers the actual size of the sparse array to create an ultrasonic image with an equivalent FPA. For example, the first setting considers positioning 48 elements in a space where 96 elements fit. Although it is possible to use all the space, the best result found using the proposed FF places the furthest element at an equivalent FPA with 54 elements. In this way, the FPA used to create a reference image is the 54 FPA. Table 5 summarizes all the results where the top half of the table the 96 and 128 FPA are considered as a reference (Strategy 1) and the bottom half of the table considered the size of the sparse array to create the reference image (Strategy 2), where higher values that have more than 0.5 difference are highlighted.

The reason to choose these two strategies is to focus on different aspects of the images generated by the sparse arrays. Strategy 1 focuses on images' lateral resolution, as the reference is the 96 and 128 FPA. The focus of strategy 2 is on the artefacts' intensities and how similar they are to the variable reference image. It is desired that the sparse array generates images with a higher lateral resolution, but the artefact intensities need to remain low. Therefore, the FF needs to consider a satisfactory sparse array that generates images that has the balance of these two characteristics.

In Strategy 1, under the 96 FPA reference section, the values are low for the 48 and 66 elements sparse array for both arrays found using different FF. The arrays found using the RP FF have higher lengths than the lengths of the arrays found using the proposed FF. In the case of a low number of elements in a wide search space, the images generated by the arrays found using the RP FF have high artefact intensities that collaborate with this reduction in the MSSIM result. In contrast, the arrays found using the proposed FF are less sparse, which means that the lateral resolution is decreased and collaborates with the lower MSSIM. However, the images generated by these arrays have a better balance between lateral resolution and contrast, as will be seen when the results in strategy 2 are analysed. As the number of elements increases in the sparse array, the MSSIM also increases, and similar MSSIM results are obtained for both sparse arrays.

In 128 FPA reference, the same trend happens in the 48 and 64 elements sparse arrays, which are considered a reduced number of elements in the sparse array considering the search

space. However, it is possible to see that the MSSIM of the images generated with the sparse arrays found using an RP FF has more than 0.5 difference in the 44, 64 and 88 elements sparse array. This happens because the sparse arrays have higher lengths and, consequently, better lateral resolution. In Strategy 1, the lateral resolution has a higher contribution to a higher MSSIM, as it is compared with the 128 FPA. In the 96/128FPA result, the sparse array found using the proposed FF has a considerable higher MSSIM. The 96/128 FPA found using the RP FF is one of the cases where the array has a low RP FF value but generates images with undesired qualities, such as high artefact intensities and low lateral resolution. In the last two settings (102 and 110).

Under Strategy 2 in Table 5, the Ref PSF and Ref RR show the size of the FPA used as a reference to compare with the sparse arrays found. For example, the 66 elements sparse array found using the proposed FF has a respective size of 76 FPA, and the one found using the RP FF has a size of 84 FPA. In the 48 and 66 elements sparse array of the 96 FPA search space, the MSSIM values are considerably higher for the images generated using the sparse array found with the proposed FF. This same happens in the 48, 64 and 88 sparse array elements of the 128 FPA search space. As this strategy focuses more on the artefact intensities, it is possible to see that the images generated using the sparse arrays found with the proposed FF values sparse arrays configurations that generate images with a balance between lateral resolution and contrast. In the other results, the MSSIM values are higher in most cases.

Table 5 – MSSIM calculated between an image generated with a sparse array and a reference image

Strategy 1											
Reference Elements	96					128					
	48	66	72	80	88	48	64	88	96	102	110
Sec3 - PSF	0.69	0.79	0.84	0.92	0.97	0.64	0.70	0.81	<b>0.81</b>	0.84	0.89
Sec3 - RP	0.68	0.82	0.84	0.92	0.97	0.89	<b>0.78</b>	0.86	0.58	0.88	0.90
Sec6 - PSF	0.65	0.75	0.82	0.87	0.95	0.57	0.65	0.78	<b>0.77</b>	0.82	0.88
Sec6 - RP	0.61	0.77	0.81	0.89	0.96	<b>0.63</b>	<b>0.77</b>	<b>0.83</b>	0.54	0.86	0.89
Sec6 - PSF	0.67	0.81	0.85	0.92	0.98	0.65	0.75	0.85	<b>0.84</b>	0.88	0.93
Sec6 - RP	0.69	0.82	0.86	0.93	0.98	<b>0.70</b>	<b>0.84</b>	<b>0.90</b>	0.55	0.92	0.92
Strategy 2											
Ref PSF	60	76	94	94	94	76	98	102	102	112	126
Ref RR	78	84	94	94	94	118	126	126	126	126	126
Elements	48	66	72	80	88	48	64	88	96	102	110
Sec3 - PSF	<b>0.94</b>	<b>0.93</b>	0.84	0.91	0.97	<b>0.85</b>	<b>0.93</b>	<b>0.96</b>	<b>0.93</b>	<b>0.97</b>	0.91
Sec3 - RP	0.67	0.81	0.85	0.91	0.97	0.69	0.78	0.85	0.58	0.87	0.89
Sec6 - PSF	<b>0.92</b>	<b>0.90</b>	0.81	0.88	0.96	<b>0.81</b>	<b>0.89</b>	<b>0.94</b>	<b>0.91</b>	<b>0.95</b>	0.89
Sec6 - RP	0.60	0.77	0.82	0.90	0.95	0.64	0.77	0.82	0.53	0.85	0.87
SecF - PSF	<b>0.97</b>	<b>0.95</b>	0.86	0.93	0.98	<b>0.90</b>	<b>0.96</b>	<b>0.98</b>	<b>0.95</b>	<b>0.98</b>	0.94
SecF - RP	0.65	0.81	0.87	0.94	0.98	0.71	0.85	0.91	0.55	0.91	0.91

The contrast to ration (CNR) of the phantom images can be analysed to elucidate this better relationship between lateral resolution and contrast for the sparse array found using the proposed fitness function. Table 6 illustrates the CNR calculated using (37) for Sections 3, 6

and F of the phantom using all the best sparse arrays and the respective 96 and 128 FPA, where the best results between the sparse arrays are highlighted.

Table 6 – CNR of section 3, 6 and F of the phantom image generated by the sparse arrays and the 96 and 128 FPA

Setting Elements	96					128					
	48	66	72	80	88	48	64	88	96	102	110
Sec3 FPA	11.64	11.64	11.64	11.64	11.64	11.62	11.62	11.62	11.62	11.62	11.62
Sec3 (PSF)	<b>11.08</b>	<b>11.64</b>	11.69	<b>11.94</b>	<b>11.78</b>	<b>11.37</b>	<b>11.55</b>	<b>11.62</b>	<b>11.64</b>	<b>11.54</b>	<b>11.20</b>
Sec3 (RP)	9.62	10.36	<b>11.84</b>	11.90	11.77	10.39	10.36	10.98	10.46	11.04	10.94
Sec6 FPA	10.96	10.96	10.96	10.96	10.96	10.92	10.92	10.92	10.92	10.92	10.92
Sec6 (PSF)	<b>10.59</b>	<b>10.74</b>	<b>10.82</b>	10.89	10.94	<b>10.53</b>	<b>10.65</b>	<b>10.84</b>	<b>10.94</b>	<b>10.88</b>	<b>10.78</b>
Sec6 (RP)	9.09	9.90	10.75	<b>10.95</b>	<b>10.98</b>	9.46	9.00	9.81	9.43	10.24	10.18
SecF FPA	11.54	11.54	11.54	11.54	11.54	11.55	11.55	11.55	11.55	11.55	11.55
SecF (PSF)	<b>10.74</b>	<b>11.53</b>	<b>11.62</b>	<b>11.66</b>	<b>11.60</b>	<b>11.31</b>	<b>11.35</b>	<b>11.52</b>	<b>11.68</b>	<b>11.60</b>	<b>11.39</b>
SecF (RP)	9.57	10.52	11.58	11.63	11.58	10.90	11.13	11.15	10.65	11.08	11.08

The sparse arrays found using the proposed fitness function have higher CNR compared to the arrays found using the RP FF, with exception of 3 cases. Although these sparse arrays have a better lateral resolution, the artefact intensity has a higher level, showing that the RP FF has a poor ability to evaluate sparse arrays that generate an image with a good balance between lateral resolution and contrast. The proposed FF considers good arrays the ones that have a better balance between lateral resolution and side lobes' intensity. Furthermore, the RP FF has the problem of miss judge arrays where one with high FF generates better images than one with lower FF, which does not happen with the proposed FF.

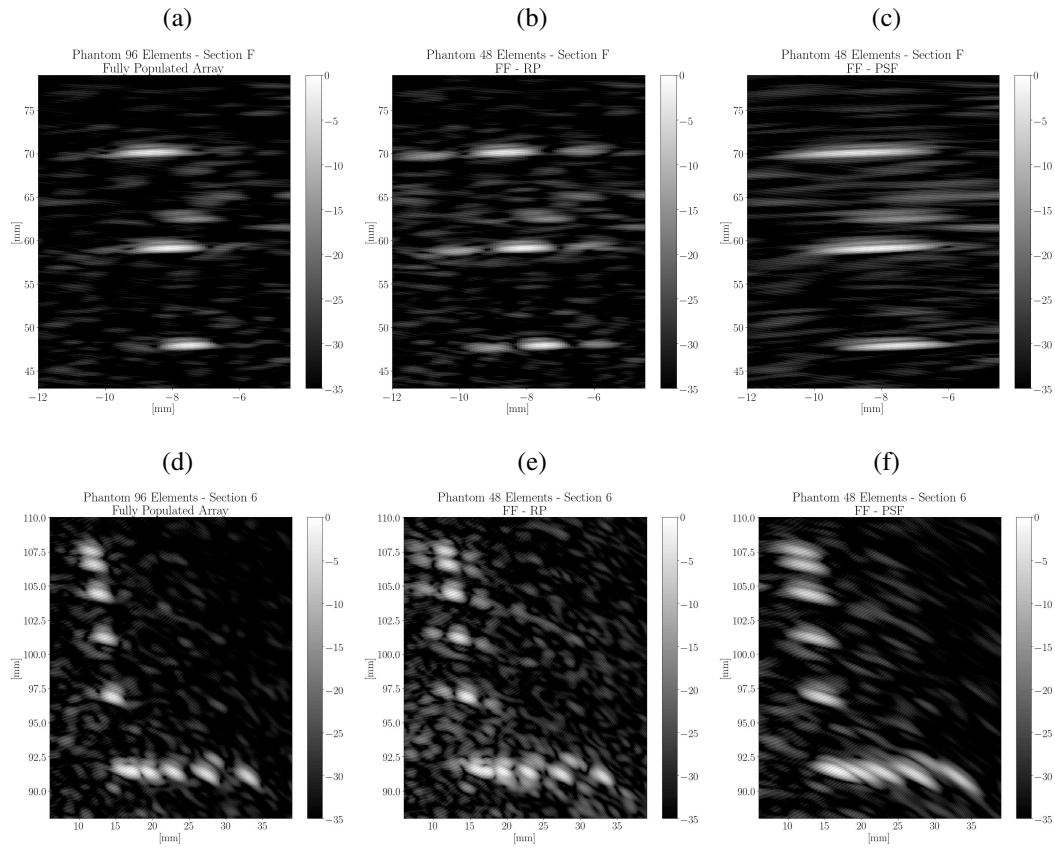
Figure 37 illustrates the phantom images generated in sections F and 6 for the 48 elements sparse array under the 96 setting. The 96 FPA images are given in (a) for section F and (d) for section 6. In (b), section F of the phantom is generated using the sparse array found using the FF based on the radiation pattern. As it can be seen, the lateral resolution looks similar to the 96 FPA image (a). However, due to high side lobes, there is a high artefact intensity aside the twisted wire. In comparison, section F generated by the 48 sparse arrays found using the proposed FF (c) does not have this high-intensity artefact but there is a loss in lateral resolution.

The interference caused by the high side lobes is more clear when Section 6 is analysed. In (e), the image was generated using the sparse array found using the RP FF. It is possible to see that the interference in the lower wires makes its identification difficult. On the other hand, the image generated by the sparse array found using the proposed FF has a loss in the lateral solution as the wires are wider in this image but it has better contrast.

As the number of elements in the sparse array increases in the setting 96, both sparse configurations found using the two FF have the same dimension equivalent to a 94 FPA size. The CNR and MSSIM are close to each other, as the phantom images (Figure 38).

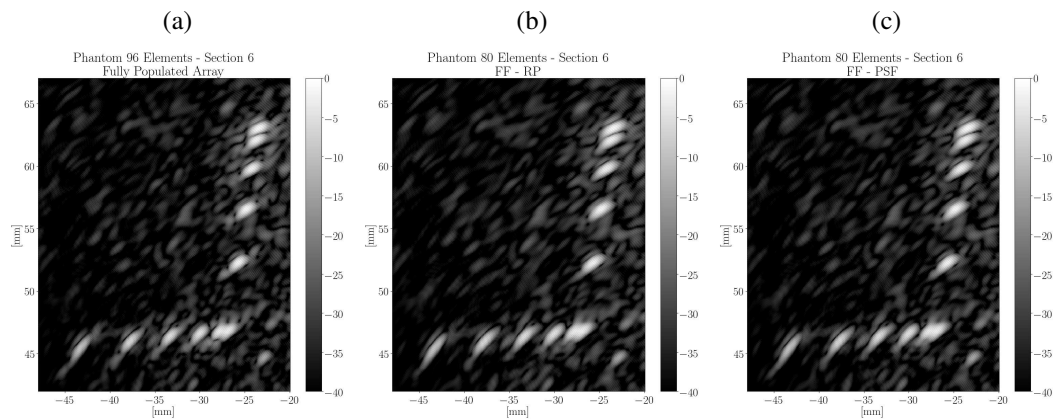
For the sparse configurations under setting 128, the same trend happened. For the sparse arrays with a lower number of elements (48,64 and 88), the arrays found using the RP FF had

Figure 37 – Section F of the phantom generated using the (a) 96 FPA, (b) the best 48 elements sparse array found using the FF based on radiation pattern and (c) the best 48 elements sparse array found using the proposed FF. Section 6 of the phantom generated using the (d) 96 FPA, (e) the sparse array found using the FF based on radiation pattern and (f) the 48 elements sparse array found using the proposed FF.



Source: Author

Figure 38 – Section 3 of the phantom generated using the (a) 96 FPA, (b) the 80 elements best sparse array found using the FF based on radiation pattern and (c) the 80 elements best sparse array found using the proposed FF.



Source: Author

better lateral resolution but with worse contrast. As the number of elements in the sparse array increases (102 and 110), the images are similar in contrast and lateral resolution.

The proposed FF considers good apertures that have an equilibrium of lateral resolution and contrast compared to the RP FF. Moreover, sometimes the sparse array considered the best with the lower values in the RP FF does not mean that the array will generate good images.

For example, the best 96 elements sparse array found using the RP FF generates a phantom image with high artefacts' intensity. Figure 39 illustrates phantom images of sections F and 6 generated using different arrays configurations. In (a) and (d), the phantom image is generated using the 128 FPA. In (b) the section F image is generated using the best 96 elements sparse array found using the RP FF, it is possible to see a high artefact intensity aside the twisted wires. In Figure 39 (e) the sum of intensities makes the interpretation of the image confusing and hard to identify the wires.

Section F of the Phantom image generated by the best 96 sparse arrays found using the proposed FF is illustrated in Figure 39 (c). As it can be seen, the lateral resolution is lower but the artefacts besides the wires images do not appear with the high intensity as in Figure 39 (a) and (b). This also makes the interpretation of section 6 (f) easier as it is more clear to see the wires in the image, although it is not possible to identify the two twisted wires close to each other, as highlighted in the image.

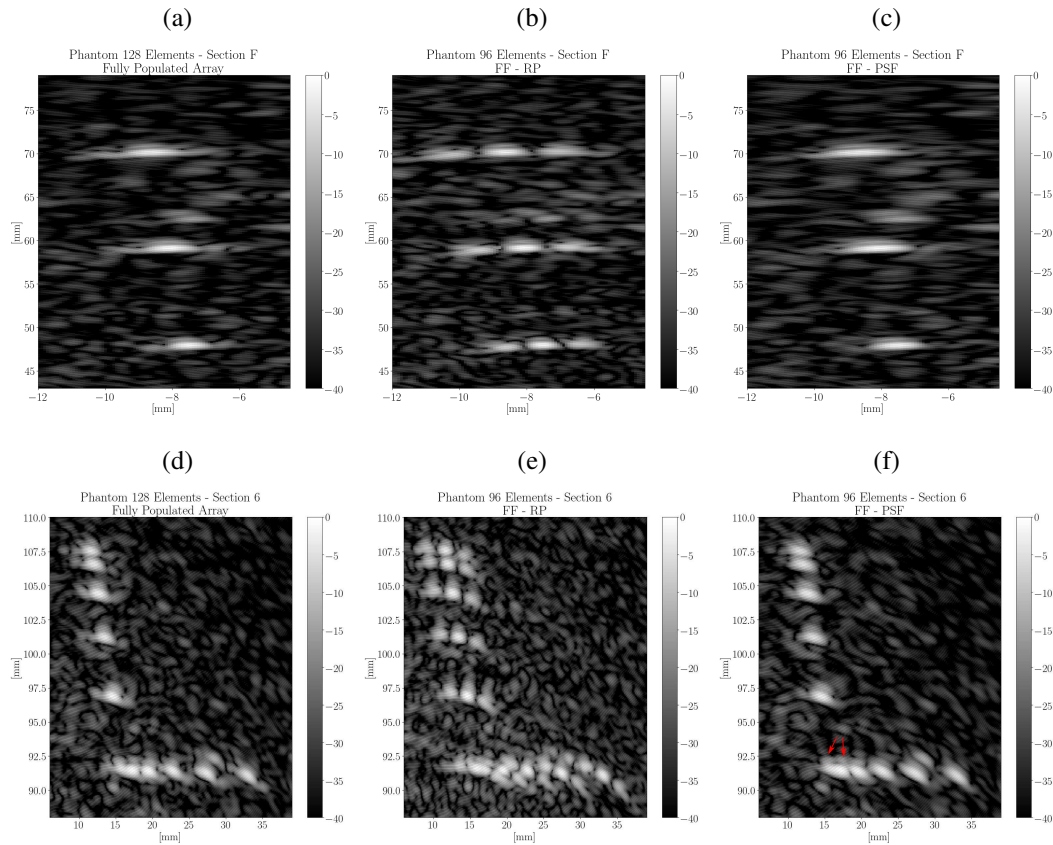
### 3.4 COMMENTS

This chapter collaborates on different aspects of the linear sparse array design and will be submitted in the future to a journal. The new codification with the continuous optimization algorithms is able to control the number of elements in the sparse array without penalization function and was able to find better sparse array configurations with better FF compared to the presented in the literature. Moreover, it was noticed that the RP FF fails to distinguish between good and bad apertures, as some sparse configurations generate PSFs with good lateral resolution and low artefact intensity but has a high FF value. In this way, a new fitness function was proposed that uses the energy and entropy extracted from a PSF. This new FF aims to correctly evaluate sparse array configurations that consider maintaining a reasonable lateral resolution and contrast.

The phantom results were able to experimentally show that this goal was achieved. For configurations that have a low number of elements, the sparse arrays found using the proposed FF maintain a good lateral resolution and contrast. As the number of elements increases, the images generated by the sparse arrays found using the two FF were the same. However, as the RP FF sometimes fails to distinguish good and bad apertures, the best sparse array with 96 elements has high artefact intensity that makes the image unrecognizable.

Although the linear arrays presented in this work are set to a  $0.5 \lambda$  grid, it is possible to

Figure 39 – (a) Section F and (d) Section 6 of the phantom generated using the 128 FPA, (b) and (e) the phantom images generated by the 96 elements best sparse array found using the FF based on radiation pattern and (c) and (f) the phantom images generated by the 96 elements best sparse array found using the proposed FF.



Source: Author

remove this grid and give more freedom to the elements to be placed and better results found. Moreover, the synthetic aperture technique can be used to create a low-cost system, which increases access to medical care in poor and developing countries. The calculation of the PSF is still computationally costly to be used in 2D sparse array design and alternatives are necessary to evaluate the configurations.

During the development of this work, the synthetic aperture technique was used, and the phantom images were generated using the combinations of emitter and receivers signals of the FMC. The acquisition time of the FMC was not considered in this study, as the signals were already stored in memory. However, it is easy to see that the sparse configurations reduce this time as fewer elements are used compared to an FPA. Another alternative to decrease the acquisition time in the synthetic aperture technique is to create an acquisition strategy where not all emitter and receivers combinations are sampled, which is attractive for 2D arrays, where reducing the acquisition time enables to use of real-time ultrasonic applications for 2D arrays using synthetic aperture.

## 4 ACQUISITION STRATEGY FOR NON-GRID APERTURES

In this chapter, a guide to design ultrasonic synthetic aperture systems for non-grid two-dimensional sparse arrays such as spirals or annular segmented arrays is presented. It presents an algorithm that identifies which elements have more significant impact on the beam pattern characteristics and uses this information to reduce the number of signals, the number of emitters and the number of parallel receiver channels involved in the beamforming process. Consequently, we can optimise the 3D synthetic aperture ultrasonic imaging system for a specific sparse array, reducing the computational cost, the hardware requirements and the system complexity. Simulations using a Fermat spiral array and experimental data based on an annular segmented array with 64 elements are used to assess this algorithm.

This chapter is part of the work published by DE SOUZA et al. (2021)

### 4.1 THE COARRAY ANALYSIS

The development of real-time ultrasonic imaging systems based on arrays is a complex issue that encompasses different fields of study, such as material science (PARK et al., 2020), manufacturing (SUN et al., 2015), physics (LI; CHI, 2018), and electronic integration (BIRK et al., 2014). Signal processing also plays a considerable role in this challenge (KARAMAN et al., 2009; HOCTOR; KASSAM, 1990), mainly to establish a good trade-off between hardware complexity and image requirements.

Synthetic Aperture Focusing Techniques (SAFT) allow the system designer to reduce hardware requirements at the expense of image frame rate (KARAMAN et al., 2009; HOCTOR; KASSAM, 1990; LOCKWOOD et al., 1998; RASMUSSEN; JENSEN, 2014; HOLMES et al., 2005). A synthetic aperture imaging system is based on a two-step process: data acquisition and beamforming. The complexity and necessary resources associated with both processes are determined by what we call here the acquisition strategy (*ACQ*). The data acquisition sub-process follows this strategy, which is based on the independent capture of the signals that correspond with each emission/reception pair (e-r pair) for the selected aperture. The most complete acquisition strategy is the Full Matrix Capture (*FMC*), which, for an  $N$ -element aperture, captures all the  $(N \times N)$  signals (one for each e-r pair). Then, the beamforming sub-process performs the compensation of emission and reception delays at each point of the Region Of Interest (ROI) using the *TFM* given in (28), where  $s_{er}(t)$  is the signal received by the element  $r$  when  $e$  is the emitter.

Although the *TFM* generates high-quality images, the *FMC* offers a poor trade-off between hardware parallelism and frame rate. The ratio between the number of signals ( $N \times N$ ) and the number of parallel electronic reception channels determines the number of acquisition operations. As a result, low parallelism in reception increases the acquisition time. Further-

more, with this number of signals, the computational cost to generate the *TFM* image is high (HOLMES et al., 2005; ROMERO-LAORDEN et al., 2016).

As explained in Chapter 2, the combination of emitters and receivers in an array can be modelled as a sampling grid known as coarray (HOCTOR; KASSAM, 1990). The emitter/receiver element combination corresponds to a spatial frequency (KARAMAN et al., 2009), and signals that occupy the same spatial frequency in the coarray can be considered redundant for the beamforming process. In this sense, in a matrix array, the *FMC* has a high degree of redundancy and, if redundant information is eliminated, in exchange for a reduction in signal-to-noise ratio, it is possible to reduce the computational cost and simplify the acquisition process (BRUNKE; LOCKWOOD, 1997; HOCTOR; KASSAM, 1990; KARAMAN et al., 2009).

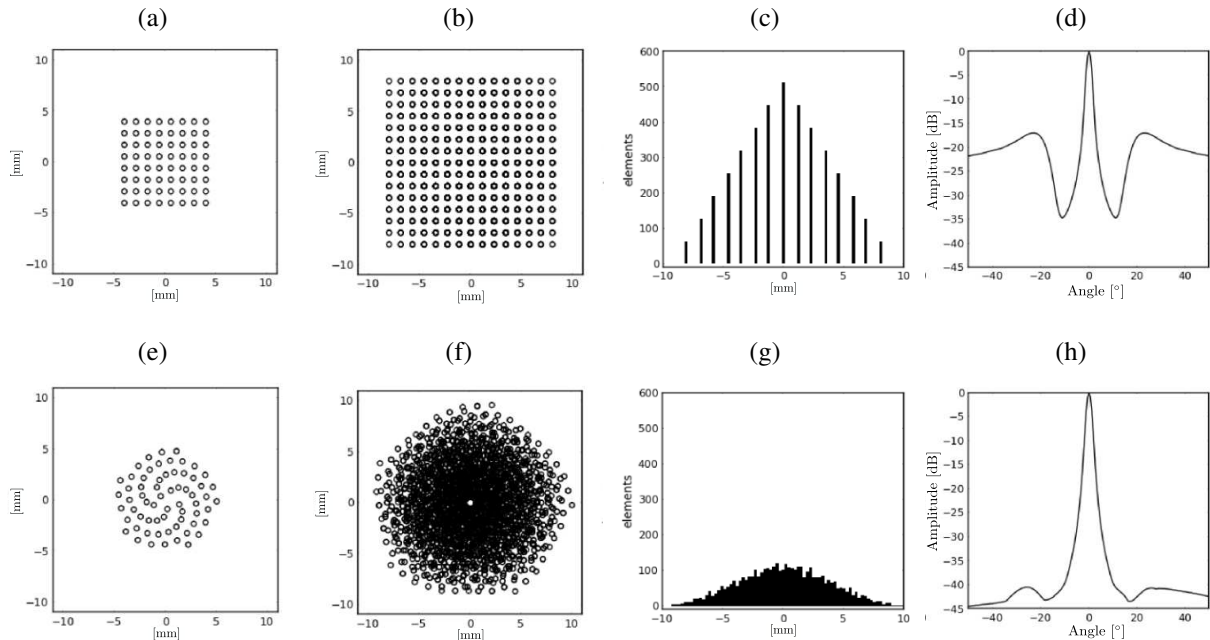
For matrix apertures, this analysis provides a straightforward way to simplify system acquisition design (KARAMAN et al., 2009; HOCTOR; KASSAM, 1990; LOCKWOOD et al., 1998; MARTÍN et al., 2012). The most efficient coarray is the Minimum Redundancy Coarray (*MRC*), where just one element occupies each spatial frequency or coarray location (ISHIGURO, 1980). Such a solution, using the minimum number of signals, provides the maximum degrees of freedom and lateral resolution and avoids grating lobes. Moreover, depending on the available parallel resources, it can be achieved with different acquisition strategies (MARTÍN et al., 2010).

When considering non-matrix arrays (e.g. spiral or circular distributions), the redundancy identification becomes a complex issue (MARTÍNEZ-GRAULLERA et al., 2010; SCHWARTZ; STEINBERG, 1998; DIARRA et al., 2013). The differences between matrix and non-matrix are presented in Figure 40(a) and (e), with their corresponding coarrays illustrated in (b) and (f), respectively. Both apertures have the same number of elements ( $N = 64$ ), and the same dimensions (diameter,  $D = 16\lambda$ ).

Figure 40(c) and (g) illustrate an equivalent linear array for the matrix and spiral array, where the elements are projected in the  $x$ -axis ( $\phi = 0^\circ$ ). Two characteristics are highlighted for the equivalent linear array. First, the matrix array has a high degree of coincidence in its element location and concentrates them in very few locations. Second, the spiral array elements are less coincident and produce a dense equivalent linear array. The matrix array generates a regular coarray of  $\lambda$  spacing grid, while the spiral array generates a coarray with an irregular pattern that has smaller and irregular spacing between elements. This element distribution has consequences on the beam pattern (wideband response,  $BW = 60\%$ ) because it reduces the number of constructive interferences in the sidelobe region (Figure 40(d) and (h)).

Although sparse configurations based on non-matrix arrays allow better space distribution compared to sparse matrix arrays (MARTÍNEZ-GRAULLERA et al., 2010; SCHWARTZ; STEINBERG, 1998), they also show significant levels of redundancy. The reciprocity principle ( $s_{er}(t) \equiv s_{re}(t)$ ) can be used to reduce some redundancy. Considering the coarray definition given in (27), each emitter/receiver pair and its associated signals  $s_{er}(t)$  corresponds to a unique

Figure 40 – For matrix arrays: (a) array structure, (b) coarray footprint, (c) equivalent array projection at  $\phi = 0^\circ$ , and (d) radiation pattern at  $\phi = 0^\circ$  (wideband response, BW=60%). For spiral array aperture: (e) array structure, (f) coarray footprint, (g) equivalent array projection at  $\phi = 0^\circ$ , and (h) radiation pattern at  $\phi = 0^\circ$  (wideband response, BW=60%).

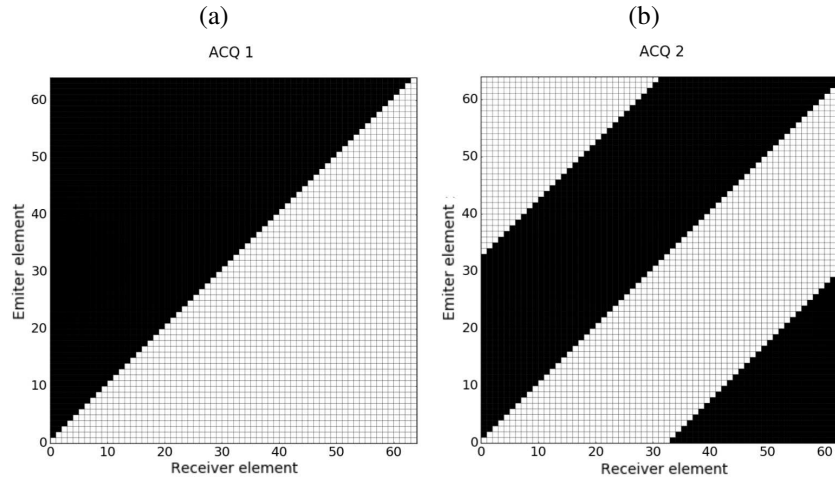


Source: Author

coarray element. By the reciprocity principle, it can be considered that  $s_{er}(t)$  is equal to  $s_{re}(t)$ , introduce equivalent information in the beamformer and can be removed without any loss. The respective coarray elements,  $\vec{C}_{er}$  and  $\vec{C}_{re}$ , occupy the same spacial space and, therefore, can be considered redundant. Figure 41(a) illustrates the *ACQ1* acquisition strategy, where the white squares correspond to the combination of emitters  $e$  and receivers  $r$  used for acquisition. The number of signals involved is reduced by almost half. Moreover, in order to reduce the number of parallel channels and, consequently, the electronic resources, the acquisition strategy *ACQ1* can be rearranged to create the *ACQ2* alternative, as shown in Figure 41(b).

In the specific case of a 64 elements array, depicted in Figure 41, *ACQ2* reduces the number of signals involved from 4096 to 2080, and the number of receiver parallel channels from 64 to 33. This structure can be reorganised to obtain a simpler electronic implementation. Figure 42(a) illustrates a more compact representation of *ACQ2*, where the y-axis corresponds to the 64 emitter elements and the x-axis the 33 receiver channels (A/D channels). Reciprocity allows us to empty almost half of the acquisition matrix, and we can make a rearrangement of columns to reduce the number of A/D converters needed. At each position of the matrix, the coloured squares represent the receiver elements allocated for the respective emitting transducer and A/D channel. It is possible to see from this matrix that channel 33 needs to access all 64 elements as it handles the pulse-echo signals. For the other converters, each column is filled

Figure 41 – Matrix presentation of acquisition strategy (*ACQ*) for a generic array composed of 64 elements. White cells are the active channels. (a) *ACQ1* - the reciprocity principle has been applied to reduce the number of signals. (b) *ACQ2* - the reciprocity principle also has been used to optimise the electronic resources.



Source: Author

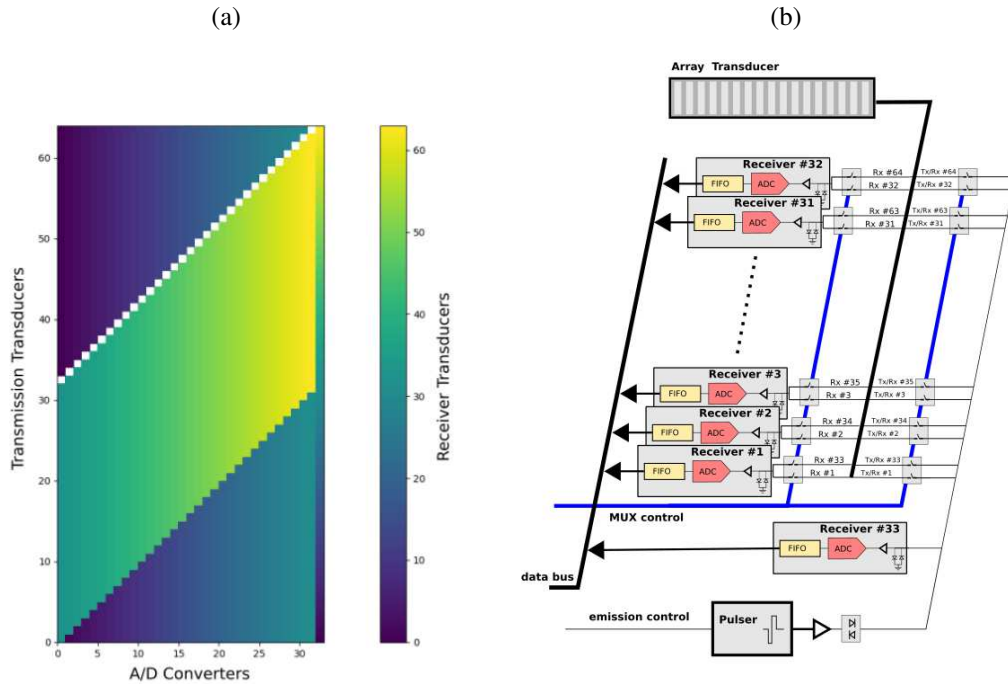
with two receiver elements to implement the acquisition strategy *ACQ2*. For example, column 1, which corresponds to A/D converter 1, is filled at the bottom with receiver 33 and changes to receiver 1 after emission 33. In this implementation, the 32 first receivers channels share each only two different elements, and the multiplexer is simplified. Moreover, there are switched-off receiver operations (white cells in Figure 42(a)) that occur because converter 33 is in charge of these acquisitions.

In Figure 42(b), there is a model of the ultrasonic system based on this acquisition strategy. In this case, the multiplexer is implemented in two independent nets controlled, each one, by 64 switches. In one net, each receiver channel, from 1 to 32, is associated with two transducers (the  $i^{th}$  and  $(32+i)^{th}$ ). In the other net, the 64 switches share the connection between the pulser (emitter) and the 33 receiver circuit.

It is important to highlight that reciprocity does not depend on how the elements are distributed, and it can be applied to linear and bidimensional configurations. However, some caution should be applied in the distribution of the Tx/Rx pairs. For example, to avoid image artefacts caused by non-linear and shadowing effects in the propagation medium, it is important to distribute emission/reception pairs homogeneously to avoid the concentration of emitters (or receivers) on one specific side of the aperture.

The coarray can be used to identify signals that introduce the same information in the beamforming. In the case of the reciprocity principle, the elements  $\vec{C}_{er}$  and  $\vec{C}_{re}$  shares identical position in the coarray and can be easily removed to create *ACQ1* and *ACQ2*. This principle can be applied to any array, but the hardware and data reduction are limited to marginally half. In non-grid arrays, the superposition of the elements is rare, which turns difficult to find

Figure 42 – Compact Representation of ACQ2 (a) and an ultrasonic acquisition system (b).



Source: Author

and eliminates more signals that introduce redundancy. In this way, it is necessary to study a different method to check redundancy in the coarray.

#### 4.1.1 Identification of redundancy in the coarray

Redundancy is produced when a coarray position is filled by more than one coarray element. In non-matrix distributions, where there is no-grid, once the reciprocity principle is used, the positions of the coarray elements are rarely coincident (see Figure 40(b)), so all of them should be considered as non-equivalent (non-redundant). Nevertheless, some coarray elements could be considered equivalent for the beamforming process if there is a minimum distance between them. This minimum distance can be evaluated by using the focusing delay quantification theory (MAGNIN et al., 1981; PETERSON; KINO, 1984; STEINBERG, 1992), which states that errors introduced by the quantification of focusing delays can be rejected as long as they remain below  $(\frac{\lambda}{32})/c$ . Based on this, if the distance between two coarray elements is less than  $\frac{\lambda}{32}$ , we can consider that they introduce the same information in the beamforming process. However, if sparsity is high, the redundancy revealed by this clustering operation is very low, and a useful alternative is to study how redundancy is organised in the equivalent linear array.

From the Projection-Slice Theorem (GASKILL, 1978), the narrowband beampattern of a 2D array in a particular azimuth direction is determined by the projection of all the coarray

elements on an axis along the same direction. In this sense, two elements  $\vec{C}_{e_1 r_1}$  and  $\vec{C}_{e_2 r_2}$  are redundant in a given angle  $\phi$  if:

$$|\langle \vec{C}_{e_1 r_1}, (\sin \phi, \cos \phi) \rangle - \langle \vec{C}_{e_2 r_2}, (\sin \phi, \cos \phi) \rangle| \leq \frac{\lambda}{32}, \quad (38)$$

Although there is a specific solution for each azimuth angle, this strategy highlights redundancy. And, if the whole azimuth domain is considered, a redundancy map can be created and used to show the relationship between the different coarray elements at each azimuth angle. Essentially, this is an unstructured Radon transform where the projected elements are clustered, in sets, on a grid organised along the azimuth and radial axis. This grid is created respecting the Nyquist criterion, which establishes that the resolution in the radial dimension is given by  $\lambda/2$ . And, in the angular axis, the resolution is defined by the main lobe width of the coarray. Hence, the angular discretization is given by  $\phi_p$ :

$$\phi_p = \frac{1}{2} \arcsin \frac{\lambda}{2D}. \quad (39)$$

This discrete grid is a matrix of sets shaped as  $N_p \times N_g$ , where the number of angles  $N_p$  is:

$$N_p = \left\lceil \frac{4\pi}{\arcsin(\lambda/(2D))} \right\rceil, \quad (40)$$

and  $N_g$  is:

$$N_g = \left\lceil \frac{2D}{\lambda/2} \right\rceil + 1, \quad (41)$$

Then, the coarray element  $C_{er}$  is stored in a set at  $[p, g]$  position if the following clustering condition is met:

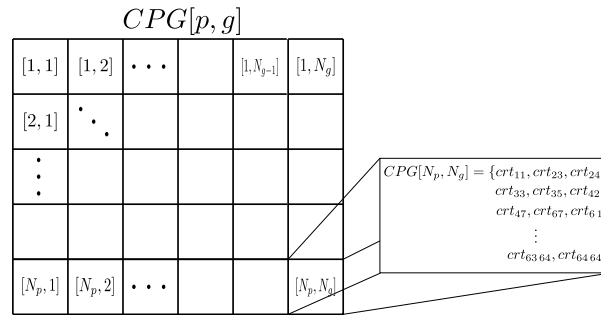
$$\left| \left\langle \vec{C}_{er}, (\sin(k\phi_p), \cos(k\phi_p)) \right\rangle - g \frac{\lambda}{2} - D \right| < \frac{\lambda}{32}, \quad (42)$$

This structure, named Coarray Projection Grid (*CPG*), can be used to study the redundancy of any acquisition strategy and describes the potential of an aperture to be optimised. Two parameters can be obtained from it: the occupancy rate of the *CPG* ( $M_o$ ), which is the percentage ratio between occupied locations and the total number of possible locations, and the redundancy level ( $M_r$ ), which is the mean number of signals per occupied *CPG* location and indicates if an optimisation process can be performed. Figure 43 illustrates a *CPG* for an array with  $N$  emitters and receivers, where each position  $[p, g]$  has the elements of coarray that meet condition (42).

## 4.2 ACQUISITION STRATEGIES ALGORITHM

We define a particular acquisition strategy *ACQ* as a list of e-r pairs used to obtain the data set. To evaluate its performance, we can use  $M_o$ ,  $M_r$  and the number of signals involved

Figure 43 – Example of Coarray Projection Grid (*CPG*) where each  $[p, g]$  position contains a set of coarray elements  $\vec{C}_{er}$  that meet the condition (42)



Source: Author

( $N_s$ ). These values are computed with the help of a matrix named *MAP*, which has similar dimensions as *CPG* and works as a counter to the number of elements at each respective grid position.

For the ideal *ACQ*, all *MAP* positions should be filled with only one coarray element ( $M_o = 100\%$  and  $M_r = 1$ ), meaning that the beampattern generated by this *ACQ* has the maximum lateral resolution, as well as equivalent distribution of side lobes at each azimuth angle.

In the case of a sparse array, the *CPG* is sparsely and irregularly filled and it cannot achieve the ideal *ACQ*. However, we can reduce the number of signals involved by smoothing the irregular shape. This can be achieved by eliminating overlapping coarray elements while the occupancy  $M_o$  is maintained. With this objective, a two-step procedure is proposed to reduce the number of signals and also consider hardware restrictions to optimise system resources.

#### 4.2.1 Step one: Generation of the *CPG* database

First, *FMC* is used as *ACQ*. Then, the *CPG* is assembled and the occupancy level ( $M_o$ ) and redundancy level ( $M_r$ ) are calculated. The  $M_o$  indicates how the aperture can fill the *CPG*, and it is desirable that any proposed *ACQ* has the same  $M_o$ . The  $M_r$  indicates how much room there is for optimisation. Although our objective is to reduce  $M_r$  maintaining  $M_o$ , this will also reduce  $M_r$  and will also decrease averaging and the SNR.

To make programming tasks easier, we are going to reorganise the *CPG* structure in another  $N \times N$  matrix. Each  $[e, r]$  position of this new matrix, named Inverse Coarray Projection Grid (*ICPG*), corresponds to the coarray element  $\vec{C}_{er}$ . Inside each position, the different  $[p, g]$  values that  $\vec{C}_{er}$  satisfy using the condition (42) will be stored. The process to create the *ICPG* database is defined in algorithm 1.

The *ICPG* makes it easier to evaluate the impact of a specific element on the acquisition strategy, introduces specific conditions for the system (like avoiding specific elements), and

---

**Algorithm 1** Generation of the *ICPG* database
 

---

```

1: for  $e$  in  $\text{range}(N)$ :
2:   for  $r$  in  $\text{range}(N)$ :
3:      $ICPG[e, r] = []$ 
4:     for  $p$  in  $\text{range}(N_p)$ :
5:        $C_{buf} = \langle \vec{C}_{er}, (\sin(k\phi_k), \cos(k\phi_k)) \rangle$  projected element
6:       for  $g$  in  $\text{range}(N_g)$ :
7:         if  $(|C_{buf} - g \frac{\lambda}{2} - D| < \frac{\lambda}{32})$ 
8:            $ICPG[e, r].\text{append}([p, g])$ 
9: return  $CPG$  database

```

---

simplifies the task of introducing information in the *MAP*.

#### 4.2.2 Step two: Acquisition Strategy Design

The acquisition strategy optimisation is described in the algorithm 2, where the *ACQ* is a list of  $G_c = [e, r]$  values that define the strategy ( $e$  emission transducer and  $r$  reception transducer). This algorithm created is a simple case, where we only have a limited number of emitters and parallel channels. However, it is straightforward to introduce other conditions such as eliminating specific elements or using different elements for emission and reception.

The contribution of the *ACQ* to the projected coarrays is analysed in the *MAP*. The proposed heuristic selects the emission/reception configuration (*ACQ*) that best fills the *MAP* matrix with the minimum number of signals. The maximum number of allowed emitters and parallel reception channels ( $MPD[0, 1]$ ) is checked using a matrix of counters shaped as  $2 \times N$  ( $PD$  in algorithm 2).

The algorithm initialises the *MAP* matrix, the  $PD$  and the sequence *CAN* of emission/reception pairs. If there are no restrictions, *CAN* is initialised with all combinations of emitters and receivers (*FMC*). The same happens for  $PD$ , where it can be used for several hardware adjustments, like excluding specific elements of the receiver channels. After that, the algorithm makes several loops. At each loop, the contribution of each coarray element ( $i0 = [e, r]$ ) to *MAP* is evaluated by how much information is introduced (the number of positions that are filled where  $MAP[p, g] = []$ , *FP* counter) and by how much redundancy is introduced (positions where  $MAP[p, g] \neq []$ , *NFP* counter). The process is controlled by Global Free Positions (*GFP*) and Global Non-Free positions (*GNFP*) that are the counters of the candidate ( $G_c$ ) to be incorporated to *ACQ*. If the emission element  $e$  and reception  $r$  has free parallel channels, and the pair  $[e, r]$  contributes with more information ( $FP > GFP$ ) and less redundancy ( $NFP < GNFP$ ) to the *MAP*, it becomes a candidate ( $G_c = i0$ ) and *GFP* and *GNFP* are updated. At the end of the round, the candidate is attached to *ACQ*, the *MAP* and *CAN* are updated and a new round begins with the remaining elements, until  $GFP = 0$ , which means that the sequence can not fill more new *MAP* positions and adding more elements would increase redundancy.

**Algorithm 2** Algorithm for selecting the acquisition strategy(*ACQ*)

---

```

1:  $MAP = \mathbf{zeros}(N_p, N_g)$  Filling matrix
2:  $ACQ = []$  initialisation acquisition strategy
3:  $GFP = 1, GNFP = 1$  Global position counters
4:  $CAN = []$  signal sets
5: for  $e$  in range( $N$ ):
6:     for  $r$  in range( $N$ ):
7:          $CAN.append([e, r])$ 
8:  $PD = \mathbf{zeros}(2, N)$  Parallelism Degree per element counter
9: while ( $GFP > 0$ ):
10:     $GFP = 0, GNFP = 0$ 
11:    for  $i0$  in  $CAN$ :
12:        if ( $PD[[0, 1], i0] < MPD[0, 1]$ ).all: Tx:Rs parallelism check
13:             $NFP, FP = \mathbf{compute\_FP}(MAP, ICPG[i0])$ 
14:            if ( $GFP < FP$ )or(( $GFP == FP$ )and( $NFP < GNFP$ )):
15:                 $GFP = FP; GNFP = NFP;$ 
16:                 $G_c = i0$ 
17:            if ( $GFP > 0$ ):
18:                 $ACQ.append(G_c)$ 
19:                 $CAN.remove(G_c)$ 
20:                 $PD[0, G_c[0]] += 1$ 
21:                 $PD[1, G_c[1]] += 1$ 
22:                for  $i0$  in  $ICPG[G_c]$ :
23:                     $MAP[i0] = MAP[i0] + 1$ 
24: return  $ACQ$  Acquisition Strategy

```

---

## 4.3 EVALUATION OF THE PROCEDURE

Two different arrays were chosen to evaluate the performance of the proposed technique. The first is a 64-elements Fermat spiral array (MARTÍNEZ-GRAULLERA et al., 2010), where simulation was used to analyse it. The second is a 64-elements segmented annular array (MARTÍNEZ et al., 2003), where simulation and several experimental ultrasonic images were generated to verify the results. The proposed algorithm was evaluated by considering the beampattern wideband response, the *MAP* occupancy level ( $M_o$ ), the redundancy level ( $M_r$ ) and the number of signals involved ( $N_s$ ).

From the beampattern, three lateral profiles are obtained at each elevation angle, the maximum, the mean and the minimum values. In the following figures, for comparison between the *FMC* and the examined designed strategy (*ACQ*), their acoustic field lateral profiles are presented. The light grey areas (contoured by dashed lines) show the result of the *ACQ*, whereas dark grey areas (contoured by solid lines) are related to the *FMC*. Furthermore, an inset shows a detail of lateral resolution for small elevation angles.

### 4.3.1 Fermat spiral array

The Fermat spiral array was designed with a diameter of  $22\lambda$ , 64 elements and a divergence angle  $\alpha = 125.764^\circ$ , central frequency  $f_c = 3.0$  MHz,  $BW = 60\%$ , operating in water ( $c = 1500$  m/s) and focused at 60 mm. The aperture and its beam pattern are shown in Figure 44: (a) array footprint, (b) coarray structure, (c) acoustic pressure, and (d) lateral profile of the acoustic pressure at each elevation angle (light grey area contoured by the dashed line).

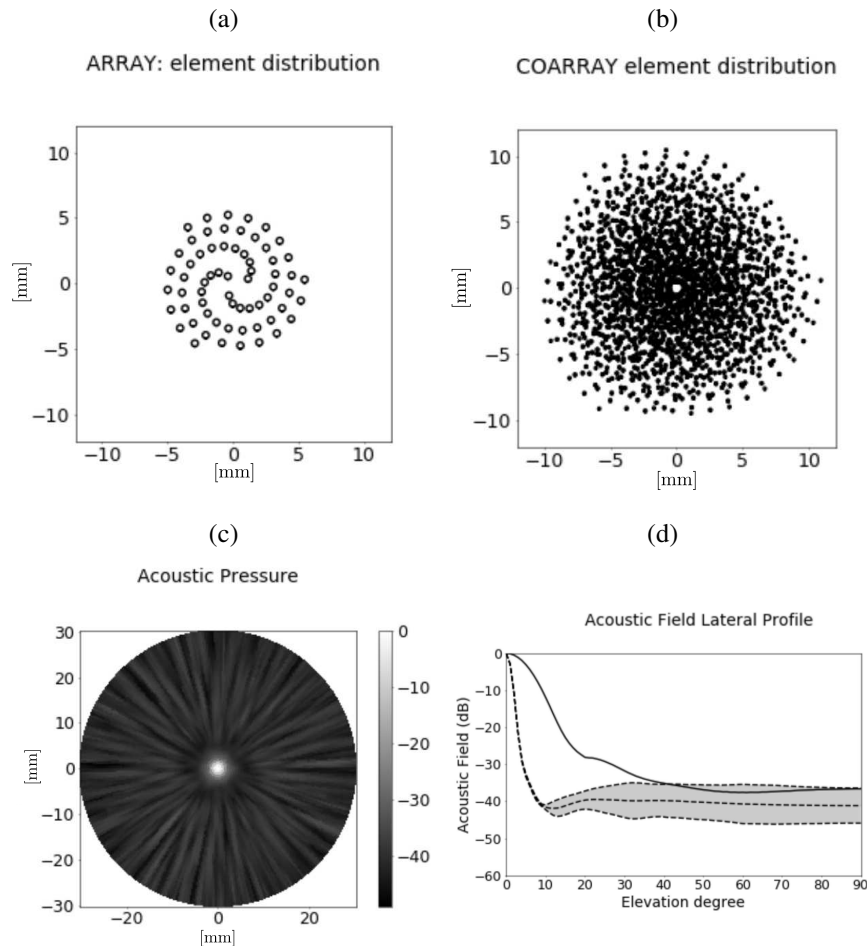
The beam pattern response (higher sidelobe profile) of a 64 elements matrix array, with its elements spaced by  $\lambda/2$  ( $8 \times 8$  matrix), is also illustrated in Figure 44 (d) with a solid line. The matrix array has a similar dynamic range ( $-30$  dB) and lowers lateral resolution than the spiral array. The specific spiral distributions aim to spread the energy in large sidelobes regions, avoiding a high concentration of energy. Thus, a higher lateral resolution is achieved with low grating lobes (MARTÍNEZ-GRAULLERA et al., 2010; SCHWARTZ; STEINBERG, 1998). In this case, the mean value of the spiral array is around  $-40$  dB with a 5 dB deviation.

By clustering the coarray elements that are less than  $\lambda/32$  apart, only six signals  $s_{ij}$  are added to the set of redundant signals (initially made up of reciprocal elements). Using the projections, the *FMC* occupies 40422 positions of the possible 49770 in the *CPG* structure; that results in an  $M_o$  of 81% and an  $M_r$  of 7.23. If the reciprocity principle is used to create an *ACQ*, which is named as *RCP* (see table 7),  $M_r$  is reduced to 3.68, which still indicates a very redundant distribution.

Then, using the proposed heuristic, the first acquisition strategy, *ACQ*(64 : 64), is illustrated in Figure 45. In this example, *MPD* is defined using 64 emission elements and 64 parallel channels ( $T_x : R_s = 64 : 64$ ) and the signals considered redundant are eliminated. Compared to the *FMC*, we achieved the same  $M_o$  with only 39% of the signals and a 59% reduction in the  $M_r$ . Also, it has reduced the reception channels. The mean number of reception channels per emission is 25, with a maximum of 32 and a minimum of 14. Furthermore, it employs 450 fewer signals than the *RCP*. Comparing the acoustic field of (64 : 64) with the original aperture, we see that the sidelobe distribution has a flattened distribution with an overall increase of only 2 dB in comparison to the *FMC* (Figure 45).

Also in Figure 45(b), four parameters are illustrated and they will be used to compare the lateral profile: the Dynamic Range (*DR*), in dBs, defined as the maximum sidelobe level relative to the main lobe level; the  $\Delta\theta_{DR}$ , in degrees, defined as the main lobe width at the level of *DR*; The Cross-Point (*CP*), in dB, defined by the level that the *ACQ* lateral profile crosses the *FMC* lateral profile; and the -6 dB main lobe width  $\Delta\theta_{-6dB}$ . It can be seen that the *ACQ*(64 : 64) lateral resolution is higher than *FMC*'s until  $CP = -21$  dB. The dynamic ranges are similar, and  $\Delta\theta_{DR}$  increases a bit, although the value of  $\Delta\theta_{-6dB}$  is smaller for the *ACQ*(64 : 64). Additional results for all *MDP* combinations analysed for the spiral array are summarised in Table 7, where  $N_s$  is the number of signals selected and  $N_c$  is the maximum number of parallel channels for

Figure 44 – The 64 element spiral. (a) array footprint, (b) coarray footprint, (c) acoustic pressure in the semi-sphere [ $\theta = 0^\circ : 90^\circ, \phi = 0^\circ : 360^\circ$ ] and (d) lateral profile showing the distribution of the sidelobes in elevation. The dashed line represents the spiral beampattern, and the light grey area within that line shows side lobe distribution at each elevation angle. The solid line is the corresponding beampattern of a 64 element matrix array.



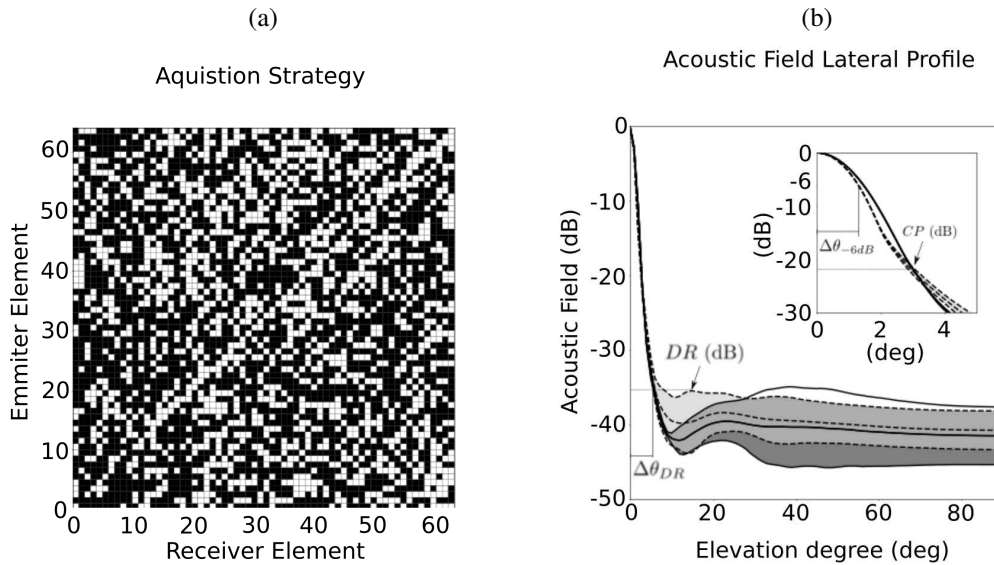
Source: Author

each strategy in reception.

The algorithm can limit the maximum number of emissions and receptions. To illustrate this, we defined the following *MPD* values for our acquisition strategies: *ACQ*(64 : 32), *ACQ*(64 : 16), *ACQ*(64 : 8), *ACQ*(32 : 64) and *ACQ*(16 : 64). The first three strategies defined that all 64 emitters elements can be used and the restriction of the algorithm is in the number of parallel receivers, with a significant restriction in the (64 : 8) case. The matrix representations of acquisition strategies obtained from the first three settings are illustrated in Figure 46(a), (b) and (c), and their lateral profile are illustrated in Figure 47 (a),(b) and (c), respectively.

In *ACQ*(64 : 32), the results obtained are similar to *ACQ*(64 : 64) (see Table 7). The number for parallel receivers is the same and, comparing the lateral profile of *ACQ*(64 : 32) (Figure 47(a)) with *ACQ*(64 : 64) (Figure 45(b)), both strategies have almost the same response.

Figure 45 – (a) strategy (64 : 64) for redundancy reduction. (b) sidelobe distribution at each elevation angle for strategy (64 : 64) (light grey area within the dashed line) and the *FMC* (dark grey area within the solid line).



Source: Author

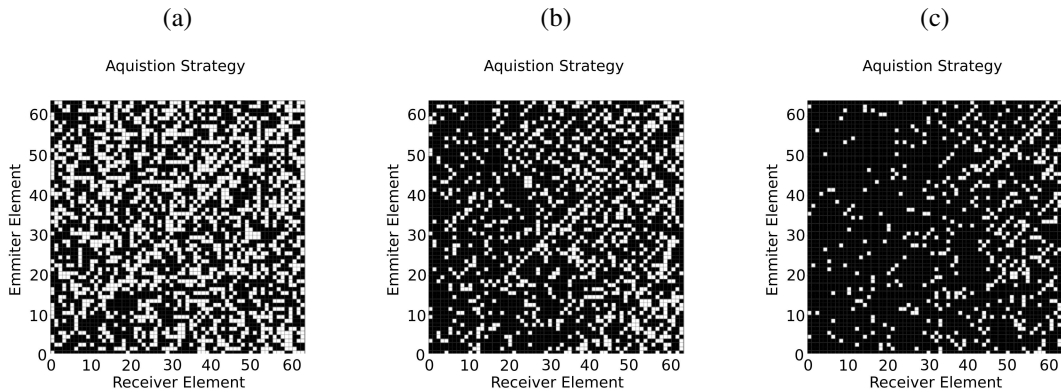
Table 7 – Fermat spiral array: performance for the *FMC*, *RCP* and all six strategies considered ( $T_x : R_x$ ).

$ACQ$	$M_o$	$M_r$	$N_s$	$N_c$	$\Delta\theta_{-6dB}$	$CP$ (dB)	$DR$ (dB)	$\Delta\theta_{DR}$
<i>FMC</i>	81%	7.23	4096	64	$2.92^\circ$	-	-35	$11.5^\circ$
<i>RCP</i>	81%	3.68	2080	33	$2.92^\circ$	-	-35	$11.5^\circ$
(64 : 64)	81%	2.93	1630	32	$2.6^\circ$	-20.9	-35.4	$15.1^\circ$
(64 : 32)	81%	2.93	1631	32	$2.6^\circ$	-20.83	-36	$14.0^\circ$
(64 : 16)	77%	2.03	1024	16	$2.34^\circ$	-20.75	-34	$13.4^\circ$
(64 : 8)	59%	1.43	512	8	$2.02^\circ$	-21.69	-28.6	$11.3^\circ$
(32 : 64)	77%	2.71	1444	50	$2.6^\circ$	-21	-33.8	$12.0^\circ$
(16 : 64)	65%	2.02	984	60	$2.66^\circ$	-18	-31.9	$12.8^\circ$

One remarkable fact, showing the benefits of the redundancy reduction, is that the response of the *FMC* has worse  $\Delta\theta_{-6dB}$  and slightly more sidelobes than  $ACQ(64 : 64)$ (Figure 45(b)) and  $ACQ(64 : 32)$  (Figure 47(a)).

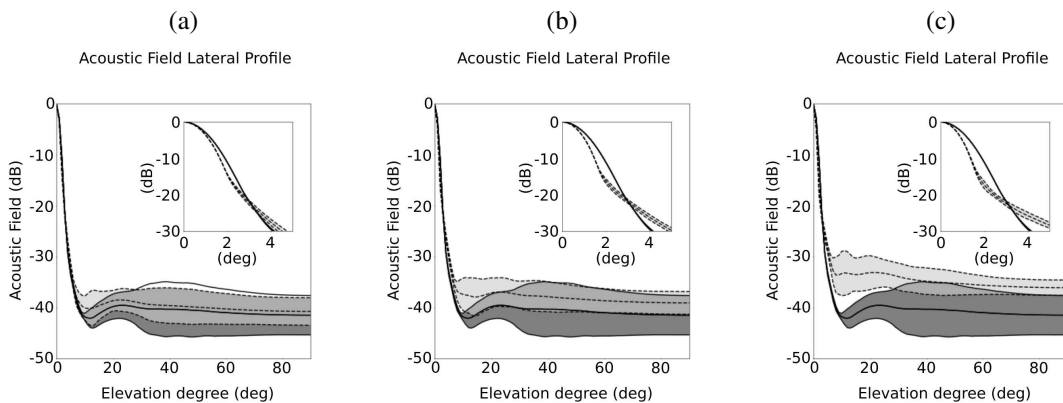
In  $ACQ(64 : 16)$  (Figure 47(b)), this configuration has vacant positions in the *CPG* ( $M_o$  decreases to 77%). Although there is a small increase in all lateral profiles, and compared to the *FMC* response, the sidelobes remain in a similar range. In  $ACQ(64 : 8)$  (Figure 47(c)), there is a significant resource reduction by using only 12% of the available signals. In consequence, the sidelobes are 5 dB higher than the *FMC* response. However, it is remarkable that  $\Delta\theta_{-6dB}$  becomes smaller for  $ACQ(64 : 16)$ , even using fewer resources.

Figure 46 – Acquisition matrix obtained from (a)  $ACQ(64 : 32)$ , (b)  $ACQ(64 : 16)$  and (c)  $ACQ(64 : 8)$ .



Source: Author

Figure 47 – Sidelobes distribution at each elevation angle for strategies (a)  $ACQ(64 : 32)$ , (b)  $ACQ(64 : 16)$  and (c)  $ACQ(64 : 16)$  (light grey area within the dashed line) and the  $FMC$  (dark grey area within the solid line).

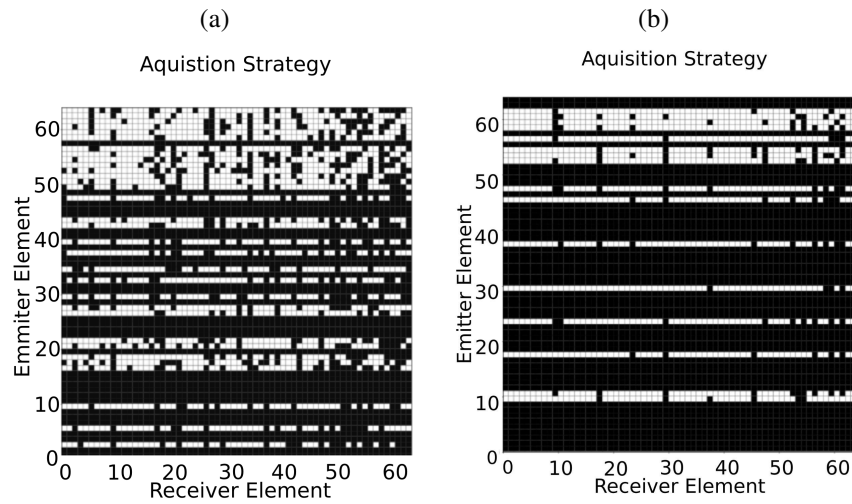


Source: Author

Figure 48 illustrates the matrix acquisition obtained from the  $ACQ(32 : 64)$  and  $ACQ(16 : 64)$ . In this case, the number of emitters is limited.  $M_o$  for both cases decreases from 81% to 77% and 65%, respectively. The lateral profile for  $ACQ(32 : 64)$  (Figure 49(a)) stays in a similar range compared to  $FMC$ , with a small increase in the mean value, but with a smaller variance. Figure 49(b) shows the acoustic response for  $ACQ(16 : 64)$  strategy, whose sidelobes rise above the  $FMC$  response and, comparing with  $ACQ(64 : 16)$ , which has similar number of used signals, it has worse response (Figure 47 (b)).

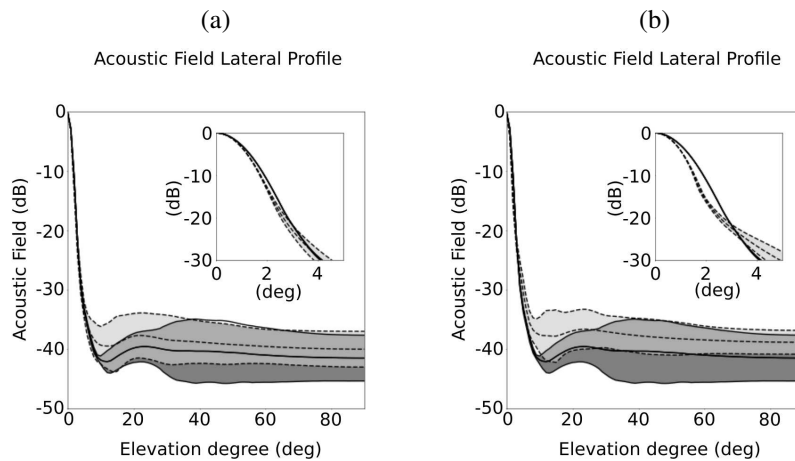
Consequently, one important conclusion is that limiting the number of emitters has more consequences in the acquisition strategy than limiting the number of receiving parallel channels. When one emission element is removed from the acquisition, instead of turning off only one position of the acquisition matrix, it will turn off a full line in the acquisition matrix. In consequence, there is less space for optimisation. On the other side, when the number of emissions

Figure 48 – *ACQ* obtained from (a) the setting (32 : 64) and (b) the setting (16 : 64) .



Source: Author

Figure 49 – Sidelobes distribution at each elevation angle for strategies (a) (32 : 64) and (b) (16 : 64) (light grey area within the dashed line) and the *FMC* (dark grey area within the solid line).



Source: Author

decreases, the imaging frame rate increases.

In our examples, the original dynamic range is maintained when the number of resultant signals is higher than 25%. The only difference is from 10° to 20°, where the amplitudes generated by the *FMC* are considerably lower. When the reduction is more intense, the side lobes' intensities increase. In the case of the lateral resolution ( $\Delta\theta_{-6dB}$ ), all of the strategies offer higher values than the *FMC* until the crossing point (up to -20 dB). From this value, the lateral resolution is higher for the *FMC*. This behaviour is a consequence of the smoother shape of the coarray when the reduction is applied.

## 4.3.2 Segmented annular array - simulated and experimental results

### 4.3.2.1 Experimental setup

The experimental example is based on the segmented annular array described in (MARTÍNEZ et al., 2003). The array prototype is illustrated in Figure 50(a) and was manufactured at CSIC laboratory. It has been designed for nondestructive testing of metallic parts, but in work, it is operating in water Figure 50(b). The array ( $f_c = 1.5$  MHz,  $BW = 20\%$ ) is composed of 64 elements that are organised in three rings, has a 20 mm diameter (in water  $20\lambda$ ), the center of the elements are spaced by 2 mm (in water  $2\lambda$ ) and element size is  $1.5 \times 1.5$  mm (in water  $1.5\lambda$ ).

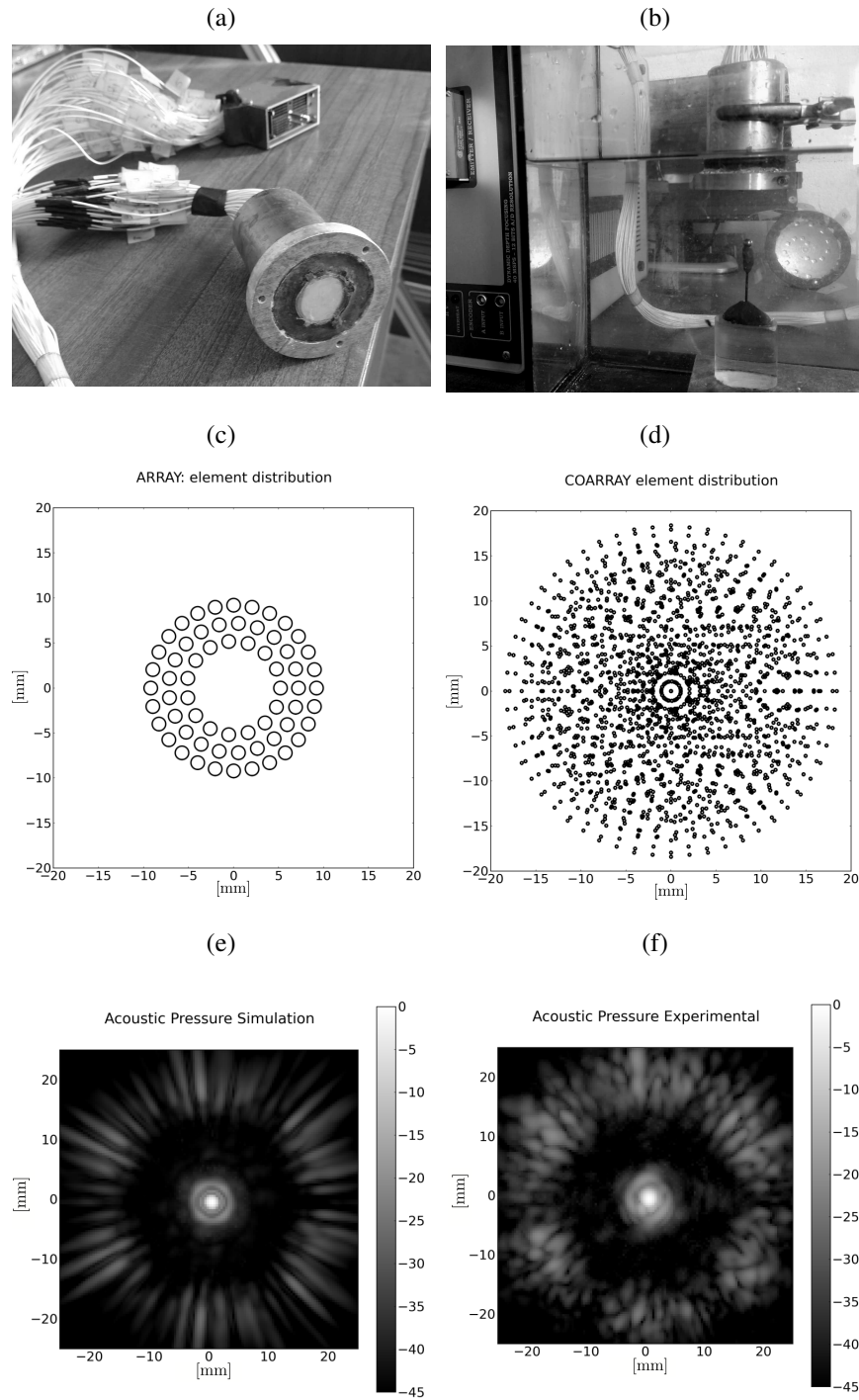
Figure 50(c) illustrates the segmented annular array element distribution and (d) is the corresponding coarray. In order to obtain a more accurate response in our simulation model, the differences in the energy radiated per element and the element radiation pattern were taken into account. Comparison between experimental data and simulations are based on images from a spherical reflector. Figure 50(e) shows a simulated image of a point reflector and Figure 50(f) illustrates the experimental image, both set at  $Z = 40$  mm,  $X = [-25 : 25]$  mm and  $X = [-25 : 25]$  mm and using the *FMC* and *TFM*. With this configuration, in water, experimental results show a lateral resolution of  $5^\circ$  and a dynamic range, limited by grating lobes at  $30^\circ$ , of 20 dB. The differences between simulated and experimental images are due to anomalies in the radiation pattern of the real aperture and the diffraction response of the reflecting sphere. Furthermore, this probe shows significant variations in element-to-element sensitivities, reaching up to 4 dB, which increases the sidelobes level intensities.

### 4.3.2.2 Synthetic aperture strategies

After clustering the coarray elements, 109 signals meet the  $\lambda/32$  condition. The *CPG* matrix has 10,542 positions ( $N_p = 251$  and  $N_g = 42$ ) fills 66% ( $M_o$ ) with a  $M_r = 5.45$ . The *RCP* configuration works as illustrated in Figure 41. The configurations designed for this example are: *ACQ*(64 : 64), *ACQ*(64 : 24), *ACQ*(64 : 16) and *ACQ*(64 : 8). Figure 51 illustrates the acquisition strategies: the acquisition matrix, simulated and experimental images of a point/spherical reflector, and a detail of the lateral profile of the maximum beampattern (simulated and experimental). Table 8 summarises several parameters used to evaluate the performance of each strategy.

The *ACQ*(64 : 64) and *ACQ*(64 : 24) strategies solutions show similar beampatterns, where the sidelobes remained at -30 dB level. For the *ACQ*(64 : 16) and *ACQ*(64 : 8) strategies, there was an increase of the sidelobes of 5 dB and 10 dB, respectively. We notice that the model predicts the impact of  $M_o$  reduction, which increases the sidelobes level (STEINBERG, 1976). Meanwhile, grating lobes, around  $28^\circ$ , kept at approximately the same level for all strategies, with a slight increase when  $M_o$  is reduced. Mainlobe width is also maintained for all strategies,

Figure 50 – Segmented annular array. (a) Array prototype; (b) experimental setup in water, array faced downwards and a 3 mm-diameter spherical reflector placed 40 mm from the array; (c) element distribution, (d) coarray footprint. Image of a (e) point reflector (simulated) and (f) 3 mm-diameter metallic sphere (experimental) both placed at  $[X=-25 : 25 \text{ mm}, Y=-25 : 25 \text{ mm}, Z=40 \text{ mm}]$ .



Source: Author

Table 8 – Segmented Annular Array. Performance for the (64 : 64), (64 : 24), (64 : 16) and (64 : 8) settings. Simulated and experimental data included for  $\Delta\theta_{-6dB}$ , DR (dB) and  $\Delta\theta_{DR}$ .

$ACQ$	$M_o$	$M_r$	$N_s$	$N_c$	$\Delta\theta_{-6dB}$		$DR$ (dB)		$\Delta\theta_{DR}$	
					Sim.	Exp.	Sim.	Exp.	Sim.	Exp.
(64 : 64)	66%	1.8	1536	29	2.80°	3.17°	-20.86	-18.91	6.40°	6.96°
(64 : 24)	60%	1.5	1286	24	2.81°	3.20°	-20.51	-18.59	6.21°	6.38°
(64 : 16)	52%	1.3	1024	16	2.82°	3.21°	-20.79	-17.41	6.40°	6.70°
(64 : 8)	35%	1.2	512	8	2.71°	3.10°	-20.59	-18.12	6.73°	10.02°

as observed from  $\Delta\theta_{-6dB}$  and  $DR$  (dB) from table 8.

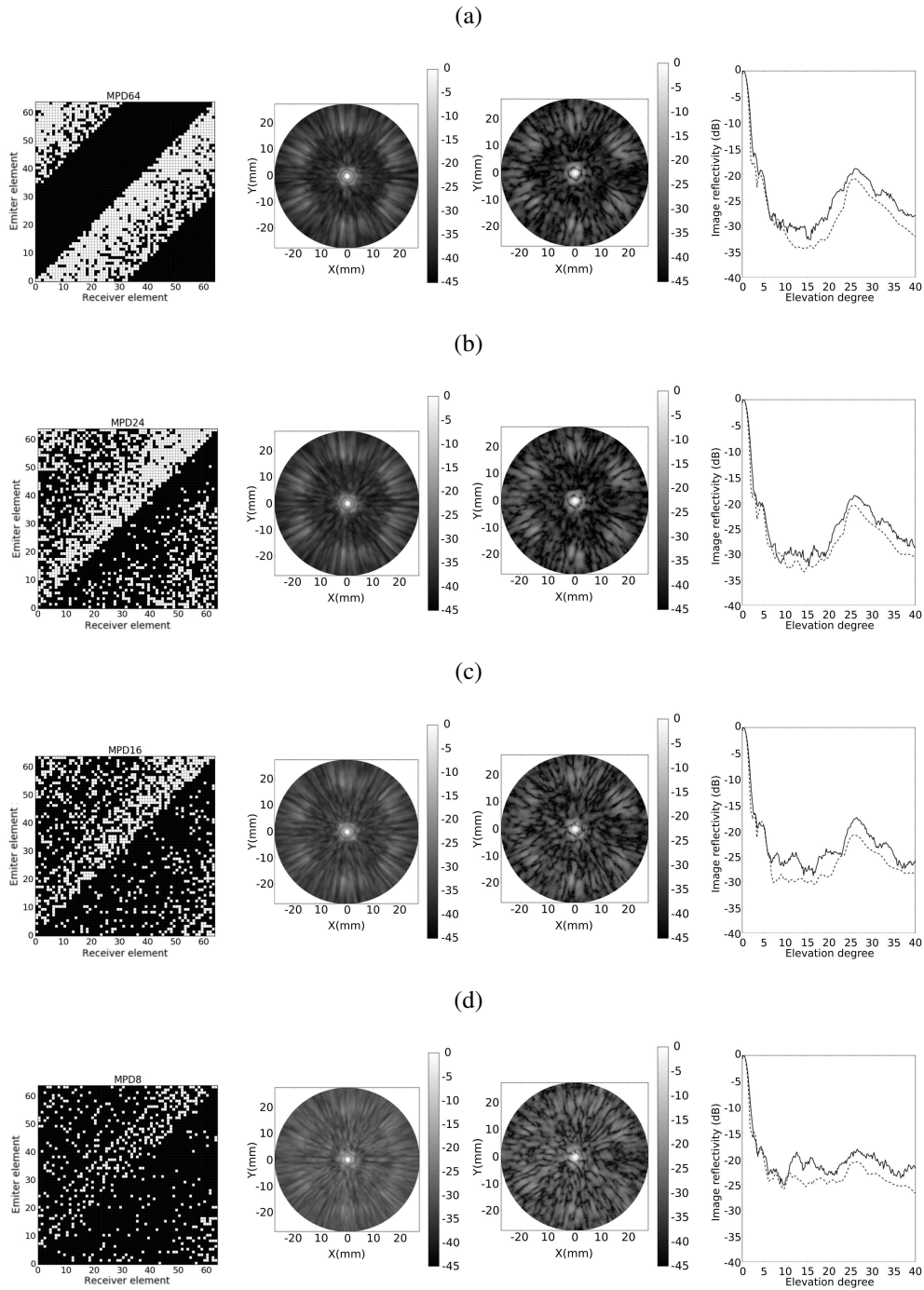
Regarding the resource optimisation, when compared to the  $ACQ(64 : 64)$ , the  $ACQ(64 : 24)$  has a 6% reduction in  $M_o$ , reducing the parallel channels ( $N_c$ ) in five, and the number of selected signals ( $N_s$ ) by 250. A significant signal reduction (512) is achieved while  $M_o$  is maintained above 50%, from  $ACQ(64 : 64)$  to  $ACQ(64 : 16)$ . The  $ACQ(64 : 8)$  produces a significant reduction in the value of  $M_o$  (35%), but the secondary lobes increase to the level of the grating lobes, as can be noticed in Figure 51(d). There are no dramatic changes in dynamic range ( $DR$ ) because the array structure is maintained, and is limited by the grating lobes.

#### 4.4 DISCUSSION

The design of a synthetic aperture imaging system should consider a balance between the number of parallel channels, the number of signals in the beamforming, the number of shots to capture all data needed per image, and the multiplexer complexity. In this sense, synthetic imaging beamforming can exploit popular parallel computation resources to obtain 3D imaging at a relatively low cost, using multicore or GPGPU (General-Purpose Graphics Processing Units). Parallel GPGPU beamforming for 4096 signals can generate a frame rate of 66 images/s ( $265 \times 256$  pixels) (ROMERO-LAORDEN et al., 2016), being possible to generate two volumes per second ( $128 \times 128 \times 128$  voxels). Considering a maximum number of signals ( $N_s$ ) of 1024, the GPGPU beamforming can generate up to ten volumes per second. However, to support this volume rate, we need to limit the acquisition operations by reducing the number of emitters and the volume of data transferred per shot to the processing system (parallel receiver channels). Using this information, we analyse, by simulations, two strategies for the Fermat spiral array:  $ACQ(42 : 24)$  and  $ACQ(32 : 32)$ .

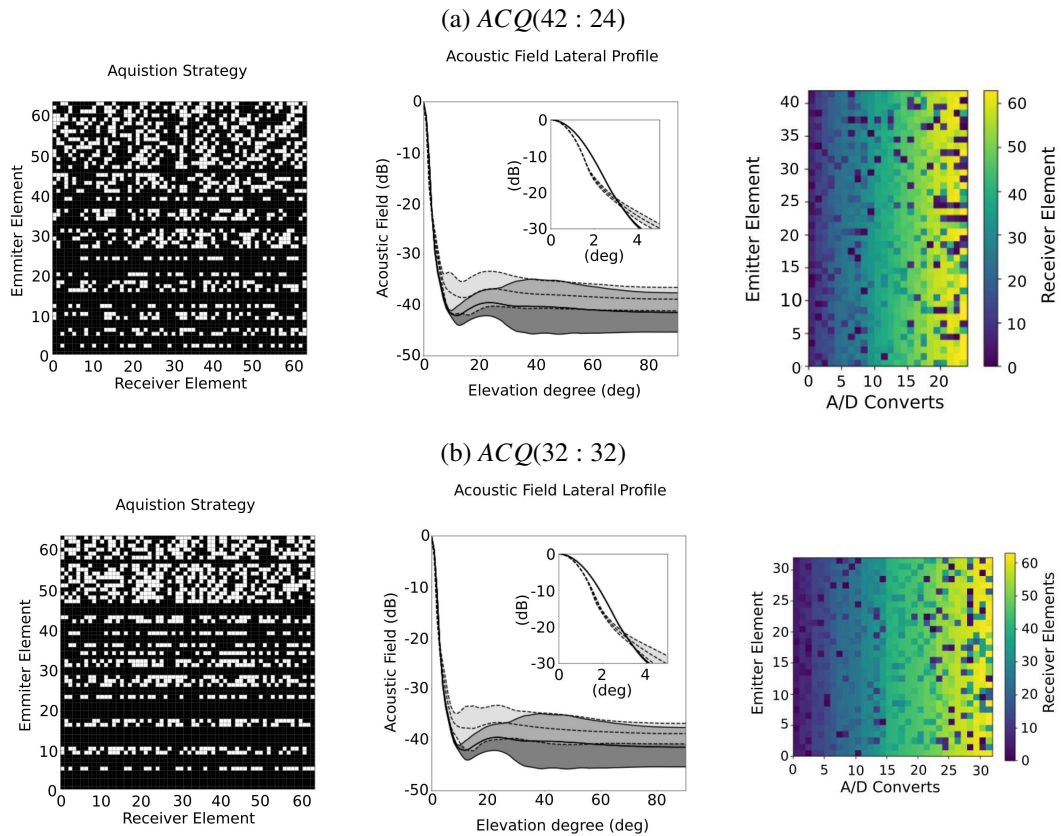
Figure 52 illustrates the two proposed acquisition strategies and shows the lateral profile of the acoustic field, where dark grey corresponds to the acoustic field of the  $FMC$ . Although the acoustic pressure is similar for the two configurations, it is possible to see that the reduction in the number of shots has a worse impact than the reduction of parallel channels in reception.

Figure 51 – Results for the segmented annular array obtained from *ACQ* (a) (64 : 64), (b) (64 : 24), (c) (64 : 16) and (d) (64 : 8), where the acquisition strategy, the simulated point reflector, the experimental metallic sphere image (cylindrical coordinates:  $Z = 40$  mm  $R = [0 : 25]$  mm,  $\theta = [0^\circ : 360^\circ]$ ), and the image reflectivity (maximum at each elevation angle) are illustrated, respectively. For the image reflectivity, the simulated response is illustrated in the dashed line and the experimental result in the solid line.



Source: Author

Figure 52 – Results obtained from *ACQ* (a) (42 : 42), and (b) (32 : 32), where the acquisition strategy is presented on the left, the sidelobe distribution at each elevation angle for strategies is illustrated at the centre, and the configuration of the multiplexer net showing, at each shot, the distribution of reception transducer in the reception channels is illustrated in the right. For the sidelobe distribution, the current *ACQ* is represented in a light grey area within the dashed line, and the *FMC* is represented as a dark grey area within the solid line.



Source: Author

The results are summarised in Table 9, where *FMC* and *RCP* are also listed. In both cases, there was a reduction in  $M_o$  from 81% to 75% and 74%, respectively. The sidelobe distribution is comparable to the *FMC*, so, in practice, the image quality is maintained in a similar range. However, the number of signals  $N_s$  is reduced to less than half when compared to *RCP* (2080 to 1008), which means a significant cost reduction in processing. Lateral resolution is also better for the proposed strategies, as can be observed from  $\Delta\theta_{-6dB}$ .

The last challenge is the design of the multiplexer net. In our example, the efficient design of the *RCP* needs up to 128 switches. However, a reduction in the number of receiver channels or/and in the number of emissions has an increment in the number of transducers that has to be attended by each receiver channel (in consecutive shots). In consequence, the multiplexer net becomes more complex. In Figure 52 the multiplexer matrix is presented for

Table 9 – Spiral array: *FMC*, *RCP*, *ACQ*(42 : 24) and *ACQ*(32 : 32) acquisition strategies results.

<i>ACQ</i>	$M_o$	$M_r$	$N_s$	$N_c$	$\Delta\theta_{-6dB}$	<i>CP</i> (dB)	<i>DR</i> (dB)	$\Delta\theta_{DR}$
<i>FMC</i>	81%	7.23	4096	64	$2.92^\circ$	-	-35	$11.5^\circ$
<i>RCP</i>	81%	3.68	2080	33	$2.92^\circ$	-	-35	$11.5^\circ$
(42 : 24)	75%	2.02	1008	24	$2.34^\circ$	-21	-33.4	$12.9^\circ$
(32 : 32)	74%	2.05	1024	32	$2.42^\circ$	-20.6	-33.11	$14^\circ$

both solutions. The configuration *ACQ*(42 : 24) needs 201 switches in reception and 42 in emission. In the case of the configuration *ACQ*(32 : 32) it needs 246 in reception and 32 in emission (see  $N_c$  in Table 9). These nets have been optimized to reduce the number of switches using an *ad-hoc* algorithm, linking transducers to specific A/D converters. In general, we can say that the reduction of parallel resources has a cost in complexity in the multiplexer.

Although the *ACQ*(42 : 24) has a significant reduction in the hardware resources (around 25%), the *ACQ*(32 : 32) is about 30% faster than *ACQ*(42 : 24). Additionally, the analysis of the beampattern, based on lateral resolution and dynamic range of both *ACQ* (see table 9), shows that they have similar behaviour.

#### 4.5 COMMENTS

In this work, we have shown, based on the concepts of the Radon transform and the equivalent linear array, how to study the coarray spatial redundancy of non-grid 2D sparse arrays like spirals or annular rings. Furthermore, we have developed a process to exploit this spatial redundancy to reduce the electronic resources and the computational cost of the beamforming operations of the synthetic aperture system. It has been shown that, with an adequate selection of signals, the resources of an imaging system can be reduced without significant degradation of the original *FMC* dynamic range. However, the reduction of redundancy makes the coarray shape smoother, which increases the lateral resolution but also increases the secondary lobes.

This procedure improves the capabilities of the system designer to control the performance of sparse arrays based on spirals and other non-grid patterns. Restrictions can be imposed, such as in the number of parallel channels and the number of emission elements. Other conditions, like eliminating specific elements, can also be applied, which could be the case due to malfunctioning transducers and, consequently, this process can be used to design fault-tolerant solutions. And finally, it can provide a measure of the aperture information quality that could be useful for the design/development of new beamforming methods based on sparse coarray reconstruction. In addition, based on the redundancy generated by the reciprocity, a generic solution with an efficient multiplexer design has also been presented.

The proposed methodology provides a solution to developing systems with low re-

sources, which can be easily embedded in complex or autonomous systems. Considering  $ACQ(64 : 16)$ , this solution uses only 16 receiver channels, 64 emitters, and one transmitter. Then, according to the standard electronic integration levels of the market, we can design a quite simple aperture that integrates the electronic front-end close to the transducer, reducing electrical noise, as well as interconnection and communication problems. This opens the possibility of developing instrumentation integrated into the internet of things systems for nondestructive testing applications.

## 5 2D SPARSE ARRAY EVALUATION

In this chapter, a new method for designing sparse bidimensional arrays based on non-grid apertures is proposed. The occupancy rate ( $M_o$ ) and redundancy level ( $M_r$ ) of the coarray projection grid (CPG) created in the previous chapter are studied to determine how these parameters influence the radiation wideband response. Then, a FF is created to evaluate non-grid apertures and the simulated annealing algorithm is used to find different sparse bidimensional arrays based on the spiral Fermat array and the segmented annular array.

### 5.1 FITNESS FUNCTION BASED ON CPG

In the previous chapter, the proposed heuristic selects different combinations of emitters and receivers to create an acquisition strategy for non-grid apertures for synthetic aperture. The heuristic finds a set of signals (emitter and receivers) that most fill a Coarray Projection Grid (CPG) with reduced redundancy. Two figures of merit are used to measure the occupancy level ( $M_o$ ) and the redundancy level ( $M_r$ ) of the CPG, where a relationship between these two features with the radiation pattern wideband response started to be constructed.

The analysis helped to understand that reducing  $M_r$  maintaining the  $M_o$  creates acquisitions that have a wideband RP with a slightly better lateral resolution, but it has higher energy intensities from 10 to 20°, compared to *FMC*. For larger angles, the side lobes intensities remained similar. These two parameters can be used to create a fitness function (FF) that is able to evaluate different non-grid sparse arrays only using spatial analysis, which removes the need to use the energy irradiated by an array or PSF.

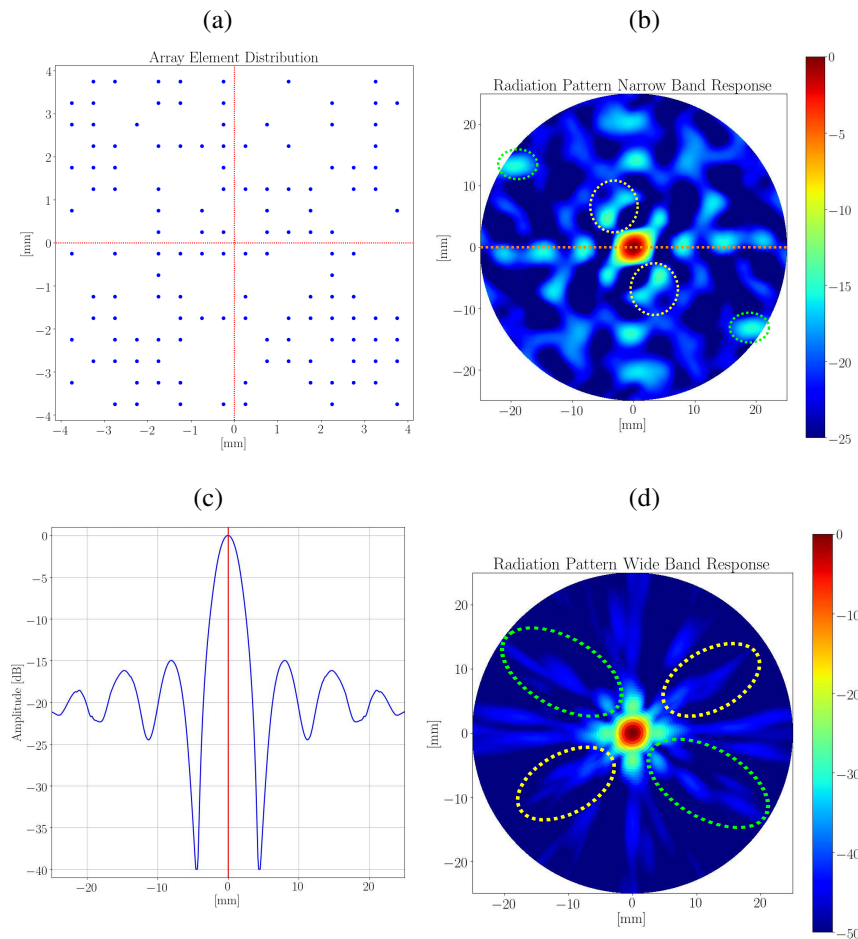
There are disadvantages of using the energy irradiated by an array to design an aperture, which justifies using the elements' position. In the narrowband response, which is a Fourier transform of the array elements position, the irradiated energy is amplified to the worse situation. The sidelobes have high amplitudes, and the grating lobes have the same magnitude as the main lobe, which turns hard to create a function that quantifies the radiation pattern. In real applications, the elements are excited with wideband pulses, different from the narrowband pulses (continuous waves) considered in this simulation method. Moreover, this response does not correctly represent the energy irradiated by asymmetrical arrays.

An asymmetrical matrix sparse array with 150 elements is illustrated in Figure 53 (a), where the radiation pattern narrowband response is illustrated in (b). Pairs of circles with matching colours are used to highlight that this response is symmetric, although the sparse array is not. Moreover, the amplitudes of this response at 0° (dashed line) are plotted in (c), where it is possible to see this symmetry at the centre. Although the array is asymmetrical, the energy response is symmetric and fails to represent the array energy.

This simulation method has this issue that does not appear with the wideband radiation

pattern response, as seen in (d), where the highlighted areas aid to see. However, in the wide-band radiation pattern response, it is required to define the ultrasonic pulse response of a single element, which can restrain the array operation to a determined centre frequency and excitation. At last, the PSF could be used as happened in chapter 3. Nevertheless, the PSFs in 2D arrays are still computationally costly to calculate. In this way, it is reasonable to use the array element's position to create a fitness function that evaluates different sparse arrays to design and find a sparse configuration with good features. To develop this FF, it is interesting to deeply analyse how ( $M_o$ ) and ( $M_r$ ) are linked to the radiation pattern response to give an idea to combine these two parameters.

Figure 53 – (a) Asymmetrical matrix sparse array, (b) Radiation Pattern narrowband response, (c) Line extracted at  $0^\circ$  of the narrowband response and (d) Radiation Pattern wide-band Response with the amplitudes extracted at  $0^\circ$ .



Source: Author

### 5.1.1 $M_o$ and $M_r$ analysis

The Fermat spiral array is a non-grid array where a good element distribution is achieved (MARTÍNEZ-GRAULLERA et al., 2010). The elements are distributed following (43), where

$\alpha$  is the divergence angle, and  $\varphi$  is the initial phase used to create different emitter and receiver apertures.

$$\vec{e}_i = (R_0 i \cos(\alpha i + \varphi), R_0 i \sin(\alpha i + \varphi)), \quad \forall \quad i = 1, \dots, N, \quad (43)$$

where  $R_0$  is defined as:

$$R_0 = \frac{D}{2 \sqrt{N \alpha}}, \quad (44)$$

where  $D$  is the aperture dimension and  $N$  is the number of elements in the array.

To analyse  $M_o$  and  $M_r$ , different sparse arrays were created by selecting a different number of elements emitting and receiving from a Fermat-based spiral array with 360 elements, where the divergence angle  $\alpha$  is  $160.875^\circ$  and  $\varphi$  is  $0^\circ$ . The spiral array with  $40\lambda$  its illustrated in Figure 54, where its radiation pattern is illustrated in (b). This array is also expanded to a  $60\lambda$  diameter, where the energy irradiated by the array is illustrated in (c).

Figure 54 (d) is the lateral profile of both radiations, where the blue continuous lines correspond to the  $40\lambda$  diameter array, and the red dashed lines correspond to  $60\lambda$  diameter. It is possible to see that the lateral energy remained almost at the same level for both arrays, and the main lobe is narrower in the wider array. For the radiation pattern simulations, the centre frequency of the ultrasonic pulse simulated was defined as  $f_c = 1.5$  MHz, operating in water ( $c = 1500$  m/s), sample frequency  $f_s = 40$  MHz and  $BW = 0.6$ .

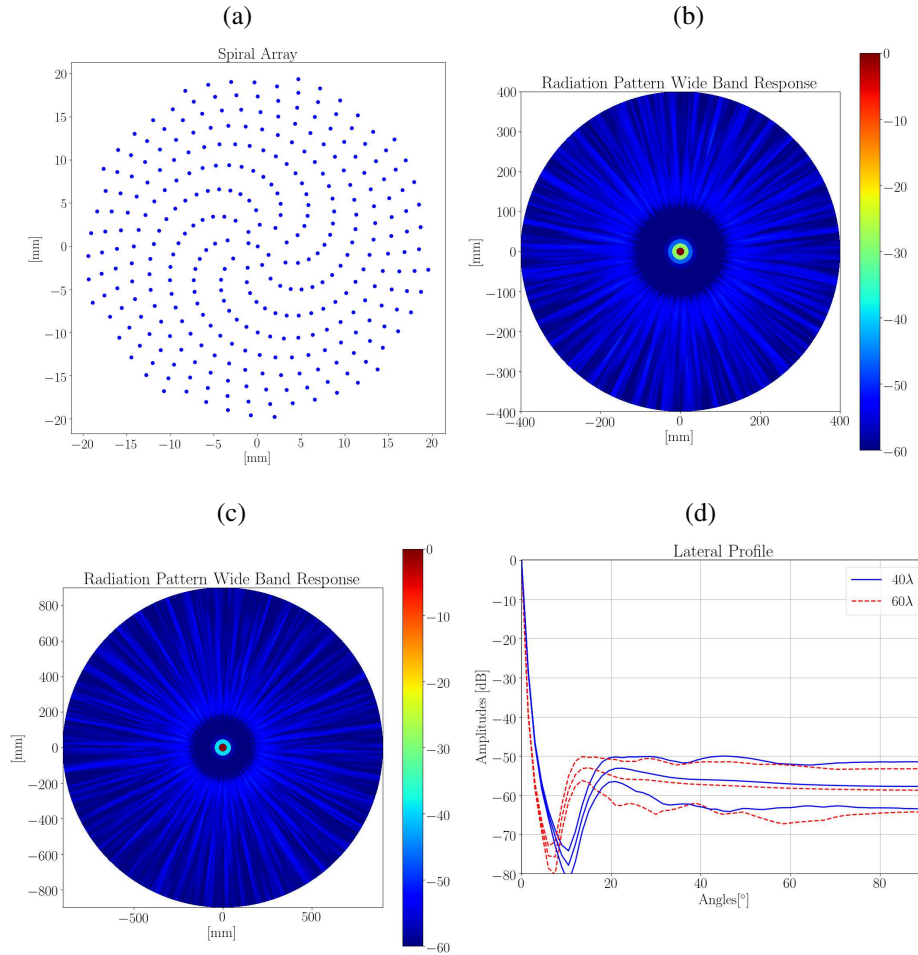
The  $40\lambda$  spiral array with 360 elements has an  $M_o$  of 0.93 and  $M_r$  of 84.94. The  $60\lambda$  spiral has an  $M_o$  of 0.92 and  $M_r$  of 56.61. These 360 spiral arrays will be used as an array model where different numbers of emitters and receivers are selected.

For the  $40\lambda$  array, different apertures were created by selecting 128 and 192 elements, where half of the elements (64 and 96) work as emitters and the other half as receivers. For the  $60\lambda$  array, 256 elements were selected, where 128 are emitters and 128 are receivers. The arrays were named  $128/40\lambda$   $192/40\lambda$ , and  $256/60\lambda$ . Table (10) gives the information about the selected apertures. Three cases were selected for each setting aiming apertures with high  $M_o$ , high  $M_r$  and a more balanced  $M_o$  and  $M_r$ .

In Figure 55, three radiation patterns of configurations 1, 2 and 3 of setting  $128/40\lambda$  in Table (10) are illustrated. The first configuration, illustrated in Figure 55(a), has a high  $M_o$ . The amplitudes aside the main lobe decline to about -25 dB at the first stage and then to -35 dB. In configuration-2, where the radiation pattern is illustrated in (b), the  $M_r$  is higher, but  $M_o$  is lower than the configuration-1. The amplitudes aside the main lobe at the first stage are higher than Figure 55(a) staying about -18 dB, but it declines faster to about -45 dB.

Figure 56(a) illustrates the lateral profile of the two configurations analysed (1 and 2). It is possible to see that, at first, configuration-1 has lower amplitudes (see I), but afterwards,

Figure 54 – (a) 360 Elements Fermat Spiral Array with  $40 \lambda$  diameter ( $\lambda = 1 \text{ mm}$ ) and  $\alpha = 160.875^\circ$ . (b) the radiation pattern of the spiral array. (c) the radiation pattern of the spiral array with the same setting, but elements placed in a  $60 \lambda$  diameter. (d) the lateral profile of the two radiation patterns.



Source: Author

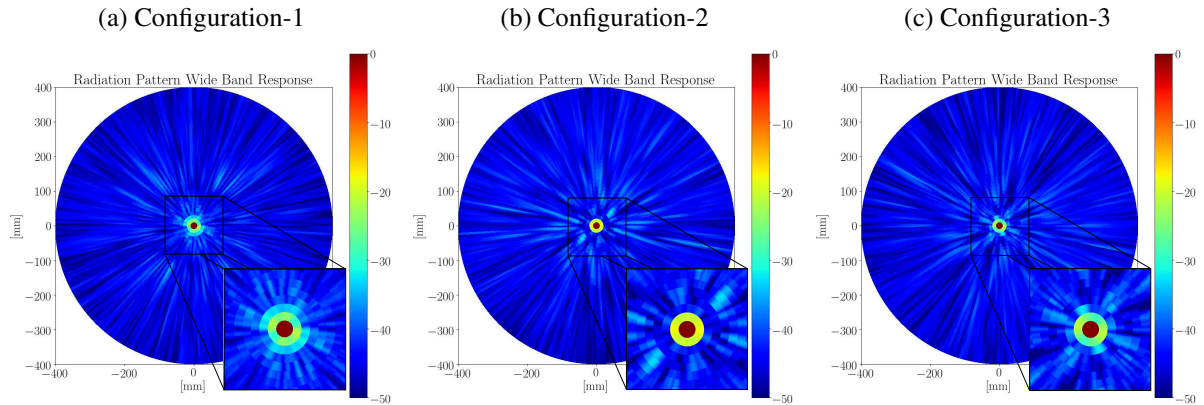
Table 10 –  $M_o$  and  $M_r$  results of different configurations

Settings	Configuration	$M_o$	$M_r$
128/40λ	1	0.84	4.08
	2	0.66	5.00
	3	0.71	4.69
192/40λ	1	0.91	10.42
	2	0.66	13.63
	3	0.77	12.85
256/60λ	1	0.90	12.90
	2	0.78	15.08
	3	0.88	13.01

there is a crossing point where the amplitudes of configuration-2 decrease faster and have lower amplitudes (see II).

The rapid decrease in the amplitudes in configuration-2 compared to configuration-1

Figure 55 – Radiation pattern wideband response of the three sparse arrays with 64 elements emitting and 64 elements receiving with  $40\lambda$  diameter, where the  $M_o$  and  $M_r$  information are given in Table (10). (a), (b) and (c) are generated using configurations 1, 2 and 3, respectively.



Source: Author

is a consequence of higher  $M_r$ . It is a desired feature in ultrasonic images as it means that the amplitudes besides the reflector imaged will rapidly decrease, which increases the image contrast. The  $M_0$  is lower in configuration-2, which has wider main lobe width that translates to worse lateral resolution than configuration-1.

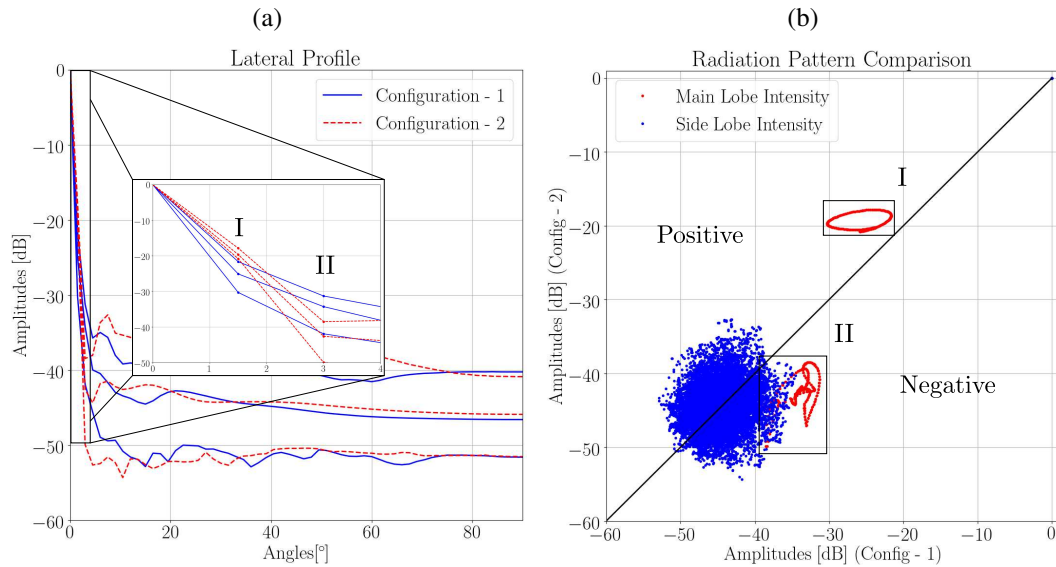
It is subjective and hard to see the difference between the side lobe distribution by looking at the lateral distribution. One strategy developed in this chapter compares pixel by pixel two radiations patterns and extracts statistical information about the distribution of pixels. For example, in one pixel of the RP of configuration-1, the amplitude is -45 dB. In the same pixel in the RP of configuration-2, the amplitude is higher at -35 dB. These two values are combined to create a coordinate (-45,-35) that is plotted in a Cartesian plane.

Figure 56(b) illustrates these amplitudes distribution comparing the RPs pixel by pixel. The amplitudes in red represent the main lobe intensities, which are the first and second points besides the maximum intensity (0 dB). In blue, the amplitudes correspond to the side lobes. The amplitudes corresponding to the x-axis are generated using configuration-1 and, on the y-axis, the amplitudes corresponding to configuration-2. A line ( $f(x) = x$ ) is also illustrated in black and helps to analyse the amplitudes distributions.

The regions I and II highlighted in the lateral profile in (a) are illustrated in (b). It is possible to see in (b) that the amplitudes corresponding to I appear above the black line, which are referred to as positive values. In region II, it is possible to see that the amplitudes are located below the black line in the negative region.

Two values are extracted from this amplitude distribution. The first, is the percentage distribution, which is the percentage number of elements in the negative and positive regions using the black line as reference. For example, using only the amplitudes in region-I in Fi-

Figure 56 – (a) lateral profile of configuration 1 and 2 of  $128/40\lambda$  and (b) the radiation pattern comparison.



Source: Author

Figure 56(b), 100% of the points are in the positive region, which means that for this area analysed, the radiation pattern generated using configuration-1 has lower amplitudes compared to the RP generated using configuration-2. In region II, all amplitudes are in the negative area (100% in negative). If regions I and II are analysed together, 50% of the points are in the positive, and 50% in the negative area.

The other parameter is the mean of the distances from the points (x,y coordinates) to their projection in the black line. This parameter indicates the dominance of one radiation pattern over the other. For example, in the main lobe analysis, considering the region I and II, the percentage distribution is 50/50 %, and the means are -5.90/4.04. The value -5.90 indicates the mean distance of the negatives points to its projections in the black line. This higher mean value for the negative points, compared to the positive mean, indicates that when the amplitudes of RP configuration-2 are lower than the amplitudes of RP configuration-1, the difference between them is higher than when the amplitudes of RP configuration-1 are lower than the amplitudes of RP configuration-2. These two parameters help to compare two radiation patterns in lateral resolution and side lobes intensities.

Two values are extracted from this amplitude distribution. First, is the percentage distribution, which is the percentage number of elements in the negative and positive regions using the black line as reference. For example, using only the amplitudes in region-I in Figure 56(b), 100% of the points are in the positive region, which means that for this area analysed, the radiation pattern generated using configuration-1 has lower amplitudes compared to the RP generated using configuration-2. In region II, all amplitudes are in the negative area (100% in negative). If regions I and II are analysed together, 50% of the points are in the positive, and

50% in the negative area.

The other parameter is the mean of the distances from the points (x,y coordinates) to their projection in the black line. This parameter indicates the dominance of one radiation pattern over the other. For example, in the main lobe analysis, considering the region I and II, the percentage distribution is 50/50 %, and the means are -5.90/4.04. The -5.90 indicates the mean distance of the negatives points to its projections in the black line. This higher mean value for the negative points, compared to the positive mean, indicates that when the amplitudes of RP configuration-2 are lower than the amplitudes of RP configuration-1, the difference between them is higher than when the amplitudes of RP configuration-1 are lower than the amplitudes of RP configuration-2. These two parameters help to compare two radiation patterns in lateral resolution and side lobes intensities.

In Table 11, the percentage distribution and mean for the main lobe and side lobes are given for all combinations of the configurations in Table 10. In the "combination" column, the first number corresponds to the image on the x-axis, linked to the negative percentage and mean. The second number corresponds to the image on the y-axis, related to the positive percentage distribution and mean. The higher the percentage or mean, the worse one RP is compared to the other. These two tables will help to understand how  $M_o$  and  $M_r$  are linked to the radiation pattern and create a mathematical function that evaluates sparse apertures.

Table 11 – Main Lobe and Side Lobe distribution analysis for the spiral array with 40 and 60  $\lambda$ .

Settings	Combination	Main Lobe Information		Side Lobe Information	
		Neg/Pos (%)	Mean	Neg/Pos (%)	Mean
128/40 $\lambda$	1-2	50/50	-5.90/4.04	45/55	-1.76/1.97
	1-3	57/43	-3.45/1.40	46/54	-1.83/1.91
	2-3	56/44	-3.41/3.41	54/46	-1.90/1.88
192/40 $\lambda$	1-2	50/50	-6.04/6.51	39/61	-1.97/2.40
	1-3	51/49	-7.94/3.13	43/56	-1.81/2.10
	2-3	91/09	-2.98/0.56	53/47	-1.90/1.88
256/60 $\lambda$	1-2	50/50	-7.18/4.32	46/54	-1.96/1.97
	1-3	65/35	-1.19/1.76	50/50	-1.58/1.66
	2-3	50/50	-6.83/3.66	55/45	-1.83/1.88

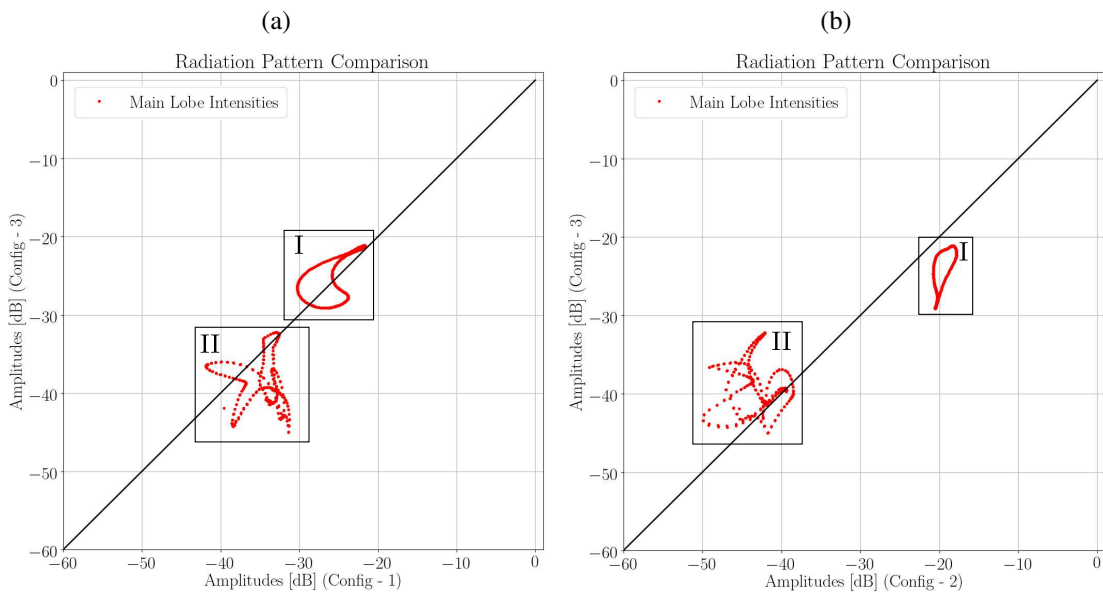
The first result is the radiation pattern combination of configurations 1 and 2. For the main lobe, the percentage distribution remained equal for the two radiations, where the mean is higher for the negative part. For the side lobes amplitudes, configuration-2 generates a radiation pattern with higher amplitudes compared to configuration-1, which can be concluded from the higher percentage distribution and mean. This is due to the lower  $M_o$  of configuration-2, which has more grating lobes interference that increases the side lobes intensities in the radiation pattern response.

Configuration 1 and 2 of 128/40 $\lambda$  are two extremes of the  $M_o$  and  $M_r$  values. Both have their qualities, Configuration-1 has a RP with lower sidelobes intensities, and in configuration-

2, the amplitudes rapidly decrease besides the main amplitude. Configuration-3 is the balance of  $M_o$  and  $M_r$  that tries to have both qualities of configurations 1 and 2. By looking at Table 11, configuration-3 generates an RP with a better main lobe compared to configurations 1 and 2, where the percentage is higher for the negative area in both combinations (57% and 56%, respectively). The mean is higher for configuration-1 (-3.45 over 1.40) and the same for configuration-2 (3.41).

When compared to configuration-1, the configuration-3 response has, in some areas, lower amplitudes right aside the main lobe, which is illustrated as region I in Figure 57(a) and a rapid decrease in the main lobe intensities, highlighted in region II. However, the side lobes are higher in configuration-3 as the percentage in the positive area is 54%. When compared with the configuration-2 response (Figure 57(b)), configuration-3 has lower amplitudes right next the maximum point (region I) and declines slower than the configuration-2 response, but in some areas configuration-3 response has lower amplitudes (region II). The side lobe amplitudes of configuration-3 are lower as the percentage is 46% for the positive region.

Figure 57 – Radiation Pattern comparison, only the main lobe analysis. (a) Combination 1-3 (b) Combination 2-3.



Source: Author

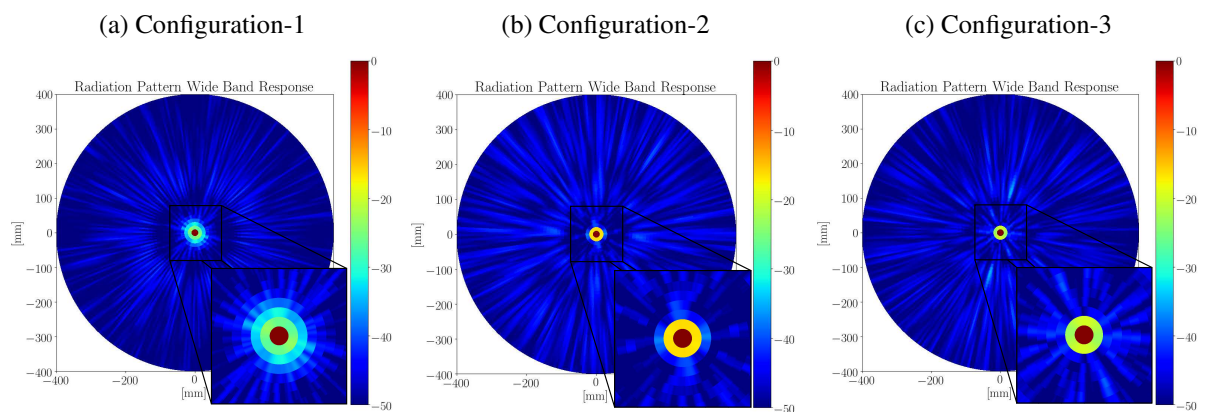
The radiation pattern of configuration-3 is a mixture of characteristics of configuration 1 and 2 radiation pattern responses. It seems that apertures with an equilibrium of  $M_o$  and  $M_r$  will have a radiation pattern with a balance between the main lobe and side lobe intensities. To check if this trend occurs, the same analysis was done for the apertures with  $192/40\lambda$  and  $265/60\lambda$  elements.

For the  $192/40\lambda$ , configuration-1 has a high  $M_o$ , configuration-2 a high  $M_r$  and configuration-3 a balance between these two parameters. The radiation pattern of these configurations

are illustrated in Figure 58 where (a), (b) and (c) are generated using the configuration 1, 2 and 3, respectively. The configuration-1, with the highest  $M_o$ , has the lowest amplitude aside the maximum amplitude, but the amplitudes decay slower than the RP of configuration-2 illustrated in (b). This behaviour is similar to configurations 1 and 2 of  $128/40\lambda$  analysis. The higher  $M_o$ , the lower the amplitudes next the maximum amplitude, but with a slow decline. The higher  $M_r$ , the faster the amplitudes will decline, but the amplitudes right next the maximum increase.

The side lobe distribution is worse in the RP generated using configuration-2, where 61% of the amplitudes in this RP are higher than the generated using configuration-1. Configuration-3 try to balance these two parameters. Comparing configurations 2 to 3, in Figure 58(c), the amplitudes aside the maximum are 91% lower than in (b), and the amplitudes rapidly decay. The sidelobe distribution is worse than in (a), with 56% of the amplitudes higher in configuration 3, but better than in (b), with 53% of the amplitudes higher in configuration 2.

Figure 58 – Radiation pattern wideband response of the three sparse arrays with 96 elements emitting and 96 elements receiving with  $40\lambda$  diameter, where the  $M_o$  and  $M_r$  information are given in Table (10). (a), (b) and (c) are generated using configurations 1, 2 and 3, respectively.

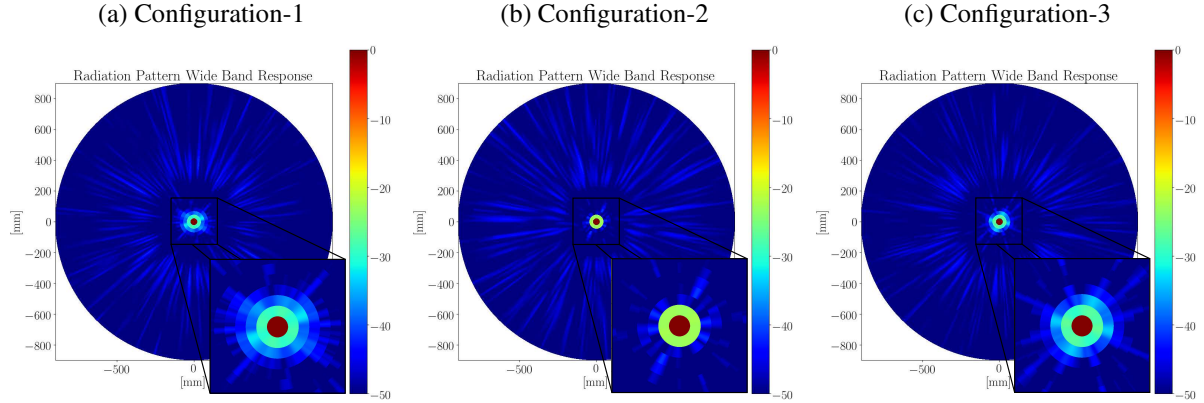


Source: Author

For the  $256/60\lambda$  apertures, the first configuration has a high  $M_o$ . The radiation pattern of this aperture, illustrated in Figure 59(a), shows the same characteristics as the apertures with high  $M_o$ . The same happens to the aperture with high  $M_r$  (configuration-2), where the radiation pattern illustrated in (b) has higher amplitudes next the maximum point, but rapidly declines. The side lobes are 54% lower for the radiation pattern in (a).

The configuration-3 radiation pattern is illustrated in (c) where the  $M_o$  is slightly lower than configuration-1 (0.88 and 0.90) and  $M_r$  is slightly higher (13.01 compared to 12.90). When the main lobe is analysed, 65% of the amplitudes are lower for the radiation pattern generated by configuration-3, and the side lobes have the same proportional distribution. Compared to the configuration-2 radiation pattern, the main lobe distribution is equally distributed because the closest to the maximum amplitudes are lower in configuration 3, but it has a slowing decay

Figure 59 – Radiation pattern wideband response of the three sparse arrays with 128 elements emitting and 128 elements receiving with  $60\lambda$  diameter, where the  $M_o$  and  $M_r$  information are given in Table (10). (a), (b) and (c) are generated using configurations 1, 2 and 3, respectively.



Source: Author

characteristic. This is the same situation that happened when configurations 1 and 2 of  $128/40\lambda$  were compared, where region I is higher for one RP and region II higher for the other.

Apertures with a balanced  $M_o$  and  $M_r$  appear to have adequate radiation pattern responses. A high  $M_o$  assures an energy reduction caused by the grating lobes' interference and helps to increase the lateral resolution. A high value of  $M_r$  helps to create the main lobe in the radiation pattern with a rapid magnitude decrease.

It is desirable an aperture with high  $M_o$  and  $M_r$ . However, in this case where the elements are selected from an aperture, these two figures of merit are inversely proportional. When the elements in the array are selected to maximize  $M_o$ ,  $M_r$  decreases, and vice-versa. It is desirable to create a mathematical function that considers these two parameters. This function needs to balance the importance of these two parameters, and one way to create this balance is by multiplying these two parameters. In this way, the proposed function created in this work is given as:

$$FF = M_o^{(k_1)} M_r^{(k_2)}, \quad (45)$$

where  $k_1$  and  $k_2$  are arbitrary weights used to give more importance in higher  $M_o$  or higher  $M_r$  but will be set to 1 in this work.

This FF evaluates the non-grid apertures considering the  $M_o$  and  $M_r$  parameters. The idea is to use this function with an optimization algorithm to find sparse apertures that generate images with high lateral resolution and low artefact intensity. In this way, an optimization problem is set where elements from the 360 spiral array are selected to maximize the FF given in (45).

## 5.2 PROBLEM FORMULATION AND SEARCH ALGORITHM

The problem is formulated as a binary optimization problem where a solution with ones and zeros indicates if an element of the 360 elements spiral array model is selected or not. The optimization problem is defined as:

$$\begin{aligned}
 & \max_{AR_e, AR_r} M_o M_r \\
 & \text{s.t. } \quad \text{sum}(AR_e) = N \\
 & \quad \quad \text{sum}(AR_r) = N \\
 & \quad \quad AR_e \in [0, 1] \\
 & \quad \quad AR_r \in [0, 1],
 \end{aligned} \tag{46}$$

where  $AR_e$  and  $AR_r$  are two binary vectors that corresponds to an emitter array ( $AR_e$ ) and a receiver array ( $AR_r$ ). The fitness function defined in (45) evaluates the solution, and the binary solutions have a constraint in the number of elements selected subject to (s.t) a value  $N$ , which is a number defined at the beginning of a search.

The optimization method selected to solve this problem is the stochastic algorithm Simulated Annealing. This algorithm is based on the annealing process, which consists of heating an object to an extreme temperature and slowly cooling it to alter the physical properties of a material. The algorithm mimics this behaviour considering that the object is a current solution, and the temperature is the probability of a worse solution being updated as the current solution. Initially, the algorithm has a high probability of a worse solution being accepted as a current solution, mimicking the cooling process. This helps to increase diversification and prevents the search algorithm to stay at a local optimum (KIRKPATRICK et al., 1983).

The Simulated Annealing is presented in the Algorithm 3. First, initial parameters such as the final cooling temperature are defined. Then, the algorithm generates an initial solution as a starting point to find better solutions and calculate its FF. In the loop stage, a new solution is generated and evaluated. If this new solution is better than the current solution, the current solution is updated. Moreover, if this new current solution is better than the best solution, this solution is updated.

If the new solution is worse than the current solution, a neighbour of the FF solutions is calculated so it can be used in a probabilistic acceptance criterion to update the current solution with this worse new solution. This probabilistic acceptance criterion is calculated in the if clause in line 13.  $T_k$  is the cooling factor that mimics the annealing principle. As the iterations increase, the probability of accepting a new solution that is worse than the current solution decreases. In this way, the algorithm starts with a high chance of accepting worse results that help to explore the search space and diversify the search. If this worse new result is not accepted, a counter increments at the point where temperature  $T_k$  and  $N_k$  are updated.

---

**Algorithm 3** Simulated Annealing
 

---

```

1: Define Initial Parameters
2: Generate First Solution
3: Evaluate the Solution
4: While(Stop_Criteria( $T_k$ )):
5:   Generate a new Solution
6:   Evaluate the new Solution
7:   if( $FF_{NewSolution} > FF_{CurrentSolution}$ ):
8:     Update the solution:
9:     if(CurrentSolution > BestSolution):
10:      Update the Best Solution:
11:   else:
12:      $dif = FF_{NewSolution} - FF_{CurrentSolution}$ 
13:     if( $e^{-dif/T_k} > \text{RandomNumber}(0 \text{ to } 1)$ ):
14:       Update the solution:
15:     else:
16:        $i = i + 1$ 
17:   if  $i > N_k$ 
18:      $T_k = \beta T_k$ 
19:      $N_k = \rho N_k$ 

```

---

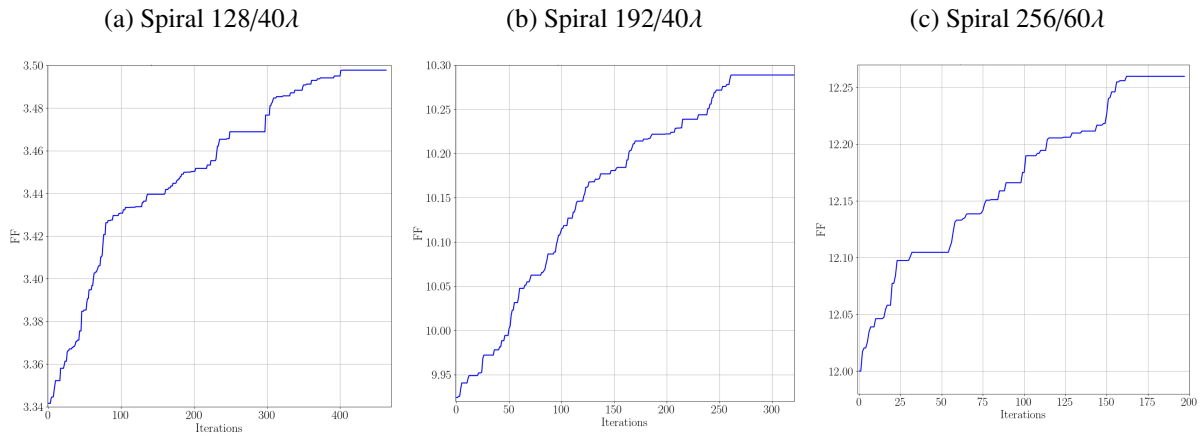
### 5.3 FERMAT SPIRAL OPTIMIZATION

The optimization strategy works by selecting emitters and receivers elements of the 360 array model, which creates a binary search problem. The solution has 720 positions, 360 for the emission elements (first half) and 360 in reception. When the value in one, the corresponding element in the 360 arrays is selected to work. Four parameters need to be arbitrarily defined, which is the case of  $\beta$ ,  $\rho$ ,  $N_k$  and  $T_k$ .  $\beta$  is the cooling factor of the algorithm, which is 0.15,  $\rho$  is the changing factor set to 5,  $N_k$  is initially 10, and  $T_k$  is 90.

The simulated annealing requires creating a function that generates new solutions. The function implemented in this work randomly swaps a position that is 1 to a place that is 0. It is equivalent to randomly turning off one element in the array and selecting another. The algorithm was used to find three apertures: 128, 192 and 256, which is the number of elements and size studied during the FF design.

Figure 60 illustrates the current best result found by the algorithm during the optimization phase. In (a), the 128/40 $\lambda$  aperture, in (b), the 192/40 $\lambda$  aperture and, in (c), the 256/60 $\lambda$  aperture. As the number of elements in the array increases, the optimization converges faster with fewer iterations.

Table 14 gives the  $M_o$ ,  $M_r$  and their multiplication (FF) for the configurations 1, 2 and 3 and the optimized aperture for their respective settings. The  $M_o M_r$  results are the highest for the optimized apertures, and it is possible to see a balance between  $M_o$  and  $M_r$  in these optimized apertures.

Figure 60 – Optimization convergence. (a) 128/40 $\lambda$ , (b) 192/40 $\lambda$  and (c) 256/60 $\lambda$ .

Source: Author

Table 12 –  $M_o$ ,  $M_r$  and  $M_oM_r$  of different configurations with different settings and their optimized aperture.

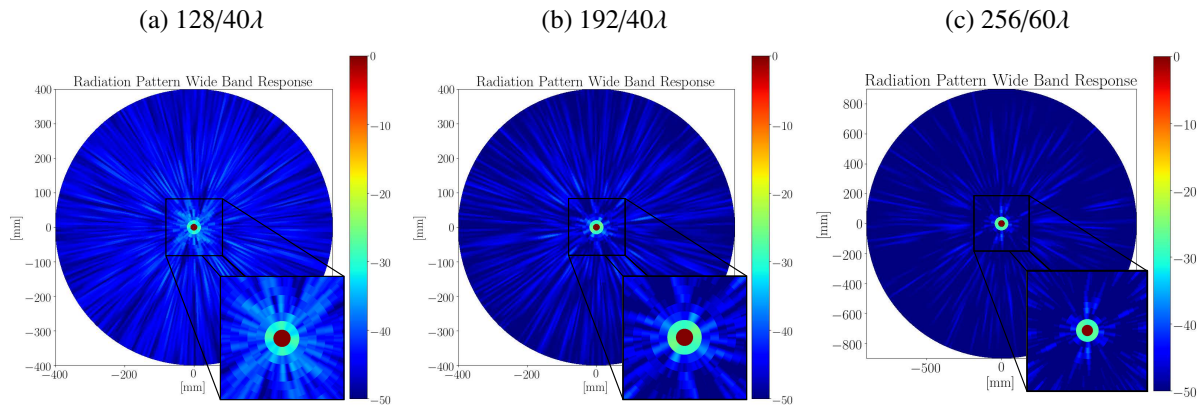
Settings	Configuration	$M_o$	$M_r$	$M_oM_r$
128/40 $\lambda$	1	0.84	4.08	3.42
	2	0.66	5.00	3.30
	3	0.71	4.69	3.32
	Optimized	0.82	4.24	<b>3.47</b>
192/40 $\lambda$	1	0.91	10.42	9.37
	2	0.66	13.63	8.99
	3	0.77	12.85	9.89
	Optimized	0.85	12.07	<b>10.25</b>
256/60 $\lambda$	1	0.90	12.90	11.61
	2	0.78	15.08	11.76
	3	0.88	13.01	12.15
	Optimized	0.86	14.24	<b>12.24</b>

The radiation pattern of these optimized apertures are given in Figure 61, where the 128, 192 and 256 elements optimized array are illustrated in (a), (b) and (c), respectively. Although the apertures have a high  $M_o$ , the amplitudes aside the maximum point rapidly decrease, which indicates that the ultrasonic images generated by these arrays will have a better contrast.

The amplitudes of the radiation patterns can be compared to the other configurations to see the improvement in the main and side lobe distribution. Table 15 gives the percentage distribution and mean of the radiation patterns comparing the optimized sparse array with the configurations analysed before. In all cases, the optimized aperture is defined for the x-axis, which is the negative percentage/mean.

Overall, it is possible to see that the optimized aperture has a better main lobe distribution compared to the other apertures. In all cases, the percentage was higher in the positive region, which corresponds to configurations 1, 2 and 3.

Figure 61 – Radiation pattern wideband response of the spiral optimized arrays. (a) 128, (b) 192 and (c) 256 elements array.



Source: Author

Table 13 – Main lobe and side lobe distribution analysis. Optimized aperture vs configurations 1,2 and 3.

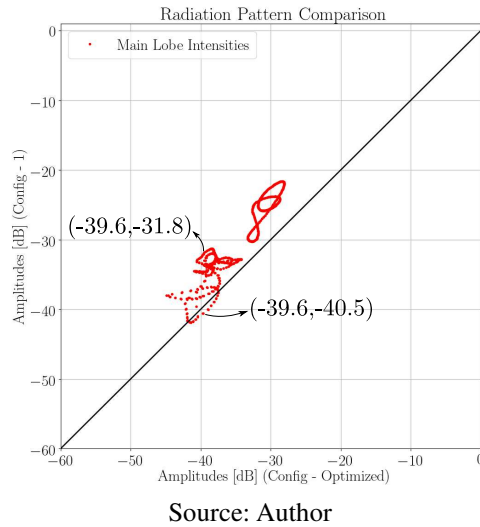
Settings	Combination	Main Lobe Information		Side Lobe Information	
		Neg/Pos (%)	Mean	Neg/Pos (%)	Mean
128/40 $\lambda$	Opt-1	04/96	-0.44/3.35	50/50	-1.48/1.71
	Opt-2	47/53	-3.37/7.38	43/57	-1.62/1.99
	Opt-3	29/71	-2.15/3.49	44/56	-1.65/1.89
192/40 $\lambda$	Opt-1	11/89	-0.76/4.19	56/44	-1.86/1.82
	Opt-2	20/80	-3.69/5.87	42/58	-1.79/2.06
	Opt-3	40/60	-3.30/4.17	48/52	-1.75/1.84
256/60 $\lambda$	Opt-1	39/61	-1.05/5.37	49/51	-1.76/1.94
	Opt-2	28/72	-3.03/3.15	45/55	-1.84/1.90
	Opt-3	20/80	-0.95/4.15	51/49	-1.77/1.87

The mean, in its absolute values, is lower for the negative region. This means that, when selecting one point in the negative area, it is more probable that the difference between the ordinate and abscissa is smaller than when a point in the positive region is selected. Figure 62 illustrates the radiation pattern comparison of the combination Opt-1 in the 128/40 $\lambda$  setting, where the mean values for the main lobe are -0.44/3.35 for the negative and positive regions, respectively.

Two points were selected, one in the negative and the other in the positive area. In the negative region, the point has the coordinate (-39.6,-40.5), which means that in one pixel of the RPs the amplitude in the RP generated by the optimized aperture is -39.6 dB and in the configuration-1 is -40.5 dB. This difference is lower when comparing the positive point selected, which has a coordinate (-39.6,-31.8). The mean value is a figure of merit that shows dominance of one radiation pattern over another, and it is possible to see that the optimized response has more dominance in the configurations RP.

Analysing the side lobe distribution, there are two cases where the amplitudes propor-

Figure 62 – Radiation pattern comparison between the optimized  $128/40\lambda$  aperture and configuration-1 of  $128/40\lambda$ .



tion is higher in the optimized aperture, in combination Opt-1 in setting  $192/40\lambda$  and Opt-3 in setting  $256/60\lambda$ . These configurations (1  $192/40\lambda$  and 3  $256/60\lambda$ ) have higher  $M_o$  values that contribute to the grating lobes suppression resulting in lower intensities compared to the optimized configurations. However, in both cases, the main lobe was better for the optimized aperture, where the amplitudes were 89% and 80% lower in the optimized array radiation pattern.

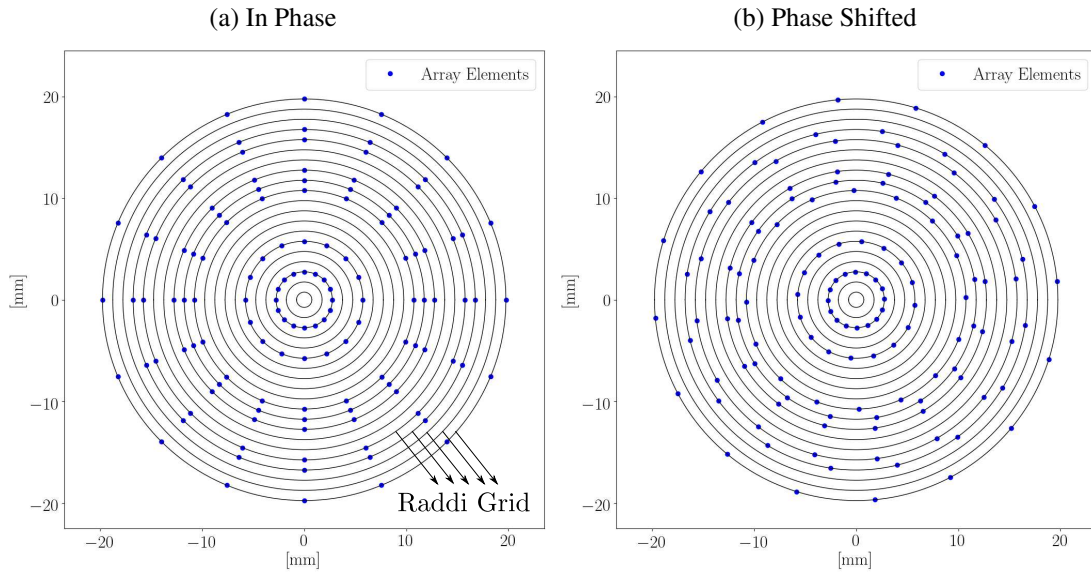
The optimization algorithm with the proposed fitness function was able to find apertures that have adequate coverage in the CPG matrix with high redundancy. When the radiation pattern of the optimized apertures was compared to configurations 1,2 and 3 with different settings, the optimized apertures generated a radiation pattern with better qualities with lower and rapid main lobe decreased and lower side lobes intensities.

The spiral array has a good element distribution where randomly selecting elements in the 360 array would create an aperture with an acceptable radiation pattern. To check if the FF works with a different aperture, an optimization problem using the proposed FF was designed to create different segmented annular arrays.

#### 5.4 SEGMENTED ANNULAR ARRAY OPTIMIZATION

The segmented annular array is a type of array where the elements are placed in rings. At each ring, the elements are equidistant to each other (MARTÍNEZ et al., 2003). Figure 63 (a) illustrates an 128 elements sparse segmented array. The array has 20 radii but only 8 are filled with elements. In each selected radius, there are 16 elements equidistant to each other. The radii elements in this array are placed in phase  $\varphi = 0^\circ$ , but, in (b), the elements in the radii are randomly phased.

Figure 63 – Segmented annular array example with 128 elements distributed in 8 radii. (a) radii in phase. (b) radii randomly rotated.



Source: Author

An optimization problem can be created where the algorithm will select several radii in a grid. These radii are pre-defined and coded into a binary vector, where one means that the respective radius is selected to create the sparse array. With the optimization problem defined in this way, the simulated annealing algorithm with the proposed FF can be used. Three types of arrays will be created based on the previous results (128,192/40 $\lambda$  and 256/60 $\lambda$ ).

The radii grid was arbitrary pre-defined starting from 1.50 $\lambda$  to 20 $\lambda$  for the 40 $\lambda$  diameter aperture and 1.50 $\lambda$  to 30 $\lambda$  for the 60 $\lambda$  diameter aperture. In both grids, the increasing step is 0.5 $\lambda$ . The algorithm selects eight radii for the emitter elements and eight radii for the receiver elements. The number of elements is equal for all radii, and the phase between the radii is randomly set.

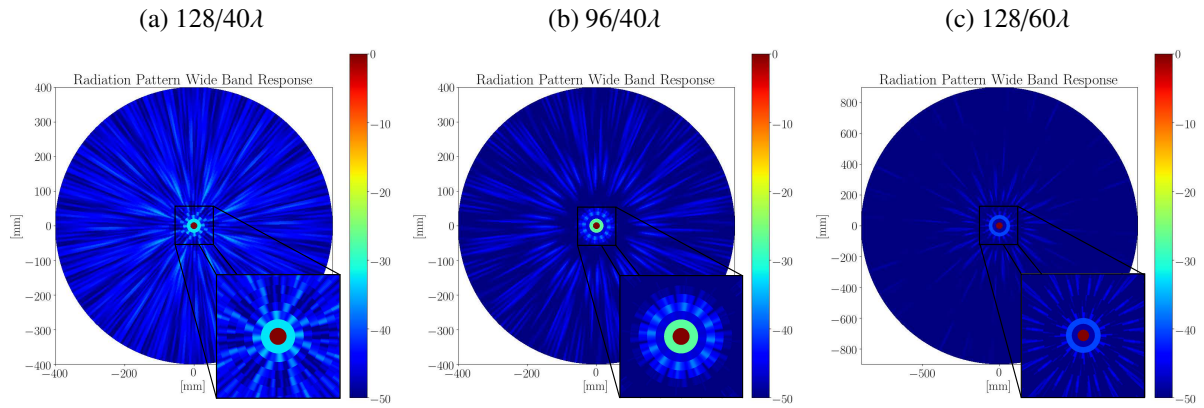
In Table 14, the  $M_o$ ,  $M_r$  and their multiplication are given for the spiral and segmented annular optimized apertures. In all cases, the segmented annular array has higher FF values. This array has a higher degree of freedom to place the elements compared to the spiral array, which made it possible to find apertures with better FF.

Table 14 –  $M_o$ ,  $M_r$  and  $M_oM_r$  of spiral and segmented optimized array.

Settings	Array Type	$M_o$	$M_r$	$M_oM_r$
128/40 $\lambda$	Spiral	<b>0.82</b>	4.24	3.47
	Annular	0.78	<b>6.01</b>	<b>4.68</b>
192/40 $\lambda$	Spiral	0.85	12.07	10.25
	Annular	<b>0.87</b>	<b>12.09</b>	<b>10.51</b>
256/60 $\lambda$	Spiral	<b>0.86</b>	14.24	12.24
	Annular	0.85	<b>14.50</b>	<b>12.32</b>

The radiation pattern of the three segmented annular apertures is illustrated in Figure 64, where the amplitudes aside the main lobe in the RP for these arrays are uniformly distributed as the elements in the radii are equidistant.

Figure 64 – Radiation pattern wideband response of the segmented annular optimized arrays. (a) 128, (b) 192 and (c) 256 elements array.



Source: Author

Table 15 gives the percentage and mean comparing the radiation pattern of the spiral with the segmented annular optimized array. Overall, the segmented annular array radiation pattern achieved a lower main and side lobe distribution. In the 256/60λ comparison, the main lobe percentage distribution is 50%. However, the mean is higher for the negative region, which means that the amplitudes in the segmented annular response are considerably lower compared to the spiral response. This can be seen in Figure 64 (c), where the amplitude asides the maximum point is close to -47 dB compared to the amplitudes of the optimized spiral which are about -30dB.

Table 15 – Main lobe and side lobe distribution analysis. Spiral array vs segmented annular array

Combination	Main Lobe Information		Side Lobe Information	
	Neg/Pos (%)	Mean	Neg/Pos (%)	Mean
128/40λ Spiral-Annular	70/30	-2.1/1.6	54/46	-2.10/1.79
192/40λ Spiral-Annular	62/38	-2.76/1.11	61/39	-2.39/1.79
256/60λ Spiral-Annular	50/50	-14.18/4.34	82/18	-2.64/1.75

The segmented annular array has more degree of freedom that enables to find apertures with better FF compared to the spiral array. Looking at the percentage distribution and the mean, the radiation pattern of the segmented annular array has narrowed the main lobe with lower side lobes. There are some factors that need to be better established that might help to find better configurations. For example, the phases between the radii are randomly defined, but they can also be optimized.

## 5.5 COMMENTS

In this chapter, the  $M_o$  and  $M_r$  parameters were studied to establish a relationship between these spatial parameters with the radiation pattern wideband response. After this study, a fitness function was proposed and used with the simulated annealing algorithm to find spiral and segmented annular array. In the optimized spiral arrays, the apertures found generated a radiation pattern with better characteristics compared to the ones studied (configurations 1, 2 and 3). In the segmented annular array, the optimized apertures had better radiation pattern characteristics compared to the spiral arrays.

Although the goal was achieved, the method needs some refinement in the future. The influence of the weights  $k_1$  and  $k_2$  set to one need to be studied, and perhaps create a method to define these weights based on the number of elements and aperture diameter. The optimization algorithm also needs to be changed, the neighbourhood generator function created in this work randomly swaps the elements and this random operation might be limiting the algorithm to find better apertures.

## 6 FINAL COMMENTS AND FUTURE WORK

### 6.1 RECAPITULATION AND APPLICATIONS

In this work, different aspects of ultrasonic imaging systems are improved using search techniques. At first, stochastic algorithms found configurations of sparse linear arrays, where a new codification method and the RP FF helped to find configurations with lower FF than those presented in the literature. Afterwards, sparse arrays' analysis enables us to verify that the RP FF has problems distinguishing which sparse arrays would generate high or low-quality images. Considering this problem, a new FF based on the PSF was proposed. This FF was used to find different sparse configurations where it was possible to check that this FF can distinguish how better a sparse array would generate an image based on the reduction of the FF value. Comparing the configurations found using the two FF, the ones based on the PSF balance the lateral resolution and contrast better than the RP FF.

Although the linear array systems already work with hundreds of elements, there are some applications for sparse linear arrays. These arrays require less energy to operate when compared to FPA with the same length. Therefore, an ultrasonic system that works in a region with restricted energy access, such as inside rain forests or in health care in impoverished areas, can use sparse linear arrays to save energy. The system might use a smartphone as a processing core and energy source.

Moreover, the design of sparse linear arrays enables the re-use of ultrasonic transducers with few elements malfunctioning. A sparse array can be designed where the broken elements and others are removed from the imaging system. In consequence, the ultrasonic probe is re-used, helping extend its lifetime. These applications help the health access in developing/poor countries and increase health quality worldwide.

In the second part of the thesis, a heuristic creates acquisition strategies for synthetic aperture systems. The algorithm analyses the projections of the coarray elements that most fill a grid matrix with low redundancy to build an acquisition. Different acquisitions for spiral Fermat and annular segmented arrays were analysed, which overall indicated that signals can be removed from the imaging system without much loss in the image quality.

At last, during the development of the acquisition strategy, two parameters were created to verify the occupancy and redundancy of an array in a grid. These two parameters were studied to check their influence on the radiation pattern response. Understanding its influence, a fitness function was created, and the simulated annealing algorithm was used to create sparse arrays in two setups. First, the elements in a pre-defined spiral array were selected using the algorithm. Then, the metaheuristic selected different radii of a grid to create an annular segmented array. The results of the radiation pattern analysed indicated that the optimized spiral array has better characteristics compared to the spiral where the elements were randomly se-

lected. When compared to the optimized annular segmented array, the radiation pattern of these arrays had better qualities compared to the spiral Fermat array. It was possible to use spatial measurements to evaluate sparse arrays based on non-grid arrays.

2D arrays create volumetric images without the need to sweep the transducer. It is possible to manufacture transducers with thousand of elements using CMUT, and the problem is to handle the data volume, electronic resources and acquisition time required to generate an image. Non-grid apertures have a better spatial element distribution compared to matrix arrays, achieving lower side lobes intensities and high lateral resolution using fewer elements. The acquisition strategy proposed reduces the acquisition time and data volume to generate an image, which enables the creation of real-time ultrasonic applications using the synthetic aperture technique.

The proposed 2D sparse array design method reduces the number of elements used in a pre-defined array. With this element reduction, phased array systems, which are used worldwide, can handle the number of elements in the sparse array. Moreover, the acquisition strategy technique can be used in the sparse array to reduce the resources required to manage the 2D transducer and create a real-time ultrasonic system based on a synthetic aperture technique.

Each part of the work helps to improve ultrasonic imaging systems by reducing the resources involved. In consequence, the data volume, electronic complexity, acquisition time and time to generate images are also reduced, enabling the use of ultrasonic images for different applications.

## 6.2 CONTRIBUTIONS

The highlights of this thesis are:

- A review in ultrasonic array simulation for linear and bidimensional array and imaging strategies.
- A study in continuous metaheuristics and a codification strategy that helped to find better sparse linear arrays.
- A new FF applied to linear sparse array design that correctly evaluates the arrays.
- A heuristic that builds an acquisition strategy for synthetic aperture for non-grid arrays.
- A study in spatial parameters and how it is linked to the radiation pattern wideband response.
- A optimization strategy to design sparse non-grid for Fermat spiral and annular segmented arrays

### 6.3 PUBLICATIONS

#### Journals:

- DE SOUZA, J. C. E.; PARRILLA-ROMERO, M.; HIGUTI, R. T.; MARTÍNEZ-GRAULLERA, O. Design of Ultrasonic Synthetic Aperture Imaging Systems Based on a Non-Grid 2D Sparse Array. *sensors*, v. 21, n. 23, p. 1-20, 2021.
- MARTÍNEZ-GRAULLERA, O.; DE SOUZA, J. C. E.; PARRILLA-ROMERO, M. ; HIGUTI, R. T. Design of 2D Planar Sparse Binned Arrays Based on the Coarray Analysis. *sensors*, v. 21, n. 23, p.1-21, 2021.

#### Congress:

- DE SOUZA, J. C. E.; PRADO, V. T.; MARTÍNEZ-GRAULLERA, O.; HIGUTI, R. T. A New Fitness Function for Sparse Linear Array Evaluation Based on the Point Spread Function. In: IEEE UFFC LATIN AMERICA ULTRASONICS SYMPOSIUM, 2021, Gainesville. *Anais...*, Gainesville: IEEE, 2021. p. 1–4.
- MARTÍNEZ-GRAULLERA, O.; DE SOUZA, J. C. E.; HIGUTI, R. T.; ROMERO, M. P.; RODRIGUEZ, A. I. Técnica De Conformación Basada En El Coarray Para Mejorar La Calidad De Imagen En Sistemas De Apertura Sintética. In: XI CONGRESSO IBÉRICO DE ACÚSTICA E 51º CONGRESO ESPAÑOL DE ACÚSTICA,2020, Faro *Anais...*, Lisboa: Sociedade Portuguesa de Acústica (SPA), 2020. p. 789-800.
- MARTÍNEZ-GRAULLERA, O.; DE SOUZA, J. C. E.; HIGUTI, R. T.; ROMERO, M. P.; RODRIGUEZ, A. I. Prototipo De Un Array Bidimensional Ultra-disperso Para Imagen Ultrasonica De Alta Resolucion. In: XI CONGRESSO IBÉRICO DE ACÚSTICA E 51º CONGRESO ESPAÑOL DE ACÚSTICA,2020, Faro *Anais...*, Lisboa: Sociedade Portuguesa de Acústica (SPA), 2020. p. 777-788.

### 6.4 FUTURE WORKS

Non-grid arrays can be designed using the linear sparse array optimization algorithm presented in Chapter 3. This increase in the degree of freedom might contribute to the quality of the sparse linear array image, especially related to sidelobes reduction. The designed 2D arrays should be experimentally tested, but there are practical difficulties related to array manufacturing and costs. Another possible application is in the inspection of plate-like structures using Lamb waves, where the elements do not necessarily need to be placed in a linear fashion but can be distributed along the plate surface. Another idea is to use the acquisition strategy

proposed in Chapter 4 in the optimized apertures found in Chapter 5 to reduce even more resources. At last, the design of 2D apertures can be enhanced by considering the optimization of the phase in the annular segmented array.

## APPENDIX A – SEARCH PROBLEMS AND METAHEURISTICS

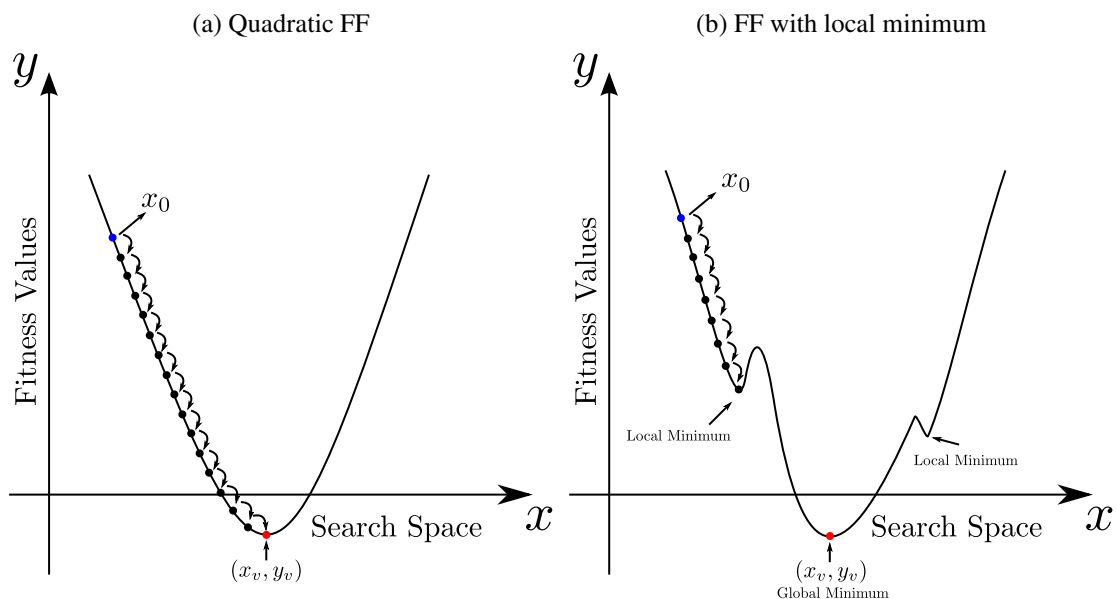
Metaheuristics are stochastic algorithms used to find solutions for optimisation problems that are NP-Hard, which are problems that increase exponentially and requires considerable computing effort to be solved (GLOVER, 1986). Most of the time, metaheuristics are interpreted as a black box optimizer applied to an optimization problem. The reason why is that metaheuristics are complex and has their only field of study.

To understand the basics of optimisation problems and therefore understand why metaheuristics, a simple example can be analysed. First, let's consider a variable  $x$  that can assume any real value, defined as the search space. Then, defining a fitness function (FF) as a second-degree equation, an optimization problem is set as trying to find the value of  $x$  that has the minimum value of FF.

In this case, the results (image) of the function is known and illustrated in Figure 65(a). A simple method to find the minimum value of this function FF is to start in any solution ( $x_0$ ) and move to another solution that returns a lower FF value. If this is done consecutively, the best solution  $x_v$  in this problem is found. This strategy is named Gradient Descendent and, although it is simple, in convex spaces the best solution is guaranteed to be found (GERON, 2019).

This example is straightforward because the possible results converge to a valley. If FF is changed and the image assumes the results illustrated in Figure 65(b), the strategy adopted maybe not find the best results (global minimum). Instead, it would stay at a local minimum.

Figure 65 – Search Space. (a) Image of a second-order equation. (b) Image of a different FF where there are minimums that the search algorithm can be stuck.



Source: Author

In real problems, it is impossible to calculate all the FF for all solutions and find the

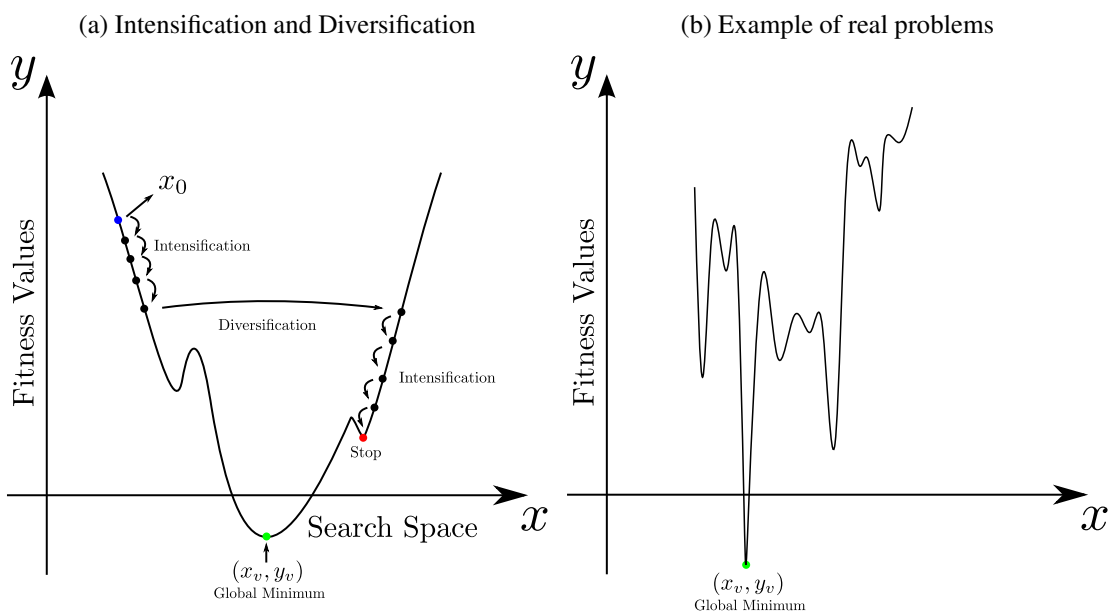
global minimum. Therefore, alternatives such as metaheuristics are used to intelligently test solutions and find the best ones. These algorithms try to escape from the local minimums and test different areas by using two strategies, intensification and diversification (NESMACHNOW, 2014).

During the intensification stage, the algorithm proposes solutions near to the current solution and calculate their FF. Then, using probability, this new solution maybe will turn into a current solution. In the diversification stage, the difference from the intensification is that the solutions proposed are located far from the current solution. An illustration of these two processes is given in Figure 66 (a), where at  $x_0$  the intensification process is applied. After four iterations, diversification is used, and the current solution that was in the left jump to the right in the search space.

In this example, the search was not able to find the global minimum. It stopped in a valley. Real applications have this problem, in which the best solution found is not guaranteed to be the global minimum. The challenge is to identify what is restraining the algorithm and propose alternatives to bypass this problem. In Figure 66 (a), for example, the stop criteria, which is the condition used to stop the search, could be used earlier. Maybe, if the search had continued, the local minimum would be found.

A more realistic search is illustrated in Figure 66 (b), where it is possible to see different valleys where the algorithm might be stuck during the searching process.

Figure 66 – Search Space. (a) illustration of intensification and diversification process in metaheuristics. (b) real representation of a searching problem.



Source: Author

In the example, the search is defined in the continuous domain, where also  $x$  could assume any real value. However, depending on the problem, the search space needs to be

constrained, and if a proposed solution is not acceptable, strategies can be used to make it acceptable. Moreover, some optimization problems are defined in a discrete (binary) domain, where the proposed solutions are vectors of zeros and ones (BEHESHTI; SHAMSUDDIN, 2013).

The metaheuristics vary from each other in different ways, mainly in the strategy to intensify, diversify. However, some metaheuristic, such as particle swarm optimization (KENNEDY; EBERHART, 1995), were designed to work in continuous domain. Other algorithms, such as the Genetic algorithm (HOLLAND, 1992), were designed to work with binary search. When defining a search problem, the representation of the solution needs to be taken into account so we can select an algorithm. Furthermore, another challenge in search problems is to create a FF that can correctly quantify the solutions  $x$ .

In this appendix, the main concepts of a search problem were presented, where the challenges of local minimums were illustrated. We also commented that the metaheuristics are used to intelligently test the solutions of a search problem as in real applications is impossible to test all solutions. Also, we present the intensification and diversification process and comment that metaheuristics vary from each other mainly in these two stages.

## BIBLIOGRAPHY

- ABUALIGAH, L.; DIABAT, A.; MIRJALILI, S.; ELAZIZ, M. A.; GANDOMI, A. H. The arithmetic optimization algorithm. *Computer Methods in Applied Mechanics and Engineering*, Amsterdam, v. 376, n. 1, p. 1–38, 2021.
- BANNOUF, S.; ROBERT, S.; CASULA, O.; PRADA, C. Data set reduction for ultrasonic TFM imaging using the effective aperture approach and virtual sources. *Journal of Physics: Conference Series*, Bristol, v. 457, n. 1, p. 1–14, 2013.
- BEHESHTI, Z.; SHAMSUDDIN, S. M. H. A review of population-based meta-heuristic algorithm. *International Journal of Advances in Soft Computing & Its Applications*, Irbid, v. 5, n. 1, p. 1–35, 2013.
- BEVAN, R. L. T.; BUDYN, N.; ZHANG, J.; CROXFORD, A. J.; KITAZAWA, S.; WILCOX, P. D. Data fusion of multiview ultrasonic imaging for characterization of large defects. *IEEE Transactions on Ultrasonics, Ferroelectrics, and Frequency Control*, Piscataway, v. 67, n. 11, p. 2387–2401, 2020.
- BIRK, M.; BALZER, M.; RUITER, N. V.; BECKER, J. Evaluation of performance and architectural efficiency of FPGAs and GPUs in the 40 and 28 nm generations for algorithms in 3D ultrasound computer tomography. *Computers & Electrical Engineering*, Elmsford, v. 40, n. 4, p. 1171–1185, 2014.
- BRUNKE, S.; LOCKWOOD, G. Broad-bandwidth radiation patterns of sparse two-dimensional vernier arrays. *IEEE Transactions on Ultrasonics, Ferroelectrics, and Frequency Control*, Piscataway, v. 44, n. 5, p. 1101–1109, 1997.
- CARDONE, G.; CINCOTTI, G.; GORI, P.; PAPPALARDO, M. Optimization of wide-band linear arrays. *IEEE Transactions on Ultrasonics, Ferroelectrics, and Frequency Control*, Piscataway, v. 48, n. 4, p. 943–952, 2001.
- CHEN, P.; ZHENG, Y.; ZHU, W. Optimized simulated annealing algorithm for thinning and weighting large planar arrays in both far-field and near-field. *IEEE Journal of Oceanic Engineering*, New York, v. 36, n. 4, p. 658–664, 2011.
- DAKKAK, W.; OLIVER, T. I. *Ventricular Septal Defect*. 1. ed. Saint Petersburg: StatPearls, 2020.
- DE SOUZA, J. C. E.; ROMERO, M. P.; HIGUTI, R. T.; MARTÍNEZ-GRAULLERA, O. Design of ultrasonic synthetic aperture imaging systems based on a non-grid 2D sparse array. *Sensors*, Basel, v. 21, n. 23, p. 1–20, 2021.
- DIARRA, B.; ROBINI, M.; TORTOLI, P.; CACHARD, C.; LIEBGOTT, H. Design of optimal 2D nongrid sparse arrays for medical ultrasound. *IEEE Transactions on Biomedical Engineering*, New York, v. 60, n. 11, p. 3093–3102, 2013.
- DRINKWATER, B. W.; WILCOX, P. D. Ultrasonic arrays for non-destructive evaluation: A review. *NDT & E International*, Oxford, v. 39, n. 7, p. 525–541, 2006.
- DUGGAN, N.; LITEPLO, A.; SHOKOOHI, H.; GOLDSMITH, A. Using lung point-of-care ultrasound in suspected COVID-19: case series and proposed triage algorithm. *Clinical Practice and Cases in Emergency Medicine*, New York, v. 4, n. 3, p. 289–294, 2020.

- GASKILL, J. D. *Linear Systems, Fourier Transforms, and Optics*. 1. ed. New York: John Wiley & Sons, 1978.
- GEHLBACH, S. M.; ALVAREZ, R. E. Digital ultrasound imaging techniques using vector sampling and raster line reconstruction. *Ultrasonic Imaging*, New York, v. 3, n. 1, p. 83–107, 1981.
- GERON, A. *Mãos à Obra: Aprendizado de Máquina com Scikit-Learn & TensorFlow*. Rio de Janeiro: Alta Books, 2019. v. 1.
- GLOVER, F. Future paths for integer programming and links to artificial intelligence. *Computers & Operations Research*, New York, v. 13, n. 5, p. 533–549, 1986. Applications of Integer Programming.
- GOSS, S.; FRIZZELL, L.; KOUZMANOFF, J.; BARICH, J.; YANG, J. Sparse random ultrasound phased array for focal surgery. *IEEE Transactions on Ultrasonics, Ferroelectrics, and Frequency Control*, Piscataway, v. 43, n. 6, p. 1111–1121, 1996.
- HAUPT, R. Thinned arrays using genetic algorithms. *IEEE Transactions on Antennas and Propagation*, New York, v. 42, n. 7, p. 993–999, 1994.
- HOCTOR, R. T.; KASSAM, S. A. The unifying role of the coarray in aperture synthesis for coherent and incoherent imaging. *Proceedings of the IEEE*, New York, v. 78, n. 4, p. 735–752, 1990.
- HOLLAND, J. H. Genetic algorithms. *Scientific American*, v. 267, n. 1, p. 66–73, 1992.
- HOLMES, C.; DRINKWATER, B. W.; WILCOX, P. D. Post-processing of the full matrix of ultrasonic transmitreceive array data for non-destructive evaluation. *NDT & E International*, Oxford, v. 38, n. 8, p. 701–711, 2005.
- HU, H.; DU, J.; XU, N.; JEONG, H.; WANG, X. Ultrasonic sparse-TFM imaging for a two-layer medium using genetic algorithm optimization and effective aperture correction. *NDT & E International*, Oxford, v. 90, n. 1, p. 24–32, 2017.
- HU, H.; DU, J.; YE, C.; LI, X. Ultrasonic phased array sparse-TFM imaging based on sparse array optimization and new edge-directed interpolation. *Sensors*, Basel, v. 18, n. 3, p. 1–15, 2018.
- ISHIGURO, M. Minimum redundancy linear arrays for a large number of antennas. *Radio Science*, Washington, v. 15, n. 06, p. 1163–1170, 1980.
- JENSEN, J. A. Ultrasound imaging and its modeling. In: FINK, M.; KUPERMAN, W. A.; MONTAGNER, J.-P.; TOURIN, A. (Ed.). *Imaging of Complex Media with Acoustic and Seismic Waves*. Heidelberg: Springer-Verlag Berlin Heidelberg, 2002. v. 1, cap. 6, p. 135–166.
- JENSEN, J. A.; NIKOLOV, S. I.; GAMMELMARK, K. L.; PEDERSEN, M. H. Synthetic aperture ultrasound imaging. *Ultrasonics*, Surrey, v. 44, n. 1, p. e5–e15, 2006.
- JOLLY, M.; PRABHAKAR, A.; STURZU, B.; HOLLSTEIN, K.; SINGH, R.; THOMAS, S.; FOOTE, P.; SHAW, A. Review of non-destructive testing (NDT) techniques and their applicability to thick walled composites. *Procedia CIRP*, Amsterdam, v. 38, n. 1, p. 129–136, 2015.

KARAMAN, M.; WYGAMT, I. O.; PRALKAN, O.; KHURI-YAKUB, B. T. Minimally redundant 2D array designs for 3D medical ultrasound imaging. *IEEE Transactions on Medical Imaging*, New York, v. 28, n. 7, p. 1051–1061, 2009.

KENNEDY, J.; EBERHART, R. Particle swarm optimization. In: INTERNATIONAL CONFERENCE ON NEURAL NETWORKS, 1995, Perth. *Anais...* Perth: IEEE, 1995. p. 1942–1948.

KHALILI, P.; CAWLEY, P. The choice of ultrasonic inspection method for the detection of corrosion at inaccessible locations. *NDT & E International*, Oxford, v. 99, n. 1, p. 80 – 92, 2018.

KIRKPATRICK, S.; GELATT, C. D.; VECCHI, M. P. Optimization by simulated annealing. *Science*, New York, v. 220, n. 1, p. 671–680, 1983.

LAROCHE, N.; BOURGUIGNON, S.; CARCREFF, E.; IDIER, J.; DUCLOS, A. An inverse approach for ultrasonic imaging from full matrix capture data: Application to resolution enhancement in NDT. *IEEE Transactions on Ultrasonics, Ferroelectrics, and Frequency Control*, Piscataway, v. 67, n. 9, p. 1877–1887, 2020.

LI, Z.; CHI, C. Fast computation of far-field pulse-echo PSF of arbitrary arrays for large sparse 2D ultrasound array design. *Ultrasonics*, Surrey, v. 84, p. 63–73, 2018.

LOCKWOOD, G.; LI, P.-C.; O'DONNELL, M.; FOSTER, F. Optimizing the radiation pattern of sparse periodic linear arrays. *IEEE Transactions on Ultrasonics, Ferroelectrics, and Frequency Control*, Piscataway, v. 43, n. 1, p. 7–14, 1996a.

LOCKWOOD, G.; LI, P.-C.; O'DONNELL, M.; FOSTER, F. Optimizing the radiation pattern of sparse periodic two dimensional arrays. *IEEE Transactions on Ultrasonics, Ferroelectrics, and Frequency Control*, Piscataway, v. 43, n. 1, p. 15–19, 1996b.

LOCKWOOD, G.; TALMAN, J.; BRUNKE, S. Real-time 3D ultrasound imaging using sparse synthetic aperture beamforming. *IEEE Transactions on Ultrasonics, Ferroelectrics, and Frequency Control*, Piscataway, v. 45, n. 4, p. 980–988, 1998.

MAGNIN, P. A.; RAMM, O. T.; THURSTONE, F. L. Delay quantization error in phased array images. *IEEE Trans. on Sonics and Ultrasonics*, New York, v. 28, n. 5, p. 305–310, 1981.

MARMONIER, M.; ROBERT, S.; LAURENT, J.; PRADA, C. Real-time 3D imaging with Fourier-domain algorithms and matrix arrays applied to non-destructive testing. *Ultrasonics*, Surrey, v. 124, p. 106–122, 2022.

MARTÍN, C.; MARTÍNEZ, O.; OCTAVIO, A.; MONTERO, F.; ULLATE, L. 2D SAFT technique to reduce grating lobes in volumetric imaging. *Physics Procedia*, Amsterdam, v. 3, n. 1, p. 381–388, 2010. ICU, Santiago de Chile, January 2009.

MARTÍN, C. J.; ROMERO-LAORDEN, D.; MARTÍNEZ-GRAULLERA, O.; PEREZ-LOPEZ, M.; ULLATE, L. G. An ultrasonic imaging system based on a new SAFT approach and a GPU beamformer. *IEEE Transactions on Ultrasonics, Ferroelectrics, and Frequency Control*, Piscataway, v. 59, n. 7, p. 1402–1412, 2012.

MARTÍNEZ-GRAULLERA, O.; MARTÍN, C. J.; GODOY, G.; ULLATE, L. G. 2D array design based on Fermat spiral for ultrasound imaging. *Ultrasonics*, Surrey, v. 50, n. 2, p. 280–289, 2010.

MARTÍNEZ, O.; AKHNAK, M.; ULLATE, L. G.; MONTERO DE ESPINOSA, F. A small 2D ultrasonic array for NDT applications. *NDT & E International*, Oxford, v. 36, n. 1, p. 57–63, 2003.

MIRJALILI, S.; LEWIS, A. The Whale Optimization Algorithm. *Advances in Engineering Software*, Barking, v. 95, n. 1, p. 51–67, 2016.

MITRA, S. K.; MONDAL, K.; TCHOBANOU, M. K.; DOLECEK, G. J. General polynomial factorization-based design of sparse periodic linear arrays. *IEEE Transactions on Ultrasonics, Ferroelectrics, and Frequency Control*, Piscataway, v. 57, n. 9, p. 1952–1966, 2010.

MONDAL, S. C.; WILCOX, P. D.; DRINKWATER, B. W. Design and evaluation of two dimensional phased array ultrasonic transducers. In: AIP CONFERENCE PROCEEDINGS, 2005, Golden. *Anais...* Golden: American Institute of Physics, 2005. v. 760, n. 760, p. 899–905.

MURATA, T.; ISHIBUCHI, H.; TANAKA, H. Multi-objective genetic algorithm and its applications to flowshop scheduling. *Computers & Industrial Engineering*, New York, v. 30, n. 4, p. 957–968, 1996.

MURINO, V.; TRUCCO, A.; REGAZZONI, C. Synthesis of unequally spaced arrays by simulated annealing. *IEEE Transactions on Signal Processing*, New York, v. 44, n. 1, p. 119–122, 1996.

NESMACHNOW, S. An overview of metaheuristics: Accurate and efficient methods for optimisation. *International Journal of Metaheuristics*, Genebra, v. 3, n. 4, p. 320–347, 2014.

ORALKAN, O.; ERGUN, A.; CHENG, C.-H.; JOHNSON, J.; KARAMAN, M.; LEE, T.; KHURI-YAKUB, B. Volumetric ultrasound imaging using 2D CMUT arrays. *IEEE Transactions on Ultrasonics, Ferroelectrics, and Frequency Control*, Piscataway, v. 50, n. 11, p. 1581–1594, 2003.

PARK, J.; SHIN, D.; HAN, J.; OH, J.; PARK, S.; KIM, Y.; JANG, J.; LEE, W.; PARK, S. Design, fabrication of honeycomb-shaped 1-3 connectivity piezoelectric micropillar arrays for 2D ultrasound transducer application. *Ceramics International*, Oxford, v. 46, n. 8, p. 12023–12030, 2020.

PATTERSON, M. S.; FOSTER, F. S. The improvement and quantitative assessment of B-mode images produced by an annular array/cone hybrid. *Ultrasonic Imaging*, Oxford, v. 5, n. 3, p. 195–213, 1983.

PETERSON, D. K.; KINO, G. S. Real-time digital image reconstruction: A description of imaging hardware and an analysis of quantization errors. *IEEE Trans. on Sonics and Ultrasonics*, New York, v. 31, n. 4, p. 337–351, 1984.

QIAN, X.; WODNICKI, R.; KANG, H.; ZHANG, J.; TCHELEPI, H.; ZHOU, Q. Current ultrasound technologies and instrumentation in the assessment and monitoring of COVID-19 positive patients. *IEEE Transactions on Ultrasonics, Ferroelectrics, and Frequency Control*, Piscataway, v. 67, n. 11, p. 2230–2240, 2020.

RANGARAJU, K.; KUMAR, K.; RENUMADHAVIM, C. H. Review paper on quantitative image quality assessment – medical ultrasound images. *International Journal of Engineering Research & Technology*, Gandhinagar, v. 1, n. 4, p. 1–6, 2012.

- RASMUSSEN, M. F.; JENSEN, J. A. Comparison of 3D synthetic aperture phased-array ultrasound imaging and parallel beamforming. *IEEE Transactions on Ultrasonics, Ferroelectrics, and Frequency Control*, Piscataway, v. 61, n. 10, p. 1638–1650, 2014.
- ROMERO-LAORDEN, D.; VILLAZÓN-TERRAZAS, J.; MARTÍNEZ-GRAULLERA, O.; IBANEZ, A.; PARRILLA, M.; PEÑAS, M. S. Analysis of parallel computing strategies to accelerate ultrasound imaging processes. *IEEE Transactions on Parallel and Distributed Systems*, New York, v. 27, n. 12, p. 3429–3440, 2016.
- ROUX, E.; RAMALLI, A.; LIEBGOTT, H.; CACHARD, C.; ROBINI, M. C.; TORTOLI, P. Wideband 2D array design optimization with fabrication constraints for 3D US imaging. *IEEE Transactions on Ultrasonics, Ferroelectrics, and Frequency Control*, Piscataway, v. 64, n. 1, p. 108–125, 2017.
- SCHWARTZ, J. L.; STEINBERG, B. D. Ultrasparse, ultrawideband arrays. *IEEE Transactions on Ultrasonics, Ferroelectrics, and Frequency Control*, Piscataway, v. 45, n. 2, p. 376–393, 1998.
- SHANNON, C. E. A mathematical theory of communication. *Bell Syst. Tech. J.*, New Jersey, v. 27, n. 3, p. 379–423, 1948.
- STEINBERG, B. D. *Principles of aperture and array system design: Including random and adaptive arrays*. 1. ed. New York: John Wiley & Sons, 1976. 356 p.
- STEINBERG, B. D. Digital beamforming in ultrasound. *IEEE Transactions on Ultrasonics, Ferroelectrics, and Frequency Control*, Piscataway, v. 39, n. 6, p. 716–721, 1992.
- SUN, S.; WU, D.; ZHU, B.; ZHANG, Y.; CHEN, S.; YANG, X. Novel fabrication of a 2D ring array for real-time volumetric endoscopic ultrasound imaging. *Ultrasonics*, Surrey, v. 60, n. 1, p. 6–10, 2015.
- SZABO, T. L. Beamforming. In: SZABO, T. L. (Ed.). *Diagnostic Ultrasound Imaging: Inside Out*. Boston: Academic Press, 2014. v. 1, cap. 6, p. 167–207.
- TRUCCO, A. Thinning and weighting of large planar arrays by simulated annealing. *IEEE Transactions on Ultrasonics, Ferroelectrics, and Frequency Control*, Piscataway, v. 46, n. 2, p. 347–355, 1999.
- TRUCCO, A. Weighting and thinning wide-band arrays by simulated annealing. *Ultrasonics*, Surrey, v. 40, n. 1, p. 485–489, 2002.
- TURNBULL, D.; FOSTER, F. Beam steering with pulsed two-dimensional transducer arrays. *IEEE Transactions on Ultrasonics, Ferroelectrics, and Frequency Control*, Piscataway, v. 38, n. 4, p. 320–333, 1991.
- WANG, Z.; BOVIK, A.; SHEIKH, H.; SIMONCELLI, E. Image quality assessment: From error visibility to structural similarity. *IEEE Transactions on Image Processing*, New York, v. 13, n. 4, p. 600–612, 2004.
- WOOH, S.-C.; SHI, Y. Optimum beam steering of linear phased arrays. *Wave Motion*, Amsterdam, v. 29, n. 3, p. 245–265, 1999a.
- WOOH, S.-C.; SHI, Y. Three-dimensional beam directivity of phase-steered ultrasound. *The Journal of the Acoustical Society of America*, New York v. 105, n. 6, p. 3275–3282, 1999b.

YANG, P.; CHEN, B.; SHI, K.-R. A novel method to design sparse linear arrays for ultrasonic phased array. *Ultrasonics*, Surrey, v. 44, p. e717–e721, 2006. Proceedings of Ultrasonics International (UT'05) and World Congress on Ultrasonics (WCU).

YANG, S.-H.; KIANG, J.-F. Optimization of sparse linear arrays using harmony search algorithms. *IEEE Transactions on Antennas and Propagation*, New York, v. 63, n. 11, p. 4732–4738, 2015.

YANG, X. A new metaheuristic bat-inspired algorithm. In: THE IV INTERNATIONAL WORKSHOP ON NATURE INSPIRED COOPERATIVE STRATEGIES (NICSO), 2010, Granada. *Anais...* Granada: Springer, 2010. p. 65–74.

YU, A. C. H.; DEMI, L.; MULLER, M.; ZHOU, Q. Ultrasound imaging: A silent hero in COVID-19 and lung diagnostics. *IEEE Transactions on Ultrasonics, Ferroelectrics, and Frequency Control*, Piscataway, v. 67, n. 11, p. 2194–2196, 2020.

ZHANG, H.; BAI, B.; ZHENG, J.; ZHOU, Y. Optimal design of sparse array for ultrasonic total focusing method by binary particle swarm optimization. *IEEE Access*, New York, v. 8, n. 1, p. 111945–111953, 2020.

ZONG, W. G.; JOONG, H. K.; LOGANATHAN, G. A new heuristic optimization algorithm: Harmony search. *Simulation*, New York, v. 76, n. 2, p. 60–68, 2001.